





Laser in der Materialbearbeitung  
Forschungsberichte des IFSW

D. Holder  
Laser micromachining with target depth

# **Laser in der Materialbearbeitung**

## **Forschungsberichte des IFSW**

Herausgegeben von  
Prof. Dr. phil. nat. Thomas Graf, Universität Stuttgart  
Institut für Strahlwerkzeuge (IFSW)

Das Strahlwerkzeug Laser gewinnt zunehmende Bedeutung für die industrielle Fertigung. Einhergehend mit seiner Akzeptanz und Verbreitung wachsen die Anforderungen bezüglich Effizienz und Qualität an die Geräte selbst wie auch an die Bearbeitungsprozesse. Gleichzeitig werden immer neue Anwendungsfelder erschlossen. In diesem Zusammenhang auftretende wissenschaftliche und technische Problemstellungen können nur in partnerschaftlicher Zusammenarbeit zwischen Industrie und Forschungsinstituten bewältigt werden.

Das 1986 gegründete Institut für Strahlwerkzeuge der Universität Stuttgart (IFSW) beschäftigt sich unter verschiedenen Aspekten und in vielfältiger Form mit dem Laser als einem Werkzeug. Wesentliche Schwerpunkte bilden die Weiterentwicklung von Strahlquellen, optischen Elementen zur Strahlführung und Strahlformung, Komponenten zur Prozessdurchführung und die Optimierung der Bearbeitungsverfahren. Die Arbeiten umfassen den Bereich von physikalischen Grundlagen über anwendungsorientierte Aufgabenstellungen bis hin zu praxisnaher Auftragsforschung.

Die Buchreihe „Laser in der Materialbearbeitung – Forschungsberichte des IFSW“ soll einen in der Industrie wie in Forschungsinstituten tätigen Interessentenkreis über abgeschlossene Forschungsarbeiten, Themenschwerpunkte und Dissertationen informieren. Studenten soll die Möglichkeit der Wissensvertiefung gegeben werden.

# **Laser micromachining with target depth**

von Dr.-Ing. Daniel Holder  
Universität Stuttgart



utzverlag München

Als Dissertation genehmigt  
von der Fakultät für Konstruktions-, Produktions- und Fahrzeugtechnik  
der Universität Stuttgart

Hauptberichter: Prof. Dr. phil. nat. Thomas Graf  
Mitberichter: Prof. Dr. Ing. André Zimmermann

Bibliografische Information der Deutschen Nationalbibliothek  
Die Deutsche Nationalbibliothek verzeichnet diese Publikation  
in der Deutschen Nationalbibliografie; detaillierte bibliografische  
Daten sind im Internet über <http://dnb.ddb.de> abrufbar.

Zugleich: Dissertation, Stuttgart, Univ., 2023

D 93

Das Werk ist urheberrechtlich geschützt.  
Sämtliche, auch auszugsweise Verwertungen bleiben vorbehalten.

Copyright © utzverlag GmbH 2023

Print ISBN 978-3-8316-5010-1  
Ebook ISBN 978-3-8316-7746-7

Printed in Germany

utzverlag GmbH, München  
Tel.: 089-277791-00 · [www.utzverlag.de](http://www.utzverlag.de)

# Table of contents

<b>Table of contents</b> .....	<b>5</b>
<b>Symbols and abbreviations</b> .....	<b>7</b>
<b>Kurzfassung in deutscher Sprache</b> .....	<b>17</b>
<b>Extended Abstract</b> .....	<b>20</b>
<b>1 Introduction</b> .....	<b>23</b>
1.1 Motivation .....	23
1.2 Analytical models for predicting the depth in micromachining with ultrashort laser pulses .....	25
1.3 Process monitoring and process control in laser micromachining of demanding applications .....	37
1.4 Process strategies for high-throughput laser milling with high energy efficiency and high surface quality .....	46
1.5 Summary of research needs .....	55
<b>2 Development and verification of analytical models for the depth progress during micromachining of geometries with high aspect ratios</b> .....	<b>57</b>
2.1 Analytical model for the depth progress of percussion drilling with ultrashort laser pulses.....	57
2.2 Analytical model for the depth progress during laser micromachining of V-shaped grooves .....	71
<b>3 Investigation of depth-controlled laser milling for reliably achieving the target depth in advanced applications</b> .....	<b>90</b>
3.1 High-quality net shape geometries from additively manufactured parts using closed-loop controlled ablation with ultrashort laser pulses .....	90
3.2 Additional results for additively manufactured parts built with support structures .....	107

---

3.3	Image processing based detection of the fibre orientation during depth-controlled laser ablation of CFRP monitored by optical coherence tomography .....	111
<b>4</b>	<b>Scaling the throughput of high-quality laser milling with a 1 kW sub-picosecond laser .....</b>	<b>137</b>
4.1	High-quality high-throughput silicon laser milling using a 1 kW sub-picosecond laser.....	137
4.2	Additional results for high-quality high-throughput laser milling of metals .....	148
<b>5</b>	<b>Conclusion .....</b>	<b>151</b>
	<b>References.....</b>	<b>155</b>
	<b>Danksagung.....</b>	<b>181</b>

## Symbols and abbreviations

$A$	-	absorptivity
$c_p$	J/(kg·K)	mass-specific heat capacity
$d$	μm	beam diameter
$D_a$	μm	mean deviation from the targeted net shape
$d_{abl}$	μm	ablation diameter
$d_c$	μm	cavity width
$d_G$	μm	groove width
$d_H$	μm	hole diameter
$d_0$	μm	beam diameter on sample surface
$e$	-	Euler's number
$E_B$	μJ or mJ	burst energy
$E_P$	μJ or mJ	pulse energy
$f$	mm	focal length
$f_B$	kHz	burst repetition rate
$f_P$	kHz	pulse repetition rate
$G$	-	number of pixels in $x$ -direction

---

$g$	-	integer for numbering of pixels in $x$ -direction
$H$	-	number of pixels in $y$ -direction
$h$	-	integer for numbering of pixels in $y$ -direction
$h_v$	J/mm <sup>3</sup>	volume-specific enthalpy for heating and vaporisation
$j$	-	integer for numbering the pulses during one scan
$j_{abl,m}$	-	maximum number of pulses contributing to ablation during one scan
$k$	-	integer for numbering the parallel lines during one scan
$M^2$		beam propagation factor
$m, M$	-	number of scans
$n, N$		number of pulses
$N_{beams}$	-	number of beams
$N_L$	-	number of parallel lines
$N_P$	-	number of pulses per line
$N_{ppb}$	-	number of pulses in burst
$N_R$	-	number of reflections until an incident ray leaves the V-shaped groove again
$P$	W	average laser power

---

$p_x$	$\mu\text{m}$	spatial offset between the impact locations of two consecutive pulses
$p_y$	$\mu\text{m}$	spatial offset between parallel hatching lines
$R_a$	$\mu\text{m}$	arithmetic average roughness measured along a line
$r_{\text{abl}}$	$\mu\text{m}$	ablation radius
$r_{\text{H}}$	$\mu\text{m}$	hole radius
$r(z)$	$\mu\text{m}$	radius along the hole depth $z$
$S^*$	-	incubation coefficient
$S_a$	$\mu\text{m}$	arithmetic average roughness measured over an area
$T$	$^{\circ}\text{C}$	temperature
$T_0$	$^{\circ}\text{C}$	ambient temperature
$v_{\text{crit}}$	$\text{m/s}$	critical scanning speed below which heat accumulation effects occur
$v_x$	$\text{m/s}$	scanning speed in $x$ direction
$\dot{V}$	$\text{mm}^3/\text{min}$	material removal rate
$w_{\text{lens}}$	$\text{mm}$	beam radius on the focusing lens
$w_0$	$\mu\text{m}$	radius of the beam waist
$w(z)$	$\mu\text{m}$	beam radius along the $z$ direction

---

$x$	$\mu\text{m}$	cartesian coordinate perpendicular to the propagation direction $z$ of the laser beam and perpendicular to the hatching direction $y$
$x_c$	$\mu\text{m}$	location of the centre of the beam along the $x$ -coordinate
$x_j$	$\mu\text{m}$	location of the centre of the beam at the time at which the $j^{\text{th}}$ pulse hits the workpiece
$x_0$	$\mu\text{m}$	location of a point with respect to the direction of $x$
$y$	$\mu\text{m}$	cartesian coordinate perpendicular to the propagation direction $z$ of the laser beam and perpendicular to the scanning direction $x$
$y_c$	$\mu\text{m}$	location of the centre of the beam along the $y$ -coordinate
$z$	$\mu\text{m}$	cartesian coordinate in propagation direction of the laser beam
$z_{\text{abl}}$	$\mu\text{m}$	ablation depth
$z_{\text{abl},n}$	$\mu\text{m}$	depth ablated by the $n^{\text{th}}$ pulse
$z_{\text{abl},m,j}$	$\mu\text{m}$	depth ablated by the $j^{\text{th}}$ pulse during the $m^{\text{th}}$ scan
$z_c$	$\mu\text{m}$	location of the focal plane of the beam along the $z$ -coordinate
$z_C$	$\mu\text{m}$	cavity depth
$z_{G,m}$	$\mu\text{m}$	groove depth after $m$ scans
$z_{G,\text{max}}$	$\mu\text{m}$	maximum achievable groove depth

---

$z_H$	$\mu\text{m}$	hole depth
$z_{H,n}$	$\mu\text{m}$	hole depth after $n$ pulses
$z_{H,\text{max}}$	$\mu\text{m}$	maximum achievable hole depth for high-quality holes
$z_R$	$\mu\text{m}$	Rayleigh length
$z_{S,m}$	$\mu\text{m}$	accumulated depth ablated by the $m^{\text{th}}$ scan
$z_T$	$\mu\text{m}$	target depth
$\alpha_{n-1}$	rad	solid angle
$\beta$	px	length of the normal segment
$\Delta V$	$\mu\text{m}^3$	volume ablated by a single pulse
$\Delta V_E$	$\mu\text{m}^3/\mu\text{J}$	energy-specific volume
$\Delta V_{E,\text{max}}$	$\mu\text{m}^3/\mu\text{J}$	maximum energy-specific volume
$\delta_{\text{eff}}$	nm	effective penetration depth
$\eta_{A,G}$	-	absorptance in the V-shaped groove
$\eta_{A,G,\infty}$	-	absorptance of a groove machined with $\infty$ scans
$\eta_{A,H,n}$	-	absorptance in a drilled hole after $n$ pulses
$\theta$	$^\circ$	angle of inclination of the normal segment perpendicular to the described line

---

$\theta_1$	°	angle of inclination of the pixel with the highest brightness in the $\theta$ - $\beta$ -Radon space matrix
$\kappa$	mm <sup>2</sup> /s	thermal diffusivity
$\lambda_L$	nm	wavelength of processing laser
$\lambda_O$	nm	wavelength of OCT probe beam
$\rho$	kg/m <sup>3</sup>	mass density
$\sigma_{n-1}$	-	ratio of the hole's opening to the complete surface area of the hole including the opening
$\tau_P$	ps or fs	pulse duration
$\phi(x)$	J/cm <sup>2</sup>	radiant fluence on the sample surface along the $x$ -coordinate
$\phi(y)$	J/cm <sup>2</sup>	radiant fluence on the sample surface along the $y$ -coordinate
$\phi_A(z)$	J/cm <sup>2</sup>	absorbed fluence along the hole depth $z$
$\phi_{A,G,m,j}$	J/cm <sup>2</sup>	radiant exposure in the tip of the groove by the $j^{\text{th}}$ pulse during the $m^{\text{th}}$ scan
$\phi_{A,H,n}$	J/cm <sup>2</sup>	absorbed fluence at the hole's tip
$\phi_{A,\text{th}}$	J/cm <sup>2</sup>	absorbed ablation threshold fluence
$\phi_{A,0}$	J/cm <sup>2</sup>	absorbed peak fluence
$\phi_{\text{th}}$	J/cm <sup>2</sup>	ablation threshold fluence
$\phi_0$	J/cm <sup>2</sup>	irradiated peak fluence

---

$\phi_{0,\text{opt}}$	J/cm <sup>2</sup>	optimum peak fluence with regard to energy-specific volume
$\Omega_x$	-	pulse overlap in scanning direction
$\Omega_y$	-	line overlap perpendicular to the scanning direction

Al	aluminium
AlSi10Mg	aluminium alloy
AR	anti reflection
ASTM	American Society for Testing and Materials
CCD	charge-coupled device
CFRP	carbon fibre-reinforced plastics
Cu	copper
CVD	chemical vapour deposition
cw	continuous wave
DIN	Deutsches Institut für Normung (German industry standard)
fs	femtosecond
He	helium

HR	high reflection
kHz	kilohertz
LCI	low coherence interferometry
LIPSS	laser-induced periodic surface structures
LPBF	laser powder bed fusion
LSM	laser scanning microscope
MEMS	micro-electro-mechanical systems
MEZ	matrix evaporation zone
MHz	megahertz
N <sub>2</sub>	nitrogen
Ni	nickel
OCT	optical coherence tomography
ps	picosecond
RMS	root-mean-square
SEM	scanning-electron-microscope
SNR	signal-to-noise ratio
sub-ps	sub-picosecond
THz	terahertz

Ti	titanium
Ti6Al4V	titanium alloy
VARI	vacuum-assisted resin infusion
µm	micrometre
3D	three dimensional



# Kurzfassung in deutscher Sprache

Die Lasermikrobearbeitung mit kurzen und ultrakurzen Laserpulsen ermöglicht eine besonders hohe Präzision und Qualität bei der Erzeugung verschiedenster Geometrien im Mikrometerbereich auf unterschiedlichen Materialien. Die Bandbreite der Verfahren und Geometrien reicht vom Perkussionsbohren von Mikrolöchern über das Gravieren von Nuten bis hin zum Lasermikrofräsen von einfachen Taschen oder komplexen Geometrien. Die Tiefe bzw. das Aspektverhältnis (Tiefe/Breite) der erzeugten Geometrie hat dabei meist einen großen Einfluss auf die Funktionalität der jeweiligen Anwendung.

Im Rahmen dieser Arbeit wurden Lasermikrobearbeitungsprozesse mit Zieltiefe im Hinblick auf die drei Aspekte analytische Modellierung des Tiefenfortschritts, tiefengeregelter Materialabtrag und Skalierung des Durchsatzes beim Volumenabtrag untersucht.

Die analytische Modellierung des Tiefenfortschritts ermöglicht die Berechnung der Bearbeitungstiefe in Abhängigkeit der Prozessparameter, um damit vor dem Bearbeitungsprozess die Prozessparameter entsprechend auslegen zu können. Zur Berechnung des Tiefenfortschritts von Geometrien mit hohen Aspektverhältnissen (Tiefe/Breite) wurden zwei analytische Modelle hergeleitet:

Das Modell für perkussionsgebohrte Mikrolöcher basiert auf den Annahmen eines konisch geformten Lochs, eines zunehmenden Einkoppelgrads mit zunehmendem Aspektverhältnis aufgrund diffuser Mehrfachreflexionen innerhalb des Lochs und der Annahme, dass die absorbierte Bestrahlung linear mit der Tiefe des Lochs zunimmt. Die theoretische Vorhersage des Modells stimmt gut mit experimentellen Ergebnissen für Löcher mit einer Tiefe von bis zu 1,5 mm in Edelstahl überein, die mit Pikosekunden-Laserpulsen gebohrt wurden.

Das Modell für gravierte Nuten basiert auf den Annahmen einer V-förmigen Nutform, eines zunehmenden Einkoppelgrads mit zunehmendem Aspektverhältnis aufgrund von spekulären Mehrfachreflexionen innerhalb der Nut und der Annahme,

dass die absorbierte Bestrahlung linear mit der Tiefe der Nut zunimmt. Die theoretische Vorhersage stimmt gut mit den experimentellen Ergebnissen für Nuten bis zu einer Tiefe von 624  $\mu\text{m}$  in einer Ti-Legierung überein, die mit Femtosekunden-Laserpulsen erzeugt wurden.

Die Messung und Regelung der Bearbeitungstiefe während der Mikrobearbeitung stellt sicher, dass die entsprechende Zieltiefe durch Anpassung der Prozessparameter erreicht wird. In der vorliegenden Arbeit wurde ein tiefengeregelter Materialabtrag durch eine in-situ Messung der lokalen Bearbeitungstiefe mittels optischer Kohärenztomographie und entsprechender Ansteuerung der Strahlquelle realisiert und dessen Potenzial anhand von zwei Anwendungen demonstriert:

Mittels pulverbettbasiertem Laserschmelzen generierte Metallbauteile erfordern aufgrund von Materialüberschüssen aus Stützstrukturen, Abweichungen von der angestrebten Nettoform und hohen Oberflächenrauigkeiten meist eine Nachbearbeitung. Das tiefengeregelte Abtragen mit ultrakurzen Laserpulsen ermöglichte die Detektion von überstehendem Material sowie einen lokal angepassten Abtrag. Dadurch konnten automatisiert Blockstützstrukturen entfernt sowie die Formabweichung und Oberflächenrauigkeit um 63% bis 81% auf 15  $\mu\text{m}$  bzw. 5  $\mu\text{m}$  reduziert werden.

Bei der Reparatur von Bauteilen aus carbonfaserverstärkten Kunststoffen ist ein schichtgenaues Abtragen der geschädigten Bereiche als Vorbereitung für den Wiederaufbau des Bauteils mit passgenauen Reparaturlagen erforderlich. Die in-situ Messung der Oberflächentopographie beim Abtragen von carbonfaserverstärkten Kunststoffen ermöglichte die bildverarbeitungsbasierte Bestimmung der lokalen Faserorientierung. Die Bestimmung der Faserorientierung mit einer Winkelgenauigkeit von besser als  $\pm 4^\circ$  wiederum ermöglichte die zuverlässige Erkennung des Übergangs zwischen zwei benachbarten Schichten, um damit den Abtragsprozess stoppen oder die bearbeitete Geometrie verändern zu können, ohne die jeweilige Schichtdicke oder Zieltiefe im Voraus zu kennen.

Die Skalierung der Mikrobearbeitungsprozesse zu hohen mittleren Laserleistungen unter Beibehaltung der geforderten Qualität und Präzision ermöglicht einen hohen Durchsatz und das Erreichen der Zieltiefe in einer kurzen Prozesszeit.

Mit einem am Institut für Strahlwerkzeuge selbstgebauten Ultrakurzpuls laser mit einer mittleren Leistung von über 1 kW wurde das Laserabtragen von Silizium und

---

Metallen untersucht. Durch Anwendung geeigneter Bearbeitungsstrategien wie Bursts, niedrigen Bestrahlungen und hohen Scangeschwindigkeiten konnte der Durchsatz beim Abtragen bei gleichbleibend hoher Oberflächenqualität deutlich erhöht werden. Am Beispiel von Silizium konnte in dieser Arbeit die Volumenabtragsrate im Vergleich zum Stand der Forschung um mehr als den Faktor 224 auf  $230 \text{ mm}^3/\text{min}$  gesteigert und gleichzeitig eine niedrige Rauheit von  $\leq 0,6 \text{ }\mu\text{m}$  bis zu mehreren hundert Mikrometern Bearbeitungstiefe beibehalten werden. Mit derselben Strategie konnten auch hohe Volumenabtragsraten von  $180 \text{ mm}^3/\text{min}$ ,  $174 \text{ mm}^3/\text{min}$  und  $126 \text{ mm}^3/\text{min}$  bei der Bearbeitung von Edelstahl, Aluminium und Kupfer erzielt werden.

## Extended Abstract

Laser micromachining with short and ultrashort laser pulses enables particularly high precision and quality in the creation of a wide variety of geometries in the micrometre range on different materials. The range of processes and geometries extends from percussion drilling of microholes and engraving of grooves to laser micromilling of simple pockets or complex geometries. The depth or aspect ratio (depth/width) of the generated geometry usually has a major influence on the functionality of the respective application.

In this thesis, laser micromachining processes with target depth were investigated with regard to the three aspects of analytical modelling of the depth progress, depth-controlled micromachining and scaling of the throughput in volume ablation.

The analytical modelling of the depth progress enables to predict the machining depth depending on the process parameters which helps to design and plan a given process. Two analytical models were derived to calculate the depth progress of geometries with high aspect ratios (depth/width):

The model for percussion-drilled microholes is based on the assumptions of a conically-shaped hole, increasing absorptance with increasing aspect ratio due to diffuse multiple reflections within the hole and the assumption that the absorbed fluence increases linearly along the depth of the hole. The theoretical prediction of the model agrees well with experimental results for holes with a depth of up to 1.5 mm in stainless steel drilled with picosecond laser pulses.

The model for engraved grooves is based on the assumptions of a V-shaped groove, increasing absorptance with increasing aspect ratio due to specular multiple reflections within the groove, and the assumption that the absorbed fluence increases linearly along the depth of the groove. The theoretical prediction agrees well with the

---

experimental results for grooves with a depth of up to 624  $\mu\text{m}$  in a Ti alloy engraved with femtosecond laser pulses.

Measuring and controlling the depth during micromachining ensures that the corresponding target depth is achieved by adjusting the process parameters. Depth-controlled material removal was realised in the present work by the in-situ measurement of the local depth using optical coherence tomography and the corresponding control of the beam source, and the potential was demonstrated by means of two applications:

Metal components generated by laser powder bed fusion usually require post-processing due to excess material from support structures, deviations from the targeted net shape and high surface roughness. Depth-controlled laser milling with ultrashort laser pulses enabled the locally adapted machining based on the measurement of the excess material. This made it possible to automatically remove block support structures and to reduce the shape deviation and surface roughness by 63% to 81% to 15  $\mu\text{m}$  and 5  $\mu\text{m}$ , respectively.

When repairing components made from carbon fibre-reinforced plastics (CFRP), it is necessary to remove the damaged areas with layer accuracy in preparation for rebuilding the component with precisely fitting repair layers. The in-situ measurement of the surface topography during laser milling of CFRP enabled the image processing-based determination of the local fibre orientation. The determination of the fibre orientation with an angular accuracy of better than  $\pm 4^\circ$ , in turn, enabled the reliable detection of the transition between two adjacent layers, so that the laser milling process could be stopped or the machined geometry changed between layers without knowing the respective layer thickness or target depth in advance.

Scaling the micromachining processes to high average laser powers while maintaining the required quality and precision enables high throughput and reaching the target depth in a short process time.

Laser milling of silicon and metals was investigated using an ultrafast laser with an average power of over 1 kW developed at the Institut für Strahlwerkzeuge. By applying suitable processing strategies such as bursts, low fluences and high scanning speeds, the throughput of laser milling could be significantly increased while maintaining high surface quality. For the example of silicon, the volume removal rate was

increased by more than a factor of 224 to 230 mm<sup>3</sup>/min compared to the state of the art while maintaining a low roughness of  $\leq 0.6$   $\mu\text{m}$  up to a machining depth of several hundred micrometres. The same strategy was also used to achieve high volume removal rates of 180 mm<sup>3</sup>/min, 174 mm<sup>3</sup>/min, and 126 mm<sup>3</sup>/min when machining stainless steel, aluminium, and copper, respectively.

# 1 Introduction

## 1.1 Motivation

The strong individualisation of products under the conditions of flexible production is an essential component in order to actively shape the fourth industrial revolution of the German future project *Industry 4.0* [1]. The flexible production of individualized products enables new business models, such as mass customisation [2,3], and the production of spare parts on demand [4]. Flexible production requires highly flexible manufacturing systems that can address different processes for the processing of different materials. As a universal tool, the laser can cover at least one process from each of the main processing groups defined in DIN8580 – primary forming, forming, separating, joining, coating, and changing material properties [5]. In the area of separation, laser micromachining with short and ultrashort laser pulses offers particularly high precision and quality in the creation of a wide range of geometries on the micrometre scale in different materials. The bandwidth of processes and geometries ranges from percussion drilling of microholes to engraving of grooves to micromilling of simple pockets or complex geometries [6,7]. The depth or aspect ratio (depth/width) of the machined geometry often has a major influence on the functionality of the respective application: Microholes with a high aspect ratio are required in spinnerets to be able to draw the thinnest possible microfibres and at the same time to be able to use the required material thickness for a stiff spinneret [8]. Lower cutting forces and shorter chips can be realised in mechanical machining of aluminium with cutting tools by grooves with high aspect ratios engraved on the cutting edge [9]. For the fabrication of transmissive silicon optics for high-power THz radiation by laser milling, the design depth must be achieved at every point of the fabricated optical elements so that the THz radiation is diffracted as desired [10].

The concept of "*first time right*" from the field of quality management [11] is particularly relevant in the context of mass customisation, because here a start-up phase to

optimise the production process for each product variant, as typically required in series and mass production, is not economical. For manufacturing by means of laser micromachining, this means that the laser parameters must be set accordingly for each target geometry or target depth and each processed material already at the start of the machining process. The amount of material removed during laser micromachining depends on the properties of the laser beam (e.g. wavelength, pulse duration, pulse energy) as well as the optical and thermophysical properties of the workpiece (e.g. absorption, energy penetration depth, vaporisation enthalpy) [12]. The exact prediction of the required process parameters as well as the resulting machining depth is difficult due to the interplay of the different parameters. However, a good estimate can be made in a short calculation time with the help of analytical models in order to design the process parameters accordingly. In case of the need for an increased precision of the machining depth, the prior estimation by analytical models can be combined with the measurement of the local ablation depth to adjust the process parameters during machining. The latter also offers the advantages of automation as well as the possibility to assign a measured quality proof to each machined geometry [13,14].

A correspondingly high productivity is required in manufacturing of each product variant for profitable mass customisation [15]. The geometries created by laser micromachining must therefore not only meet requirements for quality and precision but must also be realised with a high throughput [16], which corresponds to achieving the target depth in the shortest possible time. The machining processes should also be designed to be energy-efficient due to the limited laser power of industrially available laser beam sources in the range of a few 100 W [17] and against the background of sustainable, energy-saving manufacturing processes [18].

The following three aspects are therefore relevant for the production of mass customized products "*first time right*" with simultaneous high throughput by means of laser micromachining: First, the analytical modelling of the depth progress for predicting the machining depth in advance in order to be able to set out appropriate process parameters. Secondly, depth monitoring and control during the micromachining process to ensure that the corresponding target depth is reached with the required precision by adjusting the process parameters. Thirdly, the process scaling to high average laser powers and throughputs while maintaining the required quality and precision to achieve the target depth in a short process time. The state of the art

is described in the following for each of these three aspects to show the need for research and the objectives for this work in the respective field.

## 1.2 Analytical models for predicting the depth in micromachining with ultrashort laser pulses

### 1.2.1 State of research

Micromachining with ultrashort laser pulses has become a reliable tool for industrial applications that require locally selective material removal with high precision [7]. Micromachining with a relative movement between the laser beam and the work-piece enables the fabrication of different geometries. A selection of common geometries and the relative movement required is shown in Figure 1.1.

Percussion drilling describes a drilling process with a static beam and results in conically-shaped holes with a diameter  $d_H$  and a depth  $z_H$ . The depth of a hole can be increased by applying multiple pulses at the same location. Engraving with a moving beam with a pulse spacing of  $p_x$  leads to V-shaped grooves with a width  $d_G$  and a depth  $z_G$ . The depth of a groove can be increased by multiple passes over the same contour. Laser milling with a moving beam along multiple parallel lines with a spacing of  $p_y$  results in cavities with a width  $d_C$  and a depth  $z_C$ . The depth of a cavity can be increased by making multiple passes along parallel lines.

Predicting the amount of material removed during laser micromachining of these geometries is difficult due to the interplay of the process parameters (e.g. wavelength, pulse duration, pulse energy, ...) and material properties (e.g. absorption, energy penetration depth, vaporisation enthalpy, ...) [12]. However, the machining depth can be well estimated using analytical models by making some simplifications, e.g. specifying vaporisation-based material removal. The fundamentals of material removal with single and repetitive ultrashort laser pulses are presented in the following. The state of the art of analytical models for predicting the depth in percussion drilling of holes, engraving of grooves and laser milling of cavities is then presented and compared with experimental results for each process.

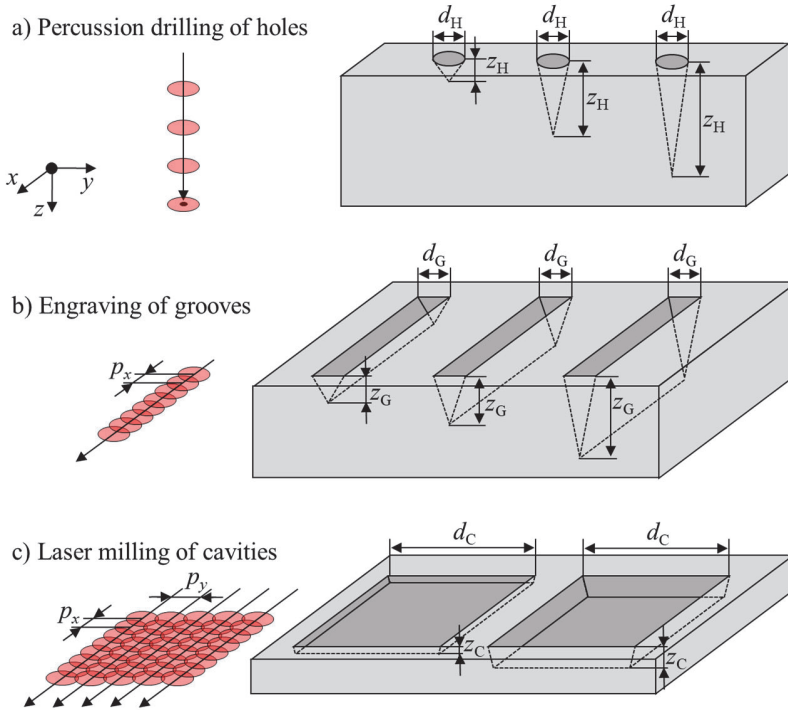


**Figure 1.1** Different machining strategies (left) to create different geometries (right): a) Percussion drilling with a static beam results in conically-shaped holes with a diameter  $d_H$  and a depth  $z_H$ . b) Engraving with a moving beam in the  $x$ -direction with a pulse spacing of  $p_x$  leads to V-shaped grooves with a width  $d_G$  and a depth  $z_G$ . c) Laser milling with a moving beam in  $x$ -direction along multiple parallel lines with a spacing of  $p_y$  results in cavities with a width  $d_C$  and a depth  $z_C$ .

### 1.2.1.1 Laser beam parameters

Micromachining of geometries with dimensions in the  $\mu\text{m}$ -range requires a corresponding size of the tool. Thus, a given laser beam with a wavelength  $\lambda_L$  and a beam propagation factor  $M^2$  has to be focused by a lens with focal length  $f$  onto the surface of the sample that is to be machined. The radius of the waist of the focused beam is given by [19]

$$w_0 = \frac{M^2 \cdot \lambda_L \cdot f}{\pi \cdot w_{\text{lens}}} \quad (1.1)$$

for a collimated beam with a beam radius  $w_{\text{lens}}$  on the focusing lens. As the input parameters are usually known from data sheets of the applied laser and optics, Eq. (1.1) allows for a fast calculation of the beam waist radius  $w_0$ . The beam waist radii are typically in the order of a few  $\mu\text{m}$  up to a few hundred  $\mu\text{m}$  for industrially available ultrafast lasers and focusing optics for infrared radiation with a wavelength of  $\lambda_L \approx 1 \mu\text{m}$  [20–24]. The beam radius  $w_{\text{lens}}$  on the focusing lens can be adapted by means of a telescope to further increase the range of available beam waist radii. The evolution of the beam radius is given by [19]

$$w(z) = w_0 \cdot \sqrt{1 + \frac{(z - z_c)^2}{z_R^2}}, \quad (1.2)$$

where  $z - z_c$  denotes the axial distance from the position of the waist and where

$$z_R = \frac{\pi \cdot w_0^2}{M^2 \cdot \lambda_L} \quad (1.3)$$

is the Rayleigh length [19]. At  $\lambda = 1 \mu\text{m}$ , the Rayleigh lengths for the exemplary beam radii from a few  $\mu\text{m}$  up to a few hundred  $\mu\text{m}$  range from a few tens of  $\mu\text{m}$  up to a few hundred of mm, respectively. The wide range of possible beam radii and Rayleigh lengths highlight the potential geometric differences in beam propagation depending on the choice of laser system and optics.

The cross-sectional distribution of the energy density per unit area of a circular Gaussian laser beam is given by the fluence

$$\phi(x, y, z) = \phi_0 \cdot \left( \frac{w_0}{w(z)} \right)^2 \cdot \exp \left( -2 \frac{(x - x_c)^2 + (y - y_c)^2}{w^2(z)} \right), \quad (1.4)$$

where  $x - x_c$  and  $y - y_c$  are the distances from the axis of the laser beam located at  $(x_c, y_c)$  and  $\phi_0$  denotes the peak fluence

$$\phi_0 = \frac{2 \cdot E_P}{\pi \cdot w_0^2}, \quad (1.5)$$

where  $E_P$  is the energy of the irradiated laser pulse [19]. The distribution of the irradiated fluence at normal incidence and for a sample located in the plane of the waist ( $z = z_c = 0$ ) is therefore given by

$$\phi(x, y) = \phi_0 \cdot \exp\left(-2 \frac{(x - x_c)^2 + (y - y_c)^2}{w_0^2}\right). \quad (1.6)$$

### 1.2.1.2 Single-pulse ablation

Material removal by ablation occurs when the locally irradiated fluence  $\phi(x, y)$  exceeds the value of the material-specific ablation threshold

$$\phi_{\text{th}} = \frac{\delta_{\text{eff}} \cdot h_V}{A}, \quad (1.7)$$

where  $\delta_{\text{eff}}$  is the effective penetration depth of the absorbed energy density,  $h_V$  denotes the enthalpy required for heating and complete vaporisation of the material and  $A$  is the material-specific absorptivity at the wavelength  $\lambda_L$  of the incident radiation at normal incidence on a flat surface. The effective penetration depth  $\delta_{\text{eff}}$  and thus the ablation threshold  $\phi_{\text{th}}$  are dominated either by the optical penetration depth or by the diffusion length of hot electrons depending on the irradiated fluence. Two regimes were observed in experimental investigations. In the low-fluence regime, the penetration depth is shorter and determined by the optical penetration depth. In the high-fluence regime, the penetration depth is longer and determined by the diffusion length of hot electrons [25,26]. In practice, the effective penetration depth is usually determined experimentally for the given processing setup since the effective penetration depth cannot be easily calculated. Not only vaporisation but also melt formation and spallation occur during ablation [27] and can result in a differing effective process enthalpy depending on the duration of the laser pulses and the absorbed

fluence. The absorptivity  $A$  can be calculated using the Fresnel equations, the refractive index and the extinction coefficient for an ideal flat surface without contamination [28]. In practice, the absorptivity can however vary depending on the surface conditions of the irradiated material, such as the surface roughness and the presence of an oxide layer [12].

Material ablation occurs when the locally irradiated fluence  $\phi(x,y)$  exceeds the ablation threshold  $\phi_{th}$ . When a Gaussian beam is used at normal incidence the local ablation depth can then be expressed by [29]

$$z_{abl}(x,y) = \delta_{eff} \cdot \left\{ \ln \left( \frac{\phi_0}{\phi_{th}} \right) - 2 \cdot \frac{x^2 + y^2}{w_0^2} \right\}. \quad (1.8)$$

As a result, craters of parabolic shape are generated on the sample surface. The maximum depth [25]

$$z_{abl} = \delta_{eff} \cdot \ln \left( \frac{\phi_0}{\phi_{th}} \right) \quad (1.9)$$

is obtained in the centre of the crater ( $x = y = 0$ ) whose transversal dimension is given by the ablation radius [30]

$$r_{abl} = w_0 \cdot \sqrt{\frac{1}{2} \cdot \ln \left( \frac{\phi_0}{\phi_{th}} \right)}. \quad (1.10)$$

The values of the ablation threshold and energy penetration depth in the case of the irradiation with ultrashort laser pulses were experimentally determined and are reported in numerous publications [26,31,32] for commonly processed metals such as stainless steel, copper, aluminium and titanium. Using the method presented in [30], the ablation threshold  $\phi_{th}$  for single pulses was determined at a wavelength of 1  $\mu\text{m}$  to be in the range  $0.2 \text{ J/cm}^2 \leq \phi_{th} \leq 3.5 \text{ J/cm}^2$  depending on the irradiated metal. The effective penetration depth for single pulses was measured to be  $\delta_{eff} < 100 \text{ nm}$  [32]. The maximum crater depth  $z_{abl}$  in metals resulting from irradiation with a single pulse

is therefore typically  $< 1 \mu\text{m}$ , even for fluences  $\phi_0$  about 100 times above the ablation threshold  $\phi_{\text{th}}$  (cf. Eq. (1.9)).

### 1.2.1.3 Incubation

The limited depth achieved with single pulses means that a location has to be irradiated by multiple pulses for micromachining of geometries with a depth  $> 1 \mu\text{m}$ . Irradiation with multiple pulses changes the surface condition of the irradiated sample due to the accumulation of laser-induced structural and chemical changes and plastic deformation of the surface [26,33]. As a result, the experimentally determined ablation threshold decreases with increasing number of irradiated pulses. This so called-incubation effect was first described by *Jee et al.* with the empirical model [33]

$$\phi_{\text{th}}(n) = \phi_{\text{th},1} \cdot n^{S^*-1}, \quad (1.11)$$

where  $\phi_{\text{th}}(n)$  denotes the ablation threshold after a number of  $n$  irradiated pulses,  $\phi_{\text{th},1}$  is the ablation threshold for a single pulse and  $S^*$  is the incubation coefficient that characterizes the extent to which incubation influences the material. For  $S^* = 1$  no changes occur in the material and the ablation threshold remains independent of the number of pulses [33]. An incubation coefficient in the range  $0.77 \leq S^* \leq 0.92$  [26,31,34] was measured for metals and at low pulse repetition rates, resulting in a reduction of the ablation threshold by a factor of about four to five between the first and the hundredth pulse. However, the model described in Eq. (1.11) converges to zero for an infinite high number of pulses, which is not physically correct and which is also not confirmed by experiments with up to  $n = 250,000$  pulses in [34]. In reality, the measured ablation threshold converges to a constant value and does not significantly change after more than 1,000 pulses. Modified empirical models that take into account the convergence to a constant ablation threshold for up to an infinite number of pulses are described in [34–36]. From Eq. (1.7) it can be deduced that the reduction of the ablation threshold with an increasing number of pulses can be attributed to a reduction of the effective penetration depth or an increased absorptivity or both. A direct correlation between the measured ablation threshold and measured effective penetration depth was observed in the experiments presented in [36] for copper and it was concluded that the incubation effect is mainly driven by a change in the effective penetration depth. Absorptivity measurements on gold samples irradiated by a

different number of pulses however showed an increased absorptivity of up to a factor of four when irradiated with up to 1,000 pulses. The increased absorptivity was attributed to an increased roughness resulting from laser-induced surface structures [37]. The experimental results show that the cause for the incubation effect has not been conclusively clarified yet but seems to be a superposition of different material properties changed by irradiation with multiple pulses.

#### 1.2.1.4 Heat accumulation

Only a fraction of the energy absorbed from each laser pulse contributes to the vapourisation and the ablation of the irradiated material and another fraction remains in the surrounding area as residual heat. When this fraction of residual heat  $\eta_{\text{res}}$  from the first pulse has not completely dissipated into the sample by heat conduction before a second pulse is applied, the second pulse interacts with preheated material and the residual heat of this second pulse heats the surface even further. The heating of the surface from subsequent pulses is commonly referred to as heat accumulation [38,39]. The temperature increase resulting from multiple repetitive pulses can be calculated as a function of the process parameters and material properties with the model presented in [38]. Assuming a point source on the surface of a half-infinite body with a 3D heat flow, the temperature immediately before the incidence of the  $(N+1)^{\text{th}}$  pulse is found to be [40]

$$T(n) = T_0 + \frac{2 \cdot \eta_{\text{res}} \cdot E_p \cdot f_p^{3/2}}{\rho \cdot c_p \cdot (4 \cdot \pi \cdot \kappa)^{3/2}} \cdot \sum_{n=1}^N \frac{1}{n^{3/2}}, \quad (1.12)$$

where  $T_0$  is the ambient temperature,  $\eta_{\text{res}}$  denotes the fraction of the pulse energy that remains in the surrounding area as residual heat,  $f_p$  is the pulse repetition rate,  $\rho$  is the mass density,  $c_p$  is the specific heat capacity, and  $\kappa$  is the thermal diffusivity. For a given set of process parameters and a specific material, the model allows to determine the process limits, e.g. a critical number of pulses that can be applied to a location before the melting temperature is reached on the surface [40]. Exceeding the melting temperature would lead to a melt-dominated machining process, whose result would significantly deviate from the prediction of an analytical model based on vapourisation-dominated material removal.

### 1.2.1.5 Laser percussion drilling of holes

The consequence of the reduction of the ablation threshold  $\phi_{\text{th}}(n)$  with increasing number of pulses  $n$  due to the incubation effect is that the dimensions of holes that are percussion-drilled by multiple pulses also depend on the number of applied pulses. The diameter  $d_{\text{H}}(n)$  of a hole drilled with a Gaussian beam with a peak fluence  $\phi_0$ , a radius  $w_0$ , and  $n$  pulses is given by [41,42]

$$d_{\text{H}}(n) = 2 \cdot r_{\text{abl}}(n) = 2 \cdot w_0 \cdot \sqrt{\frac{1}{2} \cdot \ln \left( \frac{\phi_0}{\phi_{\text{th}}(n)} \right)}. \quad (1.13)$$

For holes drilled with  $n > 1,000$  pulses, the diameter does not increase further with increasing number of pulses  $n$  [43], as the ablation threshold remains almost constant for a higher number of pulses. According to [44] the depth  $z_{\text{H}}$  of the percussion-drilled hole can be expressed by

$$z_{\text{H}}(n) = n \cdot \delta_{\text{eff}} \cdot \ln \left( \frac{\phi_0}{\phi_{\text{th}}} \right), \quad (1.14)$$

which would imply a linear depth progress and that the hole depth can be unlimitedly increased by simply increasing the applied number of pulses. In practice, an approximately linear depth progress was however only observed for shallow holes in metals and semiconductors with up to a few thousand applied pulses and with a depth of up to a few hundred  $\mu\text{m}$  [13,45–47]. Drilling beyond this depth is characterized by an irregular drilling process with gradually decreasing drilling rate until the drilling progress ceases and the maximum hole depth is reached [45,46]. Conical hole geometries are formed during percussion drilling of deep holes with ultrashort laser pulses [43,47–50]. This led to the definition of a depth limit when the local fluence is equal to the ablation threshold everywhere on the walls of the conically-shaped hole [49]. A simple model for the estimation of the depth limit was introduced in [49] and is given with minor modifications made in [17] by

$$z_{H,\max} \approx w_0 \cdot \sqrt{\frac{\left(\frac{\phi_0 - \phi_{th}}{A}\right)^2 - \phi_{th}^2 \cdot \ln^2\left(\frac{\phi_0}{\phi_{th}}\right)}{2 \cdot \phi_{th}^2 \cdot \ln\left(\frac{\phi_0}{\phi_{th}}\right)}}. \quad (1.15)$$

It can be seen from Eq. (1.15) that the maximum achievable depth  $z_{H,\max}$  of a hole in a specific material with the absorptivity  $A$  and ablation threshold  $\phi_{th}$  is determined by the peak fluence  $\phi_0$  or the pulse energy  $E_P$  (cf. Eq. (1.5)) and the beam radius  $w_0$ , which is defined by the laser beam source and the focusing setup (cf. Eq. (1.1)).

### 1.2.1.6 Laser engraving of grooves

Grooves are micromachined by means of a relative movement between the laser beam and the workpiece, which is created either by deflecting the laser beam over the processed surface using a scanner system or by moving the workpiece past the stationary beam by means of a linear axis. Moving the beam over the surface with a speed  $v_x$  results in a distance

$$p_x = \frac{v_x}{f_P}, \quad (1.16)$$

between the impact locations of consecutive pulses with a repetition rate  $f_P$ . The distance  $p_x$  in direction of movement should not exceed the ablation diameter  $2 \cdot r_{abl}$  to fabricate a groove with a continuous centre line. In order to obtain a groove with a constant width

$$d_G = 2 \cdot r_{abl} = 2 \cdot w_0 \cdot \sqrt{\frac{1}{2} \cdot \ln\left(\frac{\phi_0}{\phi_{th}}\right)}, \quad (1.17)$$

cf. Eq. (1.10),  $p_x$  should be significantly smaller than the ablation diameter since the laser beam and thus the ablated area are usually circular. The overlap

$$\Omega_x = 1 - \frac{p_x}{2 \cdot w_0} \quad (1.18)$$

can be used to express the degree of overlap of the area irradiated by consecutive pulses in the feed direction  $x$ . An approximately constant groove width  $d_G$  is achieved in single-pass micromachining when  $\Omega_x > 70\%$  [51]. In practice, multiple scans over the same contour are often required to produce grooves with a desired depth while avoiding heat accumulation defects that can result from multiple pulses during one scan. In multi-pass micromachining, a constant groove width  $d_G$  can already be achieved at lower pulse overlaps  $\Omega_x > 30\%$  [51], which facilitates the avoidance of heat accumulation defects from multiple pulses during a scan. An analytical model for the calculation of the groove depth  $z_G$  based on the ablation of multiple overlapping craters is proposed in [52]. The groove depth  $z_G(y)$  in the cross-section of the  $y$ - $z$ -plane (perpendicular to the scanning direction  $x$ ) can be calculated as a function of the process parameters with this model. With the assumption of constant material properties and using the modification made in [44] for multiple scans  $m$  one finds

$$z_G(y) = m \cdot \frac{\sqrt{2} \cdot p_x \cdot \delta_{\text{eff}}}{3 \cdot w_0} \cdot \sqrt{\ln\left(\frac{\phi_0}{\phi_{\text{th}}}\right) - \frac{2 \cdot y^2}{w_0^2}} \cdot \left( \frac{2 \cdot w_0^2}{p_x^2} \left( \ln\left(\frac{\phi_0}{\phi_{\text{th}}}\right) - \frac{2 \cdot y^2}{w_0^2} \right) - 1 \right). \quad (1.19)$$

The maximum groove depth is obtained in the centre of the groove at  $y=0$ . As in the case of the calculation of the hole depth (cf. Eq. (1.14)), Eq. (1.19) also implies a linear depth progress and that the groove depth can be unlimitedly increased by simply increasing the number of scans  $m$  along the contour. Again, a constant deepening rate was however only observed for micromachining of shallow grooves with depths in the range of tens of  $\mu\text{m}$  [53,54]. Micromachining beyond these depths is characterized by a V-shaped groove geometry and a machining process with gradually decreasing deepening rate until the depth progress ceases and the maximum groove depth is reached [53–55].

**1.2.1.7 Laser milling of cavities**

Cavities are micromachined by means of a two-dimensional relative movement between the laser beam and the workpiece in a rasterized manner. The scanning of parallel lines with a respective line spacing  $p_y$  results in the degree of overlap

$$\Omega_y = 1 - \frac{p_y}{2 \cdot w_0} \tag{1.20}$$

in the direction of  $y$  perpendicular to the propagation direction  $z$  of the laser beam and perpendicular to the scanning direction  $x$ . Analogous to the overlap  $\Omega_x$ , homogeneous ablation with a minimized influence of the circular beam shape and Gaussian intensity distribution can be achieved with overlaps  $\Omega_y > 70\%$  [56]. The width  $d_C$  of a cavity is given by

$$d_C = (N_L - 1) \cdot p_y + 2 \cdot r_{abl}, \tag{1.21}$$

where  $N_L$  is the number of parallel lines. As in the case of grooves, multiple scans along the parallel lines are often required to produce cavities of a desired depth while avoiding heat accumulation defects. An analytical model for the calculation of the cavity depth  $z_C(x,y)$  based on overlapping craters is proposed in [57]. According to this model, the cavity depth  $z_C(x,y)$  can be calculated as a function of the process parameters and for the assumption of constant material properties by

$$z_C(x,y) = m \cdot \sum_{j=0}^{N_P} \sum_{k=0}^{N_L} \left( \delta_{\text{eff}} \cdot \left( \ln \left( \frac{\phi_0}{\phi_{th}} \right) - \frac{2(x + j \cdot p_x)^2}{w_0^2} - \frac{2(y + k \cdot p_y)^2}{w_0^2} \right) \right) \tag{1.22}$$

where  $N_P$  is the number of pulses per line and  $j$  and  $k$  are integers numbering the successive pulses and parallel lines, respectively. A region of constant depth can only be achieved in the central area of the cavity since a tapered wall is formed due to the Gaussian fluence distribution [58]. Eq. (1.26) implies a linear depth progress and that the cavity depth can be unlimitedly increased by simply increasing the number of scans along the parallel lines. In contrast to holes and grooves, the constant deepening rate predicted by this model has been experimentally confirmed in numerous

publications for different process parameters, for different materials, and cavity depths of up to several millimetres: A constant deepening rate was measured in micromachining of cavities with  $\phi_0 = 5.3 \text{ J/cm}^2$  and with up to  $m = 200$  scans for different metals (Ti, Al, Cu) and cavity depths exceeding  $350 \text{ }\mu\text{m}$  [59]. Almost constant depth progress was also measured for micromachining of cemented tungsten carbide with  $\phi_0 = 17.3 \text{ J/cm}^2$  and with up to  $m = 100$  scans for cavity depths exceeding  $4 \text{ mm}$  [60].

### 1.2.2 Research needs

The constant deepening rate observed in drilling of shallow holes, in engraving of shallow grooves and in milling of cavities can be explained by constant processing parameters: As long as the bottom of the ablated geometry is flat, the irradiated laser beam is absorbed at normal incidence and the absorptivity  $A$  and fluence  $\phi$  remain constant (assuming  $z_R \gg z_C$ ). It can, however, be assumed that this behaviour is limited to a certain aspect ratio of the respective geometry, which is indicated by the cross-sections of laser-milled cavities shown in [59,60] with a decreasing width of the area of the bottom and increasing width of the tapered walls. The aspect ratio remains  $z_C/d_C < 2$  during laser milling of cavities with typical depths in the range of a few micrometres up to a few hundred micrometres [59,60]. The analytical model shown in Eq. (1.22) therefore provides a useful tool to predict the cavity depth in a wide range of commonly milled depths.

The constant deepening rate observed in drilling of holes was limited to aspect ratios ( $z_H/d_H$ ) in the order of 2 to 5 [45–47] and the constant deepening rate observed in engraving of grooves was limited to aspect ratios ( $z_G/d_G$ ) in the order of 1.5 to 3 [53,54]. In both cases, the decreasing deepening rate at higher aspect ratios can be explained by changing processing parameters. The irradiated area and the angle of incidence increase with increasing depth of the geometry due to the formation of tapered walls during micromachining with a Gaussian fluence distribution. The tapered walls are responsible for the characteristic cone-shape of holes and V-shape of grooves observed in drilling and engraving, respectively. The increasing angle of incidence with increasing depth changes the absorptivity according to the Fresnel equations [28]. Raytracing simulations revealed that rays reflected from the tapered walls can be absorbed multiple times along the walls of the hole or the groove, which

increases the total absorptance and changes the distribution of the absorbed fluence [61].

Analytical models for the calculation of the processing depth as a function of process parameters and material properties have been published only for shallow holes and shallow grooves with low aspect ratios and constant deepening rate before the start of this thesis. There is a need for research in the development of analytical models for the calculation of the depth progress of holes and grooves, which take into account the decreasing and ceasing deepening rate and thus enable the calculation of the depth progress from holes and grooves with high aspect ratios.

The first objective of the present work was to develop and experimentally verify an analytical model for calculating the depth progress of percussion-drilled holes in metals based on the assumptions of a conically shaped hole throughout the drilling process and an increasing absorptance as the aspect ratio of the hole increases.

The second objective of this work was to develop and experimentally verify an analytical model for calculating the depth progress of micromachined grooves in metals based on the assumptions of a V-shaped groove throughout the micromachining process and an increasing absorptance as the aspect ratio of the groove increases.

## 1.3 Process monitoring and process control in laser micromachining of demanding applications

### 1.3.1 State of research

Analytical modelling of the depth progress is a valuable tool for estimating the result obtained with a given set of process parameters and given material properties. While the properties of the laser beam can be precisely characterized by corresponding measurement devices, some material properties, such as the effective penetration depth  $\delta_{\text{eff}}$  and thus also the ablation threshold  $\phi_{\text{th}}$ , are not easy to determine and require involved experiments. The accuracy of the experimental determination is limited due to the limited precision and reproducibility of the measurements. For example, the measured ablation threshold  $\phi_{\text{th}}$  differed by almost 80% with  $\phi_{\text{th}} = 0.28 \text{ J/cm}^2$

reported in [62] and  $\phi_{th} = 0.50 \text{ J/cm}^2$  reported in [31] when using the method reported in [30] for similar process parameters of  $1030 \text{ nm} \leq \lambda_L \leq 1064 \text{ nm}$ ,  $\tau_p = 10 \text{ ps}$ ,  $100 \leq n \leq 128$ , and  $10.0 \text{ } \mu\text{m} \leq w_0 \leq 13.5 \text{ } \mu\text{m}$  on flat copper samples. Relative uncertainties regarding the values of material properties in the two-digit percentage range can cause high absolute uncertainties regarding the depth of up to some tens or hundreds of micrometres, especially in micromachining of deep geometries with depths of up to a few millimetres as demonstrated in [60]. The limited knowledge about the values of process parameters and material properties thus leads to a limited accuracy of prediction with analytical models and uncertainties in open-loop micromachining processes. The precise determination of the process parameters and the material properties poses an even greater challenge in industrial applications for the processing of complexly shaped components and the usage of advanced materials. Common challenges of laser micromachining in application-oriented environments with target depth are depicted in Figure 1.2.

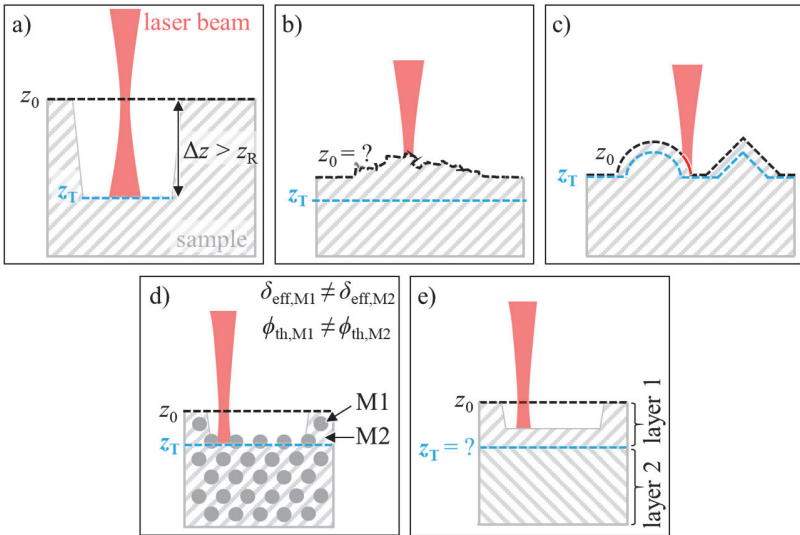


**Figure 1.2** Key challenges of laser micromachining with target depth in application-oriented environments: a) Deep geometries with  $\Delta z > z_R$ . b) An unknown surface topography  $z_0$ . c) A free-form surface and thus locally varying process parameters (e.g. fluence). d) A heterogeneous workpiece consisting of two materials (M1 and M2) with different material properties. e) An initially unknown value of the target depth  $z_T$  due to the unknown thickness of layer 1 that is to be ablated.

Challenges in terms of component geometry include machining of deep geometries with  $\Delta z > z_R$  between initial surface  $z_0$  and target depth  $z_T$  (Figure 1.2 a), an unknown surface topography and thus an unknown amount of material to be removed at a given location (Figure 1.2 b), and free-form surfaces and thus locally varying process parameters (e.g. fluence) due to different angles of inclination (Figure 1.2 c). Challenges related to the material to be machined include a heterogeneous workpiece consisting of two materials with different material properties such as effective penetration depth  $\delta_{\text{eff}}$  and ablation threshold  $\phi_{\text{th}}$  (M1 and M2 in Figure 1.2 d), and an initially unknown value of the target depth due to the unknown thickness of layer 1 that is to be removed (Figure 1.2 e).

Additional tools and techniques are required to measure and control the uncertainties resulting from the aforementioned challenges to reliably achieve the targeted depth and for parts produced “*first time right*”. The different challenges of laser micromachining in an industrial environment and the corresponding techniques for process monitoring and process control to overcome these challenges are presented in detail in the following.

### 1.3.1.1 Micromachining of deep geometries

The process parameters can change with increasing machining depth due to the beam divergence. The beam radius on the machined surface increases from  $w_0$  to  $w(z)$  (cf. Eq. (1.2)) with increasing machining depth  $z_C$  when the beam waist was set on the original surface. The increasing beam radius in turn leads to a reduced local fluence (cf. Eq. (1.4)) and thus changes the depth and width ablated by each pulse (cf. Eq. (1.8)). As a consequence, the machined depth per scan was significantly reduced for micromachining of cavities with a depth  $>200 \mu\text{m}$  in steel [63].

A constant depth progress was achieved up to over  $700 \mu\text{m}$  in the same study by shifting the position of the beam waist with increasing machining depth [63]. The position of the beam waist in relation to the surface of the sample can be determined by various methods, e.g. by measurement of the acoustic emissions [64], the plasma intensity [65] or the optical path distance [66]. The measurement of the acoustic emissions with a microphone during micromachining of ceramics allowed to detect signals of the airborne sound spectrum. The highest amplitude of the signals was measured when the beam waist was positioned on the sample surface, which allowed

determining the position of the beam waist in relation to the sample surface with an axial accuracy of  $50\ \mu\text{m}$  [64]. The plasma intensity emitted from the micromachining of aluminium was detected with a CCD camera in [65]. The highest brightness was measured when the beam waist was positioned on the surface during micromachining, which allowed to determine the position of the beam waist in relation to the surface with an axial accuracy of approximately  $50\ \mu\text{m}$ . In [66], the optical distance between the axial position of the beam waist and the surface of the sample was measured using low coherence interferometry (LCI) with a Michelson Interferometer during closed-loop micromachining of a bovine tooth. Real-time adaption of the position of the beam waist in relation to the surface of the sample allowed the machining of grooves with a constant depth and width on a bovine tooth, which had a relief amplitude over ten times the Rayleigh length  $z_R$  of the laser beam.

### 1.3.1.2 Micromachining of an unknown surface topography

During the design process of a part the targeted dimensions are specified with tolerances, due to fluctuations in material properties and uncertainties in the machining process of each processing step. The different kinds of shape deviations are categorized in six different scales according to DIN 4760 [67]. Deviations of the first order affect the characteristic dimensions of the part, such as length or height. Second-order deviations correspond to waviness with aspect ratios between the wavelength and amplitude in the range of 1000:1 to 100:1. Deviations of the third-order can be periodic or non-periodic deviations with aspect ratios between the wavelength and amplitude in the range of 100:1 to 5:1. Fourth-order deviations correspond to the surface roughness and are in the micrometre scale. The fifth-order and sixth-order deviations relate to the microstructure and crystalline structure, respectively. Only the first four orders of shape deviations (also known as surface defects) are usually relevant in industrial manufacturing processes [67]. Achieving the targeted depth at a specific location on a workpiece with unknown surface topography is challenging when open-loop laser micromachining is used since the number of pulses that needs to be applied is unknown. Furthermore, the local surface roughness of the workpiece influences the local material properties, such as the absorptance [12,68] and the ablation threshold [69], which results in an additional uncertainty with regard to the selection of the appropriate process parameters.

One approach to address these challenges is to measure the surface topography before and during micromachining in order to identify at which locations further material has to be removed and to apply locally adapted machining parameters, e.g. with regards to the number of applied pulses. Distance measurement by optical coherence tomography (OCT) is a non-destructive technique to evaluate a surface before, during and after laser micromachining. A measurement setup based on OCT was presented in [70]. The surface topography of a stepped geometry with a depth of up to 8  $\mu\text{m}$  that was produced by laser micromachining could be measured within a scanning field of 0.3 x 0.3  $\text{mm}^2$  with an axial resolution of up to 0.13  $\mu\text{m}$  and a lateral resolution of 2.5  $\mu\text{m}$  at an acquisition rate of 1.4 kHz. The measurement setup reported on in [71] is based on LCI. The surface topography of different geometries with a depth of up to 59  $\mu\text{m}$  that were produced by laser micromachining could be measured within a scanning field of 30 x 30  $\text{mm}^2$  with an axial resolution of up to 0.22  $\mu\text{m}$ . The measurement setup reported on in [66] is also based on LCI and was used to measure the surface topography of a bovine tooth with height variations exceeding 1 mm within a scanning field of up to approximately 5.5 x 1.0  $\text{mm}^2$ , with an axial resolution of 6.8  $\mu\text{m}$  and a lateral resolution of 9.4  $\mu\text{m}$  at an acquisition rate of 4 kHz.

### 1.3.1.3 Micromachining of free-form surfaces

Industrially manufactured components with function-oriented designs often have free-form surfaces. Laser micromachining of such components at normal incidence is not always possible due to the limited accessibility of the free-form surface, which is why machining of inclined surfaces may be necessary. Locally varying angles of incidence lead to locally varying process parameters [72,73]: The irradiated area increases with increasing angle of incidence, which in turn reduces the locally irradiated fluence [72]. The angle of incidence also influences the absorptivity according to the Fresnel equations [28] and the effective penetration depth [73]. These conditions make it difficult to predict suitable process parameters for achieving the desired depth at a given location on a free-form surface with open-loop micromachining.

In principle, the techniques mentioned in the previous section are also suitable for micromachining of inclined surfaces. Closed-loop depth-controlled micromachining can compensate for locally varying material removal due to locally different process parameters caused by locally different angles of incidence. The targeted depth can

therefore be achieved on inclined surfaces by measuring the local depth and applying pulses as long as the locally absorbed fluence exceeds the local ablation threshold.

### 1.3.1.4 Micromachining of heterogeneous materials

Composites such as carbon fibre-reinforced plastics (CFRP) are heterogeneous materials that are commonly used in aeronautical applications [74] or the automotive industry due to their light weight, high strength, and high stiffness [75]. CFRPs consist of two different materials, the load-bearing carbon fibres and the plastic matrix that holds the fibres in place. The unknown and locally varying distribution of the fibres and the matrix poses a challenge for the prediction of the machined depth, as both materials have strongly differing thermophysical properties: The latent heat for vaporisation of carbon fibres and plastic matrix amounts to  $79.6 \text{ J/mm}^3$  and  $1.3 \text{ J/mm}^3$ , respectively [76]. As a consequence, inhomogeneous material removal occurs even with uniform irradiation with constant parameters, which led to local deviations exceeding  $50 \text{ }\mu\text{m}$  at an average micromachining depth of  $100 \text{ }\mu\text{m}$  and to local deviations of more than  $300 \text{ }\mu\text{m}$  at an average micromachining depth of  $1 \text{ mm}$  in [77].

In-situ measurement of the machined depth during ablation of heterogeneous materials enables locally adapted processing. The approach in [78] combines a depth measurement system based on OCT with a central wavelength of  $1030 \text{ nm}$  with a nanosecond laser emitting at a wavelength of  $1060 \text{ nm}$ . Both beams were superposed using a beam splitter and were guided through a Galvanometer-scanner and an F-Theta lens. The setup allowed alternating ablation of CFRP and subsequent depth measurements to determine the areas that require further machining [78]. Inline coherent imaging was achieved in [14] with a depth measurement system operating at a wavelength of  $843 \text{ nm}$ , which was combined with a picosecond laser emitting at a wavelength of  $355 \text{ nm}$ . Closed-loop depth-controlled micromachining allowed for the fabrication of a spiral geometry with a depth of up to  $200 \text{ }\mu\text{m}$  on a heterogeneous sample consisting of latewood with a dense cell structure and earlywood with a large cell structure. The final topology showed a root-mean-square (RMS) deviation of  $35 \text{ }\mu\text{m/pixel}$  from the targeted geometry. An average ablation depth per pulse of  $9 \text{ }\mu\text{m}$  was obtained for the whole sample. The authors state that the depth obtained with open-loop micromachining would have been 56% too shallow for areas made from dense latewood and 67% too deep for areas made from earlywood, due to the

different machining rates of 4  $\mu\text{m}$  for latewood and 14  $\mu\text{m}$  for earlywood, respectively [14].

#### 1.3.1.5 Micromachining with an initially unknown value of the target depth

The layer-accurate removal of one or several layers of a multi-layer component is a challenge when there are production-related variations or tolerances in the manufacture of the layers that can lead to deviations in the thickness of the respective layers. Hence the target machining depth cannot be known in advance when the ablation is meant to stop exactly between two layers. An exemplary application is the local removal of the top layer of a solar cell or battery to reveal an underlying conducting layer as the functional path [79].

Process monitoring is required for the machining of multi-layer materials when the target depth is not known in advance, in order to detect a change of layers during ablation and thus be able to locally adjust or stop machining. Laser-induced breakdown spectroscopy (LIBS) was e.g. used for the determination of the processed material during laser micromachining in [79]. The emission from the plasma generated during laser ablation was analysed by a spectrometer in order to determine the processed material by comparing the measured spectrum with the characteristic emission lines of the respective material. The transition from carbon to copper could be detected using this approach during micromachining of a carbon-coated copper foil. LCI was used in a different approach to measure the depth progress during percussion drilling of a bimetal coin. The bimetal coin consisted of a top layer made from bronze with a thickness of 34  $\mu\text{m}$  attached to a steel substrate. The different depth progresses measured during drilling up to a depth of 35  $\mu\text{m}$  and during drilling deeper than 35  $\mu\text{m}$  allowed to detect the transition from the bronze layer to the steel substrate [66].

### 1.3.2 Research needs

The in-situ measurement of the local depth with LCI and OCT for closed-loop depth-controlled machining has proven to be a suitable technique to address and master the aforementioned challenges for the manufacture of parts produced “*first time right*”.

Two promising applications for which processes to overcome the respective challenges have not yet been developed are the automated post-processing of complexly shaped and additively manufactured metal parts and the layer-accurate removal of components made from CFRP. Both applications and the need for research in these applications are described below.

The first of the two applications is the automated post-processing of complexly shaped and additively manufactured metal parts. Additive manufacturing by laser powder bed fusion (LPBF) can be used to generate parts from slices of selectively molten powder. The process offers high flexibility for the generation of individualized and lightweight metal parts [80,81]. Post-processing is required since the LPBF process does not allow the production of parts that are directly ready to use: The parts have to be produced with support structures with a height of up to several millimetres in order to fix the produced part to the base plate and enable the generation of overhang structures [82]. The produced parts typically deviate from the targeted net shape to some extent and exhibit a high surface roughness  $R_a$  in the order of  $10\ \mu\text{m}$  to  $20\ \mu\text{m}$  due to the layer-by-layer generation [83] and partially molten powder particles adhering to the surface of the part [84]. The achievable precision is limited by the size of the powder particles, which determine the minimum thickness of the individual layers [85]. Post-processing of LPBF-generated parts by means of laser micromachining therefore addresses the challenges described in sections 1.3.1.1 to 1.3.1.3. In current work on laser-based post-processing of additively manufactured metal components, often only components with flat surfaces and simple geometries are machined and only individual defects such as surface roughness are addressed [84,86–89]. The removal of support structures is mainly done by manual and mechanical processes such as cutting, grinding or milling, which in turn limits the geometric freedom of the part [82] and can lead to damage in the case of thin-walled parts due to the mechanical stress of machining [90,91].

The development and investigation of a technique for the automatic post-processing of complexly shaped LPBF-generated components is therefore desirable. The objective of this work was to investigate and demonstrate the post-processing capabilities of depth-controlled laser micromachining monitored by OCT for LPBF-generated metal parts with regard to reducing the surface roughness and reducing deviations from the targeted net shape, milling of deep and complexly shaped geometries, and removing support structures from these parts.

The second application is the layer-accurate removal of components made from CFRP. Structural components made from CFRP can be damaged during their service lifetime and then need to be repaired [92]. The damaged areas are selectively removed in a stepped geometry to prepare for the rebuilding process with repair plies that precisely fit into the removed volume [93,94]. Each step of the stepped geometry corresponds to a layer with a specific orientation of the fibres. Layer-accurate micromachining is required to maintain the structural strength of the repaired part, as damage to an underlying layer leads to reduced adhesion of the repair plies [94]. This means that micromachining should always stop at the interface between two layers and not somewhere within one layer. Layer-accurate micromachining of CFRP is not only impeded by an inhomogeneous material removal, but also by manufacturing-related variations or tolerances in the manufacture of CFRP layers, which can lead to variations in the thickness of the respective layers of up to  $\pm 29\%$  [95]. Hence the target machining depth cannot be known in advance and when the ablation is meant to stop exactly between two layers. Layer-accurate machining of CFRP parts with thicknesses of up to several millimetres therefore addresses the challenges described in sections 1.3.1.1, 1.3.1.4 and 1.3.1.5. A process for the automated and layer-accurate machining of stepped repair geometries in CFRP by means of laser ablation has not been successfully demonstrated until the start of this thesis.

The development and investigation of a method for the in-process detection of a change of layers during laser micromachining of CFRP is therefore required. The objective of this work was to develop an image-processing-based method that uses the depth measurements generated during depth-controlled micromachining to reliably detect a change of layers with unknown layer thickness, allowing machining to be stopped at the interface of two adjacent layers for layer-accurate and stepped repair geometries.

## 1.4 Process strategies for high-throughput laser milling with high energy efficiency and high surface quality

### 1.4.1 State of research

The outstanding precision, quality, and flexibility offered by micromachining with ultrafast lasers make this technology competitive for many applications. Most often it is necessary to achieve the targeted depth in a short time and thus with high throughput to make laser micromachining economically attractive in an industrial environment. The requirements for the desired surface quality after machining must also be met in addition to the high throughput. The processed area and the local difference between the initial surface height and the target depth define the total material volume to be removed. The time required to remove the material volume in turn determines the achieved throughput.

#### 1.4.1.1 Throughput and energy-efficiency in laser milling

The volume ablated by a single pulse from a Gaussian beam with a beam radius  $w_0$  and a peak fluence  $\phi_0$  can be calculated by [96]

$$\Delta V = \frac{\pi}{4} \cdot w_0^2 \cdot \delta_{\text{eff}} \cdot \ln^2 \left( \frac{\phi_0}{\phi_{\text{th}}} \right), \quad (1.23)$$

where  $\delta_{\text{eff}}$  is the effective penetration depth and  $\phi_{\text{th}}$  the ablation threshold. The volume  $\Delta V$  ablated by a single pulse and the pulse repetition rate  $f_P$  of the laser define the material removal rate [96]

$$\dot{V} = \Delta V \cdot f_P, \quad (1.24)$$

provided that subsequent pulses are absorbed under the same conditions as their respective previous pulse. It can be seen from Eq. (1.23) and Eq. (1.24) that the material removal rate  $\dot{V}$  can be increased either by increasing the peak fluence  $\phi_0$ , which

means increasing the pulse energy  $E_p$  (cf. Eq. (1.5)) or by increasing the pulse repetition rate  $f_p$ . The maximum available average laser power

$$P = f_p \cdot E_p \quad (1.25)$$

therefore limits the material removal rate  $\dot{V}$  and thus the achievable throughput by laser micromachining, which has led to intensive efforts to optimize the energy efficiency of micromachining processes in recent years [62,96,97]. Energy efficiency in laser micromachining is often characterized by the energy-specific volume [97]

$$\Delta V_E = \frac{\dot{V}}{P} = \frac{1}{2} \cdot \frac{\delta_{\text{eff}}}{\phi_0} \cdot \ln^2 \left( \frac{\phi_0}{\phi_{\text{th}}} \right), \quad (1.26)$$

which relates the achieved material removal rate to the average laser power used for micromachining. Increasing the ablated volume by increasing the peak fluence  $\phi_0$  seems interesting due to its simplicity, but it is not optimal with respect to energy efficiency, since a pronounced maximum is found for the energy-specific volume  $\Delta V_E$ . Figure 1.3 illustrates this relation with the corresponding graphs for the ablated volume per pulse  $\Delta V$  (cf. Eq. (1.23)) and the energy-specific volume  $\Delta V_E$  (cf. Eq. (1.26)) as a function of the peak fluence  $\phi_0$  and the ratio of  $\phi_0/\phi_{\text{th}}$ . Typical parameters for micromachining of a metal substrate were taken for this example with a beam waist radius  $w_0 = 25 \mu\text{m}$ , an effective penetration depth  $\delta_{\text{eff}} = 10 \text{ nm}$ , and a threshold fluence  $\phi_{\text{th}} = 0.1 \text{ J/cm}^2$ . The ablated volume per pulse  $\Delta V$  (blue dashed line) monotonically increases with increasing peak fluence  $\phi_0$  for  $\phi_0 > \phi_{\text{th}}$ . The energy-specific volume  $\Delta V_E$  (green line) increases with increasing peak fluence  $\phi_0$  until the “optimum fluence” [97]

$$\phi_{0,\text{opt}} = e^2 \cdot \phi_{\text{th}} \quad (1.27)$$

with regard to the maximum energy-specific volume [97]

$$\Delta V_{E,\text{max}} = \frac{2}{e^2} \cdot \frac{\delta_{\text{eff}}}{\phi_{\text{th}}} \quad (1.28)$$

is reached. The energy-specific volume  $\Delta V_E$  decreases for  $\phi_0 > \phi_{0,\text{opt}}$ . It is therefore critical to choose an appropriate peak fluence for each material to achieve high energy efficiency in laser micromachining.

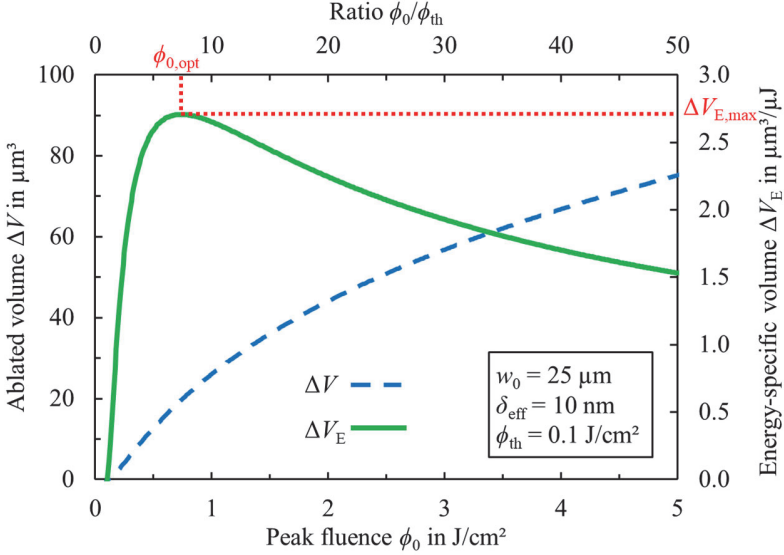


**Figure 1.3** Ablated volume  $\Delta V$  per pulse (blue dashed line) and the energy-specific volume  $\Delta V_E$  (green line) as a function of the peak fluence  $\phi_0$  and the ratio of  $\phi_0/\phi_{th}$  for the exemplary parameters  $w_0 = 25 \mu\text{m}$ ,  $\delta_{\text{eff}} = 10 \text{ nm}$ , and  $\phi_{th} = 0.1 \text{ J/cm}^2$ . The optimum fluence  $\phi_{0,\text{opt}}$  where the maximum energy-specific volume is reached and the maximum energy-specific volume  $\Delta V_{E,\text{max}}$  are indicated by red dotted lines.

#### 1.4.1.2 Surface quality in laser milling

Findings from the industrial environment show that high-quality laser milling of homogeneous materials such as silicon or metals is often associated with an average surface roughness of about  $S_a < 1 \mu\text{m}$  after machining [98,99]. One example is the fabrication of transmissive silicon optics for THz radiation, which require low roughness to achieve low scattering and thus high transmission [100]. The highest transmission of up to over 50% in the spectral range of 2.5 THz to 4.7 THz is achieved for a surface roughness  $S_a < 1 \mu\text{m}$ . The transmission is still in the double-digit percentage range with a roughness of  $1 \mu\text{m} \leq S_a \leq 3 \mu\text{m}$ , but decreases strongly at higher roughness values  $S_a > 3 \mu\text{m}$  [100]. Another example is the susceptibility of metal

surfaces to corrosion by exposition to salt fog in marine applications, where a low and moderate corrosion rate was measured for  $S_a \approx 0.1 \mu\text{m}$  and  $S_a = 1.4 \mu\text{m}$ , respectively. In contrast, a high corrosion rate was measured for the roughest surface with  $S_a = 5.8 \mu\text{m}$  [101].

The surface morphology and thus the surface roughness obtained from laser milling of silicon and metals with ultrashort laser pulses depends on the processing parameters: The peak fluence determines the resulting surface morphology, which can range from fine ripple structures with a spatial period in the scale of the laser wavelength at low peak fluences to several micrometre large cones and holes at high peak fluences [102–104]. In the case of silicon, additional defects such as nanoscale solidification cracks were observed at high peak fluences [105]. Another processing parameter that influences the surface morphology is the scanning speed. Irradiation of a spot with multiple pulses within a short time causes heat accumulation (cf. Eq. (1.12)) and can result in the formation of a bumpy surface morphology, which increases the roughness [39,106]. Multiple scans over the machined area can also result in the formation of a coarser surface morphology, which again corresponds to higher surface roughness [10,103,106].

Smooth surfaces with low surface roughness  $S_a < 1 \mu\text{m}$  and thus high quality are generally obtained by laser milling at peak fluences in the range of the optimum fluence  $\phi_{0,\text{opt}}$  and a pulse overlap of  $\Omega_x = 75\%$  [39,107,108]. Machining with the optimum fluence  $\phi_{0,\text{opt}}$  therefore leads not only to high energy efficiency but also to high surface quality.

#### 1.4.1.3 Strategies for high-throughput milling with ultrafast lasers at high average laser power

The material removal rate can be increased by increasing the repetition rate  $f_P$  while machining at the optimum fluence  $\phi_{0,\text{opt}}$  (cf. Eq. (1.24)). Excessive heat accumulation has to be avoided however to maintain high quality, as explained in the previous section. A simple technique to avoid heat accumulation defects in micromachining is to limit the number of pulses radiated to a spot and thus to limit the overlap  $\Omega_x$  by exceeding a critical speed of the beam as it moves over the surface of the sample [39]. The critical speed  $v_{\text{crit}}$  can be calculated by inserting Eq. (1.16) into Eq. (1.18) and solving for the speed, which yields

$$v_{\text{crit}} = 2 \cdot w_0 \cdot (1 - \Omega_x) \cdot f_p \cdot \quad (1.29)$$

Scanning speeds in the order of several tens or hundreds of m/s are thus required to maintain an overlap  $\Omega_x = 75\%$  for common beam diameters of a few tens of micrometres and typical repetition rates of up to tens of MHz. Galvanometer-scanners are limited to scanning speeds of a few tens of m/s [109] when used in combination with typical focal lengths in the range of several tens to several hundreds of millimetres [24]. Higher scanning speeds of up to 880 m/s can be achieved with a Polygon-scanner system [110], which is however accompanied by a reduced flexibility with regard to the scanning strategy as compared to Galvanometer-scanners.

Another approach to increase the material removal rate is to use a laser system with a fixed repetition rate  $f_p$  and to scale to higher average powers by means of increasing the pulse energy  $E_p$  (cf. Eq. (1.25)). With common focus diameters of a few tens of micrometres the peak fluence  $\phi_0$  however exceeds the optimum fluence for metals or semiconductors of  $\phi_{0,\text{opt}} \approx 1 \text{ J/cm}^2$  already at a pulse energy of a few tens of  $\mu\text{J}$ . Further strategies must therefore be pursued to maintain the optimum fluence and maximize the removal rates with high-energy lasers:

1) Temporal splitting of the pulse energy using bursts of pulses [60,108,111,112]: The laser pulse and thus the pulse energy  $E_p$  is temporally split into a number  $N_{\text{ppb}}$  of pulses with a short temporal distance in the order of one to thirty nanoseconds, whereas each pulse has an energy of  $E_p/N_{\text{ppb}}$ . The local fluence can be reduced by the divider  $N_{\text{ppb}}$  using this technique.

2) Spatial splitting of the pulse energy using beam-splitting techniques [113–115]: The laser beam and thus the pulse energy  $E_p$  are spatially split up into a number  $N_{\text{beams}}$  of beamlets arranged in an array, whereas the pulses in each beamlet have a pulse energy of  $E_p/N_{\text{beams}}$ . The arrangement and spacing between adjacent beams determine whether parallel grooves or a continuous area are machined as the beams move across the surface. The local fluence can be reduced by the divider  $N_{\text{beams}}$  using this technique.

3) Spatial distribution of the pulse energy on the surface of the sample by shifting the beam waist above or below the surface [106,116]: The pulse energy  $E_p$  is spatially distributed by exploiting the divergence of the beam to increase its radius on the

sample (cf. Eq. (1.2)). The local fluence can be reduced by the factor  $w(z)^2/w_0^2$  with this technique.

4) Spatial redistribution of the pulse energy using advanced beam shaping [44, 117–119]: The pulse energy  $E_P$  is redistributed with a beam shaping element, which allows for processing with arbitrary beam shapes and constant fluence distributions (top hat) instead of Gaussian fluence distributions.

Only the implications of strategies 1) to 3) are discussed in more detail below, since the focus of this thesis is on analytical modelling and experimental studies of the ablation with Gaussian fluence distributions. The implications of strategy 4) are not further discussed in this work and can be found in the work of *Häfner* [44].

## 1.4.2 Research needs

In the following, a simple model is denoted, which takes the implications of strategies 1) to 3) into account. The fluence

$$\phi(z) = \frac{2 \cdot E_P}{N_{\text{ppb}} \cdot N_{\text{beams}} \cdot \pi \cdot w(z)^2} \quad (1.30)$$

in the centre of a Gaussian beam can be adapted by the strategies 1) to 3), where  $z$  is the axial distance of the beam waist to the processed surface. This allows to design an energy-efficient micromachining process with a high material removal rate for a given laser system, focusing setup and material. The total material removal rate (including all temporally split pulses  $N_{\text{ppb}}$  and spatially split beamlets  $N_{\text{beams}}$ ) can be calculated by inserting Eq. (1.23) into Eq. (1.24) and multiplying by the factors  $N_{\text{ppb}}$  and  $N_{\text{beams}}$ , which yields

$$\dot{V}(z) = \frac{\pi}{4} \cdot w^2(z) \cdot \delta_{\text{eff}} \cdot f_P \cdot N_{\text{ppb}} \cdot N_{\text{beams}} \cdot \ln^2 \left( \frac{\phi(z)}{\phi_{\text{th}}} \right). \quad (1.31)$$

The impact of the strategies on the ablation diameter of each beam can be calculated based on Eq. (1.10) by

$$d_{\text{abl}}(z) = 2 \cdot w(z) \cdot \sqrt{\frac{1}{2} \cdot \ln\left(\frac{\phi(z)}{\phi_{\text{th}}}\right)}. \quad (1.32)$$

Figure 1.4 illustrates the consequences of the different strategies 1) to 3) on the material removal rate  $\dot{V}(z)$  (cf. Eq. (1.31), continuous lines) and the ablation diameter  $d_{\text{abl}}(z)$  (cf. Eq. (1.32), dashed lines). Both are shown as a function of the distance  $z$  of the beam waist to the processed surface for the typical parameters of a high-power ultrafast laser ( $P = 1$  kW) with  $\lambda_L = 1030$  nm,  $M^2 = 1.3$ ,  $f_p = 400$  kHz,  $E_p = 2.5$  mJ,  $w_0 = 25$   $\mu\text{m}$  and a material with  $\delta_{\text{eff}} = 10$  nm, and  $\phi_{\text{th}} = 0.1$  J/cm<sup>2</sup>.

Shifting the beam waist above or below the processed surface (black lines, strategy 3) to increase the beam radius  $w(z)$  and thus reduce the fluence  $\phi(z)$  requires a large shifting distance of 27.2 mm in order to reach the maximum material removal rate  $\dot{V}(z)$  and results in a large ablation diameter of  $d_{\text{abl}} = 928$   $\mu\text{m}$ . Only large geometries with a width  $>928$   $\mu\text{m}$  can therefore be micromachined using this strategy and the exemplary parameters. The usage of a pulse burst (grey lines, strategy 1,  $N_{\text{ppb}} = 5$ ) reduces the necessary shifting distance to 12.1 mm and the ablation diameter to  $d_{\text{abl}} = 415$   $\mu\text{m}$  and thus allows for micromachining of geometries with a smaller width at the maximum material removal rate  $\dot{V}(z)$ . The maximum number of pulses  $N_{\text{ppb}}$  in the burst may have to be limited due to heat accumulation (cf. Eq. (1.12)), e.g. when melt formation is to be avoided to maintain high surface quality. Additional process parallelisation by multiple beams (blue lines, strategy 2,  $N_{\text{beams}} = 5$ ) can further reduce the necessary shifting distance to 5.2 mm and can reduce the ablation diameter to  $d_{\text{abl}} = 185$   $\mu\text{m}$ . As a consequence, the given laser system, focusing setup, material, and targeted machining width define the strategy, which is best suited for micromachining with a maximized removal rate. Constant material properties are assumed in this simple model, whereas experimental studies show that the ablation threshold  $\phi_{\text{th}}$  and effective penetration depth  $\delta_{\text{eff}}$  can change with beam radius  $w(z)$  [120] and the number  $N_{\text{ppb}}$  of pulses in a burst [108]. Nevertheless, the model allows for a useful estimation of the strategies and process parameters required to achieve the maximum material removal rate for a given setup and material.

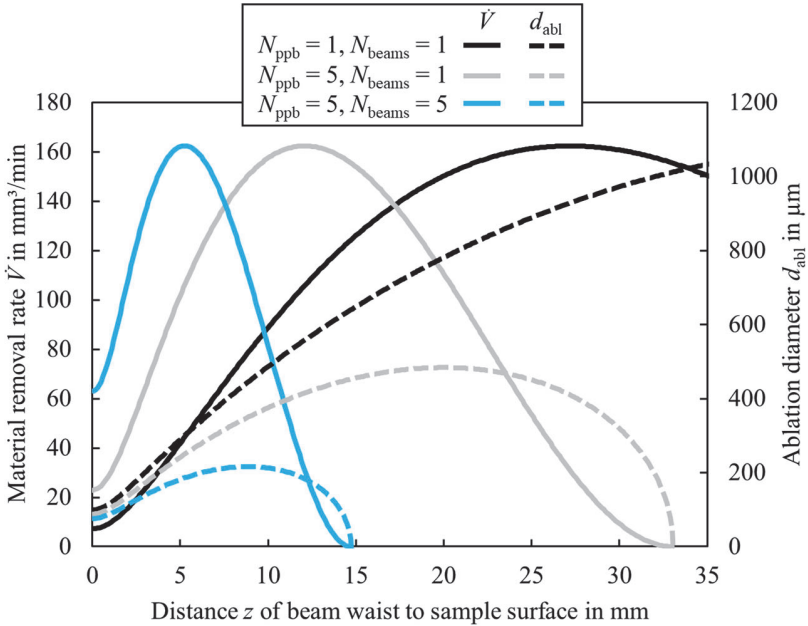


**Figure 1.4** Material removal rate  $\dot{V}$  (continuous lines) and ablation diameter  $d_{abl}$  (dashed lines) as a function of the distance  $z$  of the beam waist to the processed surface for the exemplary parameters  $\lambda_L = 1030$  nm,  $M^2 = 1.3$ ,  $f_P = 400$  kHz,  $E_P = 2.5$  mJ,  $w_0 = 25$   $\mu$ m,  $\delta_{eff} = 10$  nm, and  $\phi_{th} = 0.1$  J/cm<sup>2</sup>.

A high material removal rate is required to reach the targeted depth in a short time. In the past, the applicability of micromachining with ultrafast lasers has often been limited due to the low average laser power of only a few tens of watts. This situation has changed with recent demonstrations of ultrafast lasers with average powers in the order of kW [121–123] or multi-kW [124]. As a consequence, several new challenges have emerged in systems engineering and process design for high-quality micromachining with ultrafast lasers at high average power, such as avoidance of air breakdown and maintaining the optimum fluence despite the high pulse energy, as well as minimizing heat accumulation effects during processing at high repetition rates [17].

Figure 1.5 shows an overview of material removal rates achieved in the past few years by micromachining of cavities with ultrafast lasers at different laser powers

and for different materials such as metals, metal alloys and silicon. The different symbols represent different materials and the different colours represent different surface qualities quantified by the surface roughness  $S_a$ . The different categories of surface roughness were chosen following the applications mentioned in the previous section: Green symbols represent a very high surface quality and  $S_a < 1 \mu\text{m}$ , yellow symbols represent good surface quality with  $1 \mu\text{m} < S_a < 3 \mu\text{m}$  and red symbols represent low quality with  $S_a > 3 \mu\text{m}$ . White symbols refer to data points where no roughness value was available in the corresponding reference. The values with the highest material removal rate, the material removal rate at the highest energy-specific volume and the material removal rate at the lowest roughness were taken when multiple values for material removal rates were available in a reference.

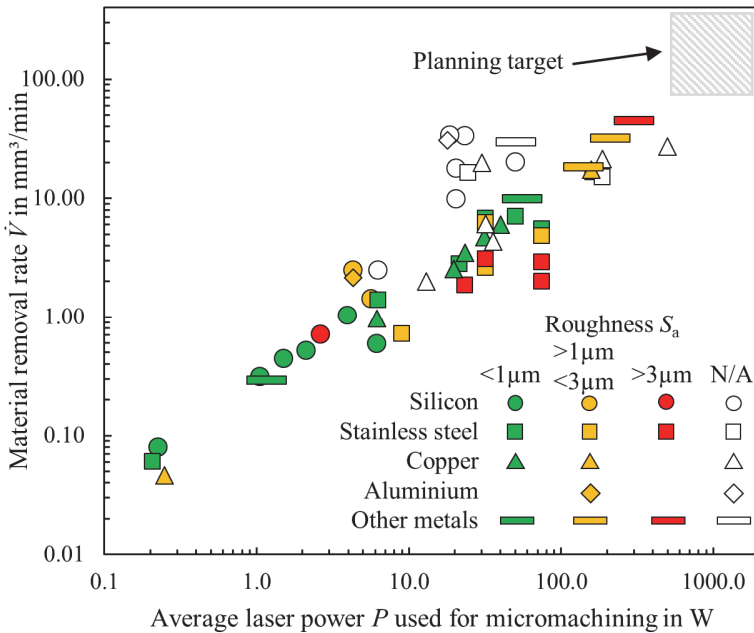


**Figure 1.5** Overview of the state of the art (in June 2022) of realized material removal rates  $\dot{V}$  as a function of the average laser power  $P$  in micromachining of cavities with ultra-short laser pulses [60,108,110–112,114,116,125–134]. The symbols represent different materials; the colours represent different surface qualities. No roughness data were available for white symbols.

High-quality surfaces with  $S_a < 1 \mu\text{m}$  obtained from micromachining of cavities in silicon with ultrafast lasers were demonstrated for average laser powers of up to  $P = 6.2 \text{ W}$  [131] and with material removal rates up to  $\dot{V} \approx 1 \text{ mm}^3/\text{min}$  [111]. Average laser powers of up to  $P = 162 \text{ W}$  were used to obtain material removal rates up to  $\dot{V} = 16.5 \text{ mm}^3/\text{min}$  for micromachining of cavities in metals with a roughness  $S_a < 1 \mu\text{m}$  [129]. The highest average power used for micromachining of metals was  $P = 500 \text{ W}$  and resulted in a material removal rate of  $\dot{V} = 27 \text{ mm}^3/\text{min}$ , however, without further characterization of the surface roughness [114]. Micromachining of cavities in silicon or metals with an average laser power over 1 kW has not been demonstrated prior to this thesis, although ultrafast lasers with average powers in the range of kW have been available for a few years.

The development of process strategies for machining with ultrafast lasers in the kW-class is desirable in order to open up further potential fields of application for laser micromachining in the industrial environment, where the available throughput has so far prevented the use of this technology [135–140]. The objective of this work was to develop and demonstrate a micromachining process for high-quality surfaces on silicon and metals using an ultrafast laser with an average power of over 1 kW to achieve material removal rates in the range of  $100 \text{ mm}^3/\text{min}$ , as indicated by the grey hatched area in Figure 1.5.

## 1.5 Summary of research needs

The research needs for laser micromachining with target depth can be summarized as follows:

1. Development of analytical models for the calculation of the depth progress when machining geometries with high aspect ratios (depth/width) using ultrashort laser pulses. These models would allow to design the process parameters prior to the laser machining process and extend the available analytical models for the calculation of the depth progress of holes and grooves from previously only shallow geometries and constant deepening rate to deep geometries and decreasing or ceasing deepening rate.
2. Investigation of depth-controlled laser milling for two demanding applications:

- I. A method for automated post-processing of complexly shaped LPBF-generated components by depth-controlled laser milling needs to be developed in order to avoid manual and mechanical processes.
  - II. A method for the in-process detection of a change of layers during laser milling of CFRP is required in order to enable layer-accurate machining of stepped repair geometries.
3. Scaling the throughput of high-quality laser milling of silicon and metals using an ultrafast laser with an average power exceeding 1 kW to achieve record-breaking material removal rates in the order of 100 mm<sup>3</sup>/min. The demonstration of high-quality processing while maintaining high throughput at this elevated power level potentially opens up further fields of application for laser micromachining in the industrial environment, where the available throughput has so far prevented the use of this technology.

The aforementioned research needs are addressed in the following chapters of this thesis. Chapter 2 presents two developed and experimentally verified analytical models to calculate the depth progress of percussion-drilled holes and engraved grooves in metals. Chapter 3 presents and describes technical solutions to the challenges of two demanding applications, such as post-processing of LPBF-generated metal components and layer-accurate ablation of CFRP. Chapter 4 describes the processing strategy used to demonstrate high-quality, high-throughput laser milling of silicon and metals to a depth of up to several hundred micrometres using a 1 kW sub-picosecond laser.

## **2 Development and verification of analytical models for the depth progress during micromachining of geometries with high aspect ratios**

Section 1.2.2 described the need for research to develop analytical models to predict the depth progress in micromachining of geometries with high aspect ratio using ultrashort laser pulses. The following section 2.1 describes a developed and experimentally verified analytical model for the calculation of the depth progress of percussion-drilled holes in metals. Section 2.2 describes a developed and experimentally verified analytical model for the calculation of the depth progress of engraved grooves in metals.

### **2.1 Analytical model for the depth progress of percussion drilling with ultrashort laser pulses**

This section contains a reproduction of the published article [141]. This article is subject to the "CC BY 4.0 Creative Commons" license (<http://creativecommons.org/licenses/by/4.0/>). Changes to text, symbols, equations, figures and numbering of references have been made solely for unification and consistency in this thesis. No changes have been made to the content.

Journal: Applied Physics A: Materials Science & Processing

Date of publication: 02.04.2021

DOI: <https://doi.org/10.1007/s00339-021-04455-3>

Copyright: © The Author(s) 2021

Daniel Holder<sup>1</sup>, Rudolf Weber<sup>1</sup>, Thomas Graf<sup>1</sup>, Volkher Onuseit<sup>1</sup>, David Brinkmeier<sup>1,2</sup>, Daniel J. Förster<sup>1,3</sup>, and Anne Feuer<sup>1</sup>

<sup>1</sup>*Institut für Strahlwerkzeuge (IFSW), University of Stuttgart, Pfaffenwaldring 43, 70569 Stuttgart, Germany*

<sup>2</sup>*Graduate School of Excellence advanced Manufacturing Engineering (GSaME), Nobelstraße 12, 70569 Stuttgart, Germany*

<sup>3</sup>*LightPulse Laser Precision, Pfaffenwaldring 43, 70569 Stuttgart, Germany*

## **Abstract**

A simplified analytical model is presented that predicts the depth progress during and the final hole depth obtained by laser percussion drilling in metals with ultrashort laser pulses. The model is based on the assumption that drilled microholes exhibit a conical shape and that the absorbed fluence linearly increases with the depth of the hole. The depth progress is calculated recursively based on the depth changes induced by the successive pulses. The experimental validation confirms the model and its assumptions for percussion drilling in stainless steel with picosecond pulses and different pulse energies.

## **1 Introduction**

For the manufacturing of parts such as dry metal forming tools with lubricant holes [142] and spinneret nozzles for direct spinning of microfibers, efficient drilling of several hundred of high-quality microholes is required in hardened deep drawing tools [143] and spinnerets [8], respectively. Helical drilling with ultrashort laser pulses is often used for a defined shaping of high-quality microholes [144–146]. However, this approach requires special cost-intensive optics. In contrast, percussion drilling can be performed with a simple setup and allows for efficient and productive drilling of microholes with a high drilling rate and short breakthrough times, which is important when several hundreds of microholes need to be drilled into one work-

piece. Short drilling times in metals can be achieved by percussion drilling at repetition rates in the range of hundreds of kHz or MHz [48,147,148]. However, the drilling rate at high repetition rates is increased by excessive melt formation [34,147,149] due to heat accumulation effects [38,150]. Melt formation significantly reduces the hole quality e.g. with the formation of rims at the hole inlet [48,147,149] and recast layers within the hole [48]. Quality reducing effects can also occur at lower repetition rates when high fluences are used. In this case, the occurrence of a particle-ignited plasma causes a widening of the hole entrance [151,152] and bulge formation within the hole [49]. The excessive generation of melt and the formation of particle-ignited plasma during laser drilling must be avoided for demanding applications such as the manufacturing of the mentioned lubricant holes in dry metal forming tools in order to achieve high-quality microholes and maintain the specific properties of the hardened deep drawing tool.

Conical hole geometries are formed during percussion drilling with ultrashort laser pulses [43,47–50] as long as the thermal defects are avoided. Following *Döring et al.*, the evolution of the hole's depth during percussion drilling can be divided into three distinct phases:

In phase 1, the drilling process is mainly characterized by a high drilling rate and results in a reproducible hole geometry. The drilling process in phase 2 is dominated by an irregular drilling progress with gradually decreasing drilling rate and decreasing reproducibility of the hole geometries. Finally, in phase 3, the drilling process is defined by stagnation with a ceasing drilling progress [45]. Hence, each phase exhibits different drilling rates and hole qualities, as described in [45] for drilling in silicon. The three phases may be interpreted as a superposition of a regular drilling process, that dominates in phase 1 and that continues in phase 2 and 3 but with a decreasing depth growth with increasing number of pulses, and irregular drilling contributions that start to become noticeable and later dominate the further depth growth as from phase 2. Hence the evolution of the drilling depth may be described as a sum of the drilling depth achieved with the regular process and the additional depth generated by the irregular, i.e. unpredictable, contributions. Both contributions come to a stop in phase 3. Drilling of reproducible and conically shaped microholes can be achieved when the drilling process is stopped before the end of phase 1, where the drilling is still dominated by the regular process without noticeable influence of the irregular contributions, which led to the definition of a “quality depth limit”

[45,49]. An analytical model for the estimation of the quality depth limit of percussion drilling with picosecond laser pulses is presented in [49]. Drilling deeper than the quality depth limit is not efficient due to the gradually decreasing drilling rate and stagnation in phase 2 and phase 3, respectively [45]. In addition, the depths obtained in the phases 2 and 3 are increasingly affected by the irregular drilling contributions. Therefore, it is essential to know the drilling rate at any time during the percussion drilling process when efficient drilling of reproducible and conically shaped microholes is required. Optical coherence tomography was demonstrated to be a versatile tool for online monitoring of the ablated depth [153,154] or drilling rate during drilling with short and ultrashort laser pulses [13]. Appropriate processing of the OCT signals allowed for the determination of the hole depth with an accuracy of  $\pm 30 \mu\text{m}$  during percussion drilling of stainless steel with nanosecond laser pulses [155].

An analytical model for the prediction of the regular drilling progress during laser percussion drilling through all the 3 abovementioned phases is introduced in the following. The model was experimentally verified using a calibrated OCT-based depth measurement for the case of drilling of blind holes with a depth of up to 1.5 mm in stainless steel with different pulse energies.

## **2 Depth progress and hole geometry of percussion-drilled microholes**

The model presented in section 3 is motivated by the experimentally observed depth progress and the resulting geometry of microholes that were percussion-drilled in stainless steel plates using picosecond laser pulses. The experiments presented in the following were performed in ambient atmosphere using the setup shown in Figure 2.1. The processed material was cold-rolled stainless steel of the type AISI 304. The processing laser with a wavelength of  $\lambda_L = 1030 \text{ nm}$  and a pulse duration of 8 ps was operated at a low repetition rate of 21.4 kHz and the laser beam was circularly polarized. Optical measurements of the depth of the holes were performed with a Fourier-domain OCT-based system (*CHRcodile 2, Precitec*), which provides a measurement rate of 70 kHz, an axial measurement range of approximately 6 mm and an axial measurement accuracy of down to  $\pm 1 \mu\text{m}$ . The processing laser beam and the OCT probe beam were coaxially superposed by means of a dichroic mirror (*Layertec*), which was HR-coated for the beam of the processing laser at a wavelength of  $\lambda_L = 1030 \text{ nm}$  and AR-coated for the OCT beam centred at a wavelength of

$\lambda_o = 1080$  nm. The beams were guided through a Galvanometer-scanner for deflection and focused by an F-Theta lens with a focal length of  $f = 340$  mm, resulting in focal radii of  $w_0 = 61 \pm 5$   $\mu\text{m}$  for the processing laser and of  $15 \pm 5$   $\mu\text{m}$  for the OCT probe beam.

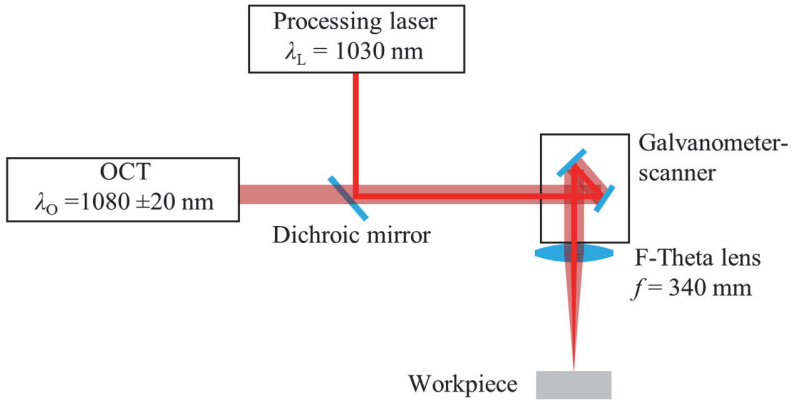


**Figure 2.1** Experimental setup for the OCT-based measurement of the depth of the holes during laser percussion drilling.

The OCT-based depth measurements were recorded during the experiments and analysed after applying two numerical signal-processing filters. First, a signal-to-noise ratio (SNR) filter was applied in order to remove noise. Second, an “increasing depth”-filter was applied to the SNR-filtered values. This filter is based on the assumption that the hole depth can only increase and not decrease by drilling with ultrashort laser pulses and low repetition rates as shown in [13]. Hence, only the depth values for which the newly measured depth is larger than the previously determined depth are considered. Application of both filters and linear interpolation between the depth values yields the evolution of the drilling depth as a function of the number of incident pulses.

Figure 2.2 shows a filtered OCT-based depth measurement of the percussion drilling progress as a function of the number of pulses (red line) for a pulse energy of  $E_P = 143$   $\mu\text{J}$ . Six holes were drilled using the same energy  $E_P = 143$   $\mu\text{J}$  but with different total numbers of pulses for the verification of the OCT-based depth measure-

ments by means of cross-sections of the holes. The micrographs of these cross-sections of holes produced by the application of 10,000 (inset no. 1), 20,000 (inset no. 2), 50,000 (inset no. 3), and 75,000 (inset no. 4) pulses are shown in Figure 2.2 with the corresponding depth values marked as blue squares. The light blue scale bar represents a length of 200  $\mu\text{m}$ .

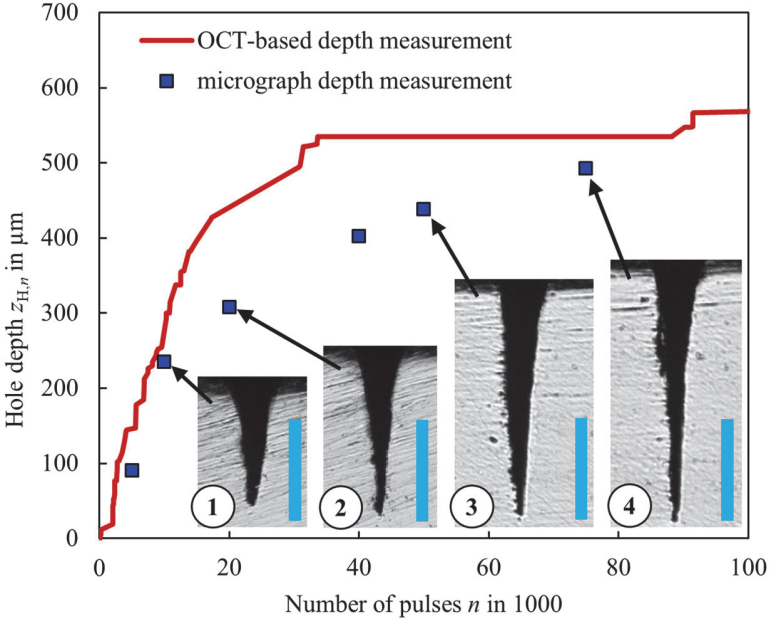


**Figure 2.2** Hole depth  $z_{H,n}$  as a function of the number of applied pulses  $n$  as measured by OCT (red curve) and as measured from micrographs of cross sections (blue quadratic data points). The percussion drilling was performed with a pulse energy of  $E_p = 143 \mu\text{J}$  and a focal radius of  $w_0 = 61 \mu\text{m}$ . Corresponding cross sections of some of the holes drilled with 10,000 (1), 20,000 (2), 50,000 (3), and 75,000 (4) pulses are shown as insets. The light blue scale bars with the insets represent a length of 200  $\mu\text{m}$ .

The hole depth measured by OCT increased with a high drilling rate during the first approximately 34,000 pulses until a hole depth of about 530  $\mu\text{m}$  was reached, corresponding to phase 1 of the drilling process. For higher numbers of pulses, the growth of the depth achieved by the regular drilling process slows down and finally saturates and the further growth of the hole is characterized by the irregular contributions in

phase 2 and 3. A similar behaviour was found for drilling of silicon [45]. The deviations between the depths measured by OCT and the depths obtained from the cross-sections shown in the micrographs might result from inaccuracies of the OCT-based depth measurement [155] or more probably to the inaccuracy of the grinding /polishing process used for the creation of the cross-sections. As the centre of the hole is not easily hit during grinding and polishing, the depth determined from these cross sections systematically yield a value that is too small. Nevertheless, the cross-sections provide important information about the shape of the hole. For percussion drilling of stainless steel with picosecond pulses with a pulse energy of  $E_p = 143 \mu\text{J}$ , a focal radius of  $w_0 = 61 \mu\text{m}$ , and up to a total of 75,000 pulses (inset no. 4), the conical hole shape clearly dominates the geometry of the drilled holes, indicating a drilling process within the “quality depth limit” [49].

### 3 Analytical model of the depth progress during percussion drilling of conically shaped microholes

Based on these findings, an analytical, recursive model was derived for the calculation of the depth progress that is achieved by the regular drilling process. The recursive model is based on the assumption that the hole depth  $z_{H,n}$  after  $n$  pulses can be calculated by

$$z_{H,n} = z_{H,n-1} + z_{abl,n}, \quad (2.1)$$

where  $z_{H,n-1}$  denotes the hole depth after  $n-1$  pulses,  $z_{abl,n}$  denotes the depth ablated by the  $n^{\text{th}}$  pulse, and  $n \in 1, 2 \dots N$ . For the shape of the hole, the simple geometrical approximation of a cone is assumed, as illustrated in Figure 2.3. This corresponds to the experimental results shown in Figure 2.2, where the geometry of a high-quality hole is typically of conical shape. The radius  $r_H$  of the hole’s opening drilled with a Gaussian beam is determined by the ablation threshold fluence  $\phi_{A,\text{th}}$  and is given by [30,49]

$$r_H = w_0 \cdot \sqrt{\frac{1}{2} \cdot \ln \left( \frac{\phi_{A,0}}{\phi_{A,\text{th}}} \right)}, \quad (2.2)$$

where  $\phi_{A,0}$  denotes the absorbed peak fluence on the flat workpiece at the centre of the Gaussian beam at normal incidence and  $w_0$  is the radius of the beam on the surface of the workpiece.

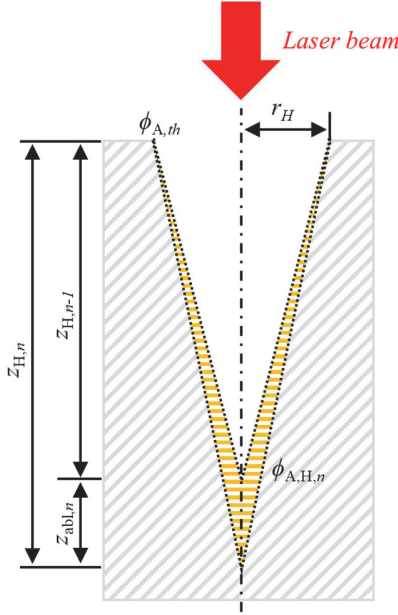


**Figure 2.3** Cross section of a cone-shaped hole with an entrance radius  $r_H$  and a depth of  $z_{H,n}$  after the application of the  $n^{\text{th}}$  pulse. The absorbed fluence of the  $n^{\text{th}}$  pulse in the hole is assumed to linearly increase from  $\phi_{A,th}$  at the entrance to  $\phi_{A,H,n}$  at the tip of the hole. The corresponding ablation leads to a hole depth which is increased by the amount  $z_{abl,n}$  from  $z_{H,n-1}$  to  $z_{H,n}$ .

The absorbed peak fluence is given by

$$\phi_{A,0} = \frac{A \cdot 2 \cdot E_p}{\pi \cdot w_0^2}, \quad (2.3)$$

where  $A$  is the material-specific absorptivity at normal incidence of a beam on a flat surface. The absorbed ablation threshold fluence  $\phi_{A,th}$  can be calculated by

$$\phi_{A,th} = \delta_{eff} \cdot h_V, \quad (2.4)$$

where  $\delta_{eff}$  is the effective penetration depth of the laser beam and  $h_V$  is the volume-specific enthalpy required for complete vaporization of the material. The effective penetration depth  $\delta_{eff}$  describes the energy transport into the material and is dominated by either the optical penetration depth or electron heat diffusion length depending on the peak fluence [26]. The ablation threshold fluence decreases with increasing number of pulses, also known as incubation effect. The threshold fluence depends on the material-specific incubation coefficient and is lowered by a factor of three to four from single pulses to several hundred pulses. As a result, the lowered ablation threshold causes an increased hole radius according to Eq. (2.2). For more than  $10^3$  pulses, a saturation of the incubation effect occurs and the ablation threshold fluence is not decreased by further number of pulses [34]. For the sake of simplicity, the absorbed ablation threshold fluence  $\phi_{A,th}$  is assumed to be constant over the entire drilling process in our model. When considering a drilling process of several tens of thousands pulses as shown in Figure 2.2, the error caused by this simplification is negligible.

As explained in Figure 2.3, the application of the  $n^{\text{th}}$  pulse in the conically shaped hole leads to the ablation of the yellow (horizontally) hatched material. By this, the hole depth is increased by the amount  $z_{abl,n}$  from  $z_{H,n-1}$  to  $z_{H,n}$ . For the calculation of the depth increment  $z_{abl,n}$  achieved by the  $n^{\text{th}}$  pulse only the absorbed fluence  $\phi_{A,H,n}$  reaching the tip of the conical hole is considered. The absorbed energy in the material volume exponentially drops with the distance to the sample surface, resulting in the logarithmic ablation law given by [97]

$$z_{abl,n} = \delta_{eff} \cdot \ln \left( \frac{\phi_{A,H,n}}{\phi_{A,th}} \right). \quad (2.5)$$

Eq. (2.5) holds for ablation of metals with laser pulses in the picosecond range when electron heat conduction is neglected [156]. Due to multiple reflections and diffuse scattering within the hole, the absorbed fluence at the tip  $\phi_{A,H,n}$  cannot easily be determined, but raytracing simulations showed an elevated absorbed fluence near the tip of the hole [157]. Note that  $\phi_{A,H,n}$  is the fluence at the tip of the hole resulting

from the  $n$ th pulse in the geometry of the hole as given after  $n-1$  pulses, which has a depth of  $z_{H,n-1}$ . As the most simple approximation for an elevated absorbed fluence near the tip of the hole, a linear increase of the absorbed fluence

$$\phi_A(z) = \phi_{A,\text{th}} + \left( \phi_{A,H,\text{th}} - \phi_{A,\text{th}} \right) \cdot \frac{z}{z_{H,n-1}} \quad (2.6)$$

along the depth  $z$  of the conically shaped hole is assumed, starting with the ablation threshold fluence  $\phi_{A,\text{th}}$  at the hole's opening and ending with the fluence  $\phi_{A,H,n}$  at the hole's tip. This assumption is consistent with the fact, that the regular drilling process gradually slows down with increasing depth, reaching a final limit when the absorbed fluence is reduced to the threshold value everywhere on the hole's wall as already presented in [49]. The superimposed increase of the hole's depth beyond the contribution of the regular process (as noticeable in phase 2 and 3) may be attributed to local irregularities in the hole's geometry generating more or less random hot spots of the incident radiation by multiple reflections in the hole [46]. At this state of the process the ablation only occurs at the location of these hot spots and not on the whole surface of the hole as caused by the regular process, leading to an irregular and less reproducible drilling process during phase 2 and 3. The irregular contributions to the depth growth are not considered by the present model.

As the integral of the absorbed fluence on the surface of the hole equals the total energy  $\eta_{A,H,n-1} \cdot E_P$  absorbed in the hole,

$$\int_0^{z_{H,n-1}} \frac{2 \cdot \pi \cdot \sqrt{r_H^2 \cdot z_{H,n-1}^2}}{z_{H,n-1}} \cdot r(z) \cdot \phi_A(z) dz = \eta_{A,H,n-1} \cdot E_P \quad (2.7)$$

where

$$r(z) = r_H - r_H \cdot \frac{z}{z_{H,n-1}} \quad (2.8)$$

$\phi_{A,H,n}$  is found to be

$$\phi_{A,H,n} = \frac{3 \cdot \eta_{A,H,n-1} \cdot E_P}{\pi \cdot r_H \cdot \sqrt{r_H^2 + z_{H,n-1}^2}} - 2 \cdot \phi_{A,th}, \quad (2.9)$$

where  $\eta_{A,H,n-1}$  represents the overall absorptance of the  $n^{\text{th}}$  pulse in the hole geometry that is present after the  $(n-1)^{\text{th}}$  pulse. The overall absorptance  $\eta_{A,H,n-1}$  is calculated based on the model originally introduced by *Gouffé* [158,159] with the corrections by *Hügel* and *Graf* [160] and is found to be

$$\eta_{A,H,n-1} = A \cdot \frac{1 + (1 - A) \left( \sigma_{n-1} - \frac{\alpha_{n-1}}{2\pi} \right)}{A \cdot (1 - \sigma_{n-1}) + \sigma_{n-1}} \quad (2.10)$$

where  $\sigma_{n-1}$  is the ratio of the area of the opening of the hole to the complete surface area of the hole including the opening, and  $\alpha_{n-1}$  is the solid angle under which the opening is seen from the tip of the hole. For a conical hole geometry  $\sigma_{n-1}$  is given by

$$\sigma_{n-1} = \frac{1}{1 + \sqrt{1 + \frac{z_{H,n-1}^2}{r_H^2}}} \quad (2.11)$$

and the solid angle  $\alpha_{n-1}$  is given by

$$\alpha_{n-1} = 4 \cdot \pi \cdot \sin^2 \left( \frac{1}{2} \arctan \left( \frac{r_H}{z_{H,n-1}} \right) \right). \quad (2.12)$$

It is noted that the model presented here requires only two generally known laser parameters,  $E_P$  and  $w_0$ , and three material parameters,  $A$ ,  $\delta_{\text{eff}}$  and  $h_V$ , which were determined for different metals in [161] and [162].

#### 4 Experimental verification

The model for the prediction of the depth progress during percussion drilling derived in section 3 was compared to experimental results obtained by drilling in stainless steel with the setup outlined in section 2. The hole radius and drilling progress were calculated from the given laser parameters, i.e. for a beam radius of  $w_0 = 61 \mu\text{m}$ , and for three different pulse energies ranging from  $143 \mu\text{J}$  to  $412 \mu\text{J}$ , which corresponds to irradiated peak fluences ranging from  $2.4 \text{ J/cm}^2$  to  $7.0 \text{ J/cm}^2$ . The values published in [162] and [163] for iron were used to calculate  $h_v = 61 \text{ J/mm}^3$  and are summarized in Table 2.1. The absorptivity was taken as  $A = 0.38$  [161]. The penetration depth  $\delta_{\text{eff}}$  was used as a fit parameter. The best agreement for the whole drilling process was achieved with  $\delta_{\text{eff}} = 20 \text{ nm}$  and yields an absorbed threshold fluence of  $\phi_{A,\text{th}} = 0.12 \text{ J/cm}^2$  (see Eq. (2.4)). The fitted value of the penetration depth  $\delta_{\text{eff}} = 20 \text{ nm}$  was assumed to be constant and is consistent with published values of the optical penetration depth of  $21 \text{ nm}$  for iron in [161] and  $20 \text{ nm}$  for stainless steel in [26].

Material parameter	Value
Density	$7,870 \frac{\text{kg}}{\text{m}^3}$ [162]
Heat capacity for solid iron	$449 \frac{\text{J}}{\text{kg} \cdot \text{K}}$ [162]
Melting temperature	$1,811 \text{ K}$ [162]
Latent heat of melting	$247 \frac{\text{kJ}}{\text{kg}}$ [162]
Evaporation temperature	$3,134 \text{ K}$ [162]
Latent heat of vaporization	$6,260 \frac{\text{kJ}}{\text{kg}}$ [163]

**Table 2.1** Material parameters for iron published in [162] and [163] used for calculating the volume-specific enthalpy required for complete vaporization of the material  $h_v$ .

The calculated hole radius according to Eq. (2.2) for the different pulse energies yields  $61 \mu\text{m}$  for  $143 \mu\text{J}$ ,  $69 \mu\text{m}$  for  $243 \mu\text{J}$  and  $76 \mu\text{m}$  for  $412 \mu\text{J}$ , respectively. The calculated hole radii were verified using the microscope images of drilled holes with

a number of pulses  $>10^3$  to neglect the increasing hole radius due to the lowered ablation threshold caused by the incubation effect within the first few hundreds of pulses, which is not taken into account by our model. The calculated hole radii are in good agreement with the measured hole radii of  $63\pm 4\ \mu\text{m}$  for  $143\ \mu\text{J}$ ,  $71\pm 4\ \mu\text{m}$  for  $243\ \mu\text{J}$  and  $73\pm 3\ \mu\text{m}$  for  $412\ \mu\text{J}$ .

The hole depth as a function of the number of pulses for the different pulse is shown in Figure 2.4. The solid lines correspond to the OCT-measurements, and the dotted lines to the values calculated with the analytical model presented in section 3.

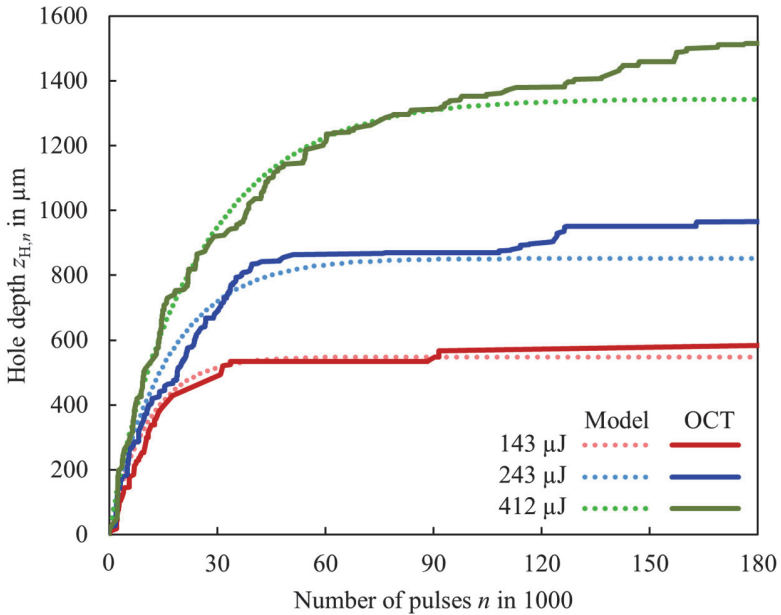


**Figure 2.4** Hole depth as a function of the number of pulses for different pulse energies as measured by OCT (solid lines) and as predicted by the model derived in section 3 (dotted lines). Parameters:  $w_0 = 61\ \mu\text{m}$ ,  $A = 0.38$ ,  $\delta_{\text{eff}} = 20\ \text{nm}$ ,  $h_V = 61\ \text{J}/\text{mm}^3$  ( $\phi_{A,\text{th}} = 0.12\ \text{J}/\text{cm}^2$ ).

The depth progress decreases with increasing number of pulses and stagnates when the fluence in the tip  $\phi_{A,H,T,n}$  converges the ablation threshold  $\phi_{A,\text{th}}$  (cf. Eq. (2.5)). It can be seen that both the depth progress and the maximum drilling depth increase with increasing pulse energy. Drilling with the highest investigated pulse energy

$E_p = 412 \mu\text{J}$  yields a maximum hole depth of  $>1.5$  mm. The measured depth and model predictions are in excellent agreement for the examined pulse energies. The model only describes the drilling progress achieved by the contribution of the regular drilling process. The calculated curves and assumptions made therefore coincide very well with the experimental result during the first phase, where the irregular contributions are still negligible. The minor deviations between the curves at low numbers of pulses might result from the inaccuracy of the depth measurement [155] or uncertainties regarding the material parameters used for the calculation, in particular the value for  $\delta_{\text{eff}}$  which might differ in the beginning of the drilling process when the fluence is still far above the ablation threshold. Furthermore, an increased absorptivity was measured for surfaces covered with surface structures which occur after a few hundred pulses [164,165] and which were also found on the bottom of drilled holes [166]. This might lead to a faster than calculated drilling progress during the beginning of the drilling process. The deviation between the experimental and the theoretically predicted hole depth after a large number of pulses which is especially observed for high pulse energies is attributed to the additional contribution by the irregular drilling process as from phase 2, which is presumably induced by local geometrical irregularities, which are not considered by the model. Also not considered in the model are other physical phenomena that can influence the drilling rate in ambient atmosphere, such as a saturated ablation plume [167] and material redeposition [168]. Laser radiation of subsequent pulses is absorbed in the ablation plume if the temporal distance of the irradiating pulses is smaller than the time required for dissipation of the plume. In our experiments with the pulse repetition rate of 21.4 kHz the effect of the ablation plume is negligible as the propagation velocity of the ablation plume is typically in the range of several hundreds of meters per second [169,170]. Material redeposition on the walls of the hole can influence the drilling rate [168] and hole geometry [171]. Geometrical deviations from the conical shape can also be caused by reflections from the walls of the hole resulting in a channel formation at the opening of the hole [172]. However, the conical hole shape clearly dominates the geometry of the drilled holes as shown by the cross-sections in Figure 2.2.

Hence, the investigations show that the presented model with the assumed conical hole geometry is suitable for the correct calculation of the hole radius and hole depth as achieved by the regular drilling process which dominates the first phase of percussion drilling. Knowing the absorptivity  $A$ , the effective penetration depth  $\delta_{\text{eff}}$  and

the evaporation enthalpy  $h_V$  (or hence,  $\phi_{A,th} = 0.12 \text{ J/cm}^2$ ), the pulse energy  $E_P$  and the beam radius  $w_0$ , the model allows for the prediction of the depth of reproducible conical holes as a function of the applied number of pulses.

## 5 Conclusion

An analytical model for the prediction of the depth progress and hole depth of conically shaped holes which are percussion drilled in metals with ultrashort laser pulses was derived. The model predicts the progress of the drilling depth for percussion-drilled holes in stainless steel with picosecond pulses up to the quality depth limit. The corresponding assumptions for the model were experimentally validated for different laser parameters using OCT-based depth measurements and cross sections of the drilled holes.

## Acknowledgements

The authors thank Dr. Markus Kogel-Hollacher and *Precitec* for providing the OCT-based measurement system *CHRcodile 2*. Furthermore, the authors thank Liane Hoster for preparing the cross-sections for the optical analysis and Dr. Lucy Blaney-Laible for proof-reading the manuscript.

## 2.2 Analytical model for the depth progress during laser micromachining of V-shaped grooves

This section contains a reproduction of the published article [173]. This article is subject to the "CC BY 4.0 Creative Commons" license (<http://creativecommons.org/licenses/by/4.0/>). Changes to text, symbols, equations, figures and numbering of references have been made solely for unification and consistency in this thesis. No changes have been made to the content.

Journal: Micromachines

Date of publication: 31.05.2022

DOI: <https://doi.org/10.3390/mi13060870>

Daniel Holder<sup>1</sup>, Rudolf Weber<sup>1</sup>, and Thomas Graf<sup>1</sup>

<sup>1</sup>*Institut für Strahlwerkzeuge (IFSW), University of Stuttgart, Pfaffenwaldring 43, 70569 Stuttgart, Germany*

## Abstract

An analytical model is presented that allows predicting the progress and the final depth obtained by laser micromachining of grooves in metals with ultrashort laser pulses. The model assumes that micromachined grooves feature a V-shaped geometry and that the fluence absorbed along the walls is distributed with a linear increase from the edge to the tip of the groove. The depth progress of the processed groove is recursively calculated based on the depth increments induced by successive scans of the laser beam along the groove. The experimental validation confirms the model and its assumptions for micromachining of grooves in a Ti-alloy with femtosecond pulses and different pulse energies, repetition rates, scanning speeds and number of scans.

## 1 Introduction

Laser micromachining of grooves with ultrashort laser pulses is a versatile process that can be applied for various applications, such as cutting through thin metal foils [174], dicing silicon wafers [54], engraving implants made of titanium alloy to enhance osseointegration [175] or engraving cutting tools to reduce the force and friction in mechanical machining of aluminium [9]. In micromachining processes with pulsed lasers, a relative movement between the laser beam and the workpiece is created either by deflecting the laser beam over the processed surface by means of a scanner or by moving the workpiece past the static beam by means of a linear axis.

In both cases, multiple scans over the same contour are typically performed to fabricate grooves with a required depth. The dimensions of the micromachined grooves, i.e., the depth and width or their aspect ratio (depth/width), have a major influence on the performance of the respective application: A complete cut through the sample is required in the cutting of thin metal sheets [174]. In open microfluidic systems, a higher flow velocity of liquids is achieved for grooves with a higher aspect ratio [176,177]. Grooves with higher aspect ratios also enhanced the performance of engraved cutting tools in mechanical machining [9].

The laser micromachined grooves with depths of a few tens up to several hundreds of micrometres typically feature a V-shaped geometry in metals [55,58], semiconductors [53,54], dielectrics [178] and polymers [179]. The resulting width of the grooves mainly depends on the diameter of the laser beam, the incident peak fluence and the material-specific ablation threshold [52]. Experimental results revealed the influence of various processing parameters on the resulting depth of a micromachined groove, such as the pulse energy or the irradiated peak fluence, the scanning speed, the number of scans over the surface [53–55] and the ablation threshold [52]. The groove's depth can be increased by multiple scans, whereas high pulse energies [54,55] and low scanning speeds [53] result in a higher increase in the depth for each scan. The progress of the depth of micromachined grooves exhibited a linear correlation with the number of scans for cutting through thin metal foils with a thickness of up to 50  $\mu\text{m}$  [174] and for micromachining of shallow grooves with a depth of up to a few tens of micrometres in semiconductors [53]. A constant deepening rate of laser-processed grooves was achieved up to an aspect ratio (depth/width) of approximately 1.5 [177], which corresponds to the phase of constant depth progress observed in areal micromachining of metals [59] and silicon [180], where the aspect ratio is typically  $<1$ . The depth progress gradually slows down with increasing depth of the groove [53,55,177], reaching a limit when the absorbed fluence is reduced to the value of the ablation threshold everywhere on the walls of the groove [54]. This behaviour corresponds to the one found for percussion drilling of microholes, where a decreasing rate of the depth progress was observed with the increasing number of applied pulses, which finally stagnated at the maximum reachable depth [45,141]. It is not energy-efficient to process until this maximum depth is reached since the rate of the depth progress decreases despite the constant applied average power.

The in situ measurement of the current depth during processing has already been demonstrated using optical coherence tomography for percussion drilling of microholes [13,141] and for areal micromachining [153,154]. This approach is also suitable for the production of grooves, as shown in [177] for groove depths up to 500  $\mu\text{m}$ . The prediction of the reachable depth of the grooves or the estimate of the rate of the depth progress during laser micromachining, which would allow for the design of an efficient and productive machining process, has proven to be difficult due to the influence and interplay of various laser parameters, scanning parameters and material properties, including the groove's depth itself. A numerical model for the calculation of the groove geometry is proposed in [181], but the model does not consider the increased absorptance in V-shaped grooves that is caused by multiple reflections, which were observed in raytracing simulations [61].

A simplified analytical model for the prediction of the depth progress in laser machining of V-shaped grooves with ultrashort laser pulses is therefore introduced in the following section. The model was experimentally verified for the case of laser micromachining of grooves with a depth of up to  $624_{-38}^{+28}$   $\mu\text{m}$  in the Ti-alloy Ti6Al4V with different pulse energies, repetition rates, scanning speeds and number of scans.

## **2 Analytical model for the prediction of the depth and width of laser micromachined grooves**

An analytical, recursive model for the calculation of the depth progress of laser-processed V-shaped grooves in metals can be derived in analogy to the model for percussion drilling of conical microholes as presented in [141]. Figure 2.5 illustrates the assumptions made for the model as seen by the cross section in the  $y$ - $z$ -plane perpendicular to the scanning direction  $x$ .

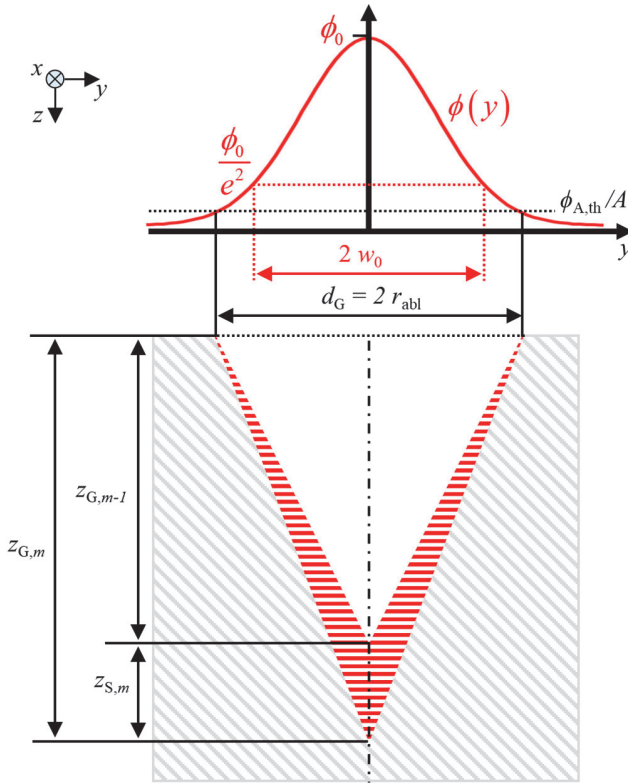


**Figure 2.5** V-shaped groove produced by a pulsed laser beam which is scanned along the x-axis. The Gaussian distribution of the fluence of the individual laser pulses is shown by the red curve. The width of the groove is denoted by  $d_G = 2 r_{abl}$ , which corresponds to two times the ablation radius  $r_{abl}$ . The incrementally increased depth of the groove is denoted by  $z_{G,m}$ , where  $m$  is the number of applied scans and  $z_{S,m} = z_{G,m} - z_{G,m-1}$  is the incremental increase in the depth produced by the  $m$ th scan along the groove. The cross section of the volume ablated during the  $m$ th scan is highlighted by the red hatched cross section.

The pulses of a Gaussian laser beam are irradiated onto the metal sample (the grey hatched cross section) at normal incidence (i.e., in the z-direction). At the surface of the workpiece, the transversal distribution of the incident fluence (red curve) is given by

$$\phi(x, y) = \phi_0 \cdot \exp\left(-2 \frac{(x - x_c)^2 + (y - y_c)^2}{w_0^2}\right) \quad (2.13)$$

where  $x - x_c$  and  $y - y_c$  are the distances from the centre of the laser beam located at  $(x_c, y_c)$ ,  $w_0$  is the beam radius and  $\phi_0$  denotes the peak fluence, which is given by

$$\phi_0 = \frac{2 \cdot E_P}{\pi \cdot w_0^2}, \quad (2.14)$$

where  $E_P$  is the pulse energy. At normal incidence, material removal by ablation on the surface occurs when the locally absorbed fluence  $A \cdot \phi(y)$ , where  $A$  is the material-specific absorptivity at the wavelength of the incident radiation, exceeds the value

$$\phi_{A,th} = \delta_{eff} \cdot h_V \quad (2.15)$$

of the ablation threshold, where  $\delta_{eff}$  denotes the effective penetration depth of the absorbed energy density and  $h_V$  denotes the volume-specific enthalpy required for heating and complete vaporization of the material. The effective penetration depth  $\delta_{eff}$  is dominated either by the optical penetration depth or by the electron heat diffusion length, depending on the peak fluence of the incident radiation [26]. Additionally,  $\delta_{eff}$  and thus  $\phi_{A,th}$  decrease with increasing number of pulses applied to the surface [36] due to the so-called incubation effect [33]. The incubation effect saturates after about 100 pulses, whereupon the effective penetration depth and the ablation threshold are not significantly decreased further by additional pulses [36]. For the sake of simplicity, the energy penetration depth  $\delta_{eff}$  and thus the ablation threshold  $\phi_{A,th}$  are assumed to be constant over the entire process for the presented analytical model. The error caused by this simplification during the first 100 pulses is negligible as typically, more than several thousands of pulses are applied to each location for the production of laser machined grooves.

The width of the groove  $d_G$  resulting from material removal corresponds to two times the ablation radius  $r_{abl}$  and is calculated by [141]

$$d_G = 2 \cdot r_{abl} = 2 \cdot w_0 \cdot \sqrt{\frac{1}{2} \cdot \ln \left( \frac{A \cdot \phi_0}{\phi_{A,th}} \right)} \quad (2.16)$$

since no ablation can occur at the locations  $|y| > r_{abl}$  where the fluence absorbed on the surface of the workpiece is lower than the ablation threshold. It is implicitly premised here that the spatial overlap of consecutive pulses along the scan path in the  $x$ -direction is sufficiently large to ensure a constant width of the groove. The spatial pulse overlap  $\Omega_x$  is defined by

$$\Omega_x = 1 - \frac{p_x}{2 \cdot w_0} \quad (2.17)$$

where

$$p_x = \frac{v_x}{f_p} \quad (2.18)$$

denotes the spatial offset between the impact locations of two consecutive pulses,  $v_x$  is the scanning speed and  $f_p$  is the pulse repetition rate. A constant groove width  $d_G$  is typically achieved with a spatial pulse overlap ranging from 30% to 95% [54].

The proposed recursive model is based on the assumption that the groove depth  $z_{G,m}$  after  $m \in 1, 2 \dots M$  scans can be calculated by

$$z_{G,m} = z_{G,m-1} + z_{S,m} \quad (2.19)$$

where  $z_{G,m-1}$  denotes the groove depth after  $m-1$  scans and  $z_{S,m}$  denotes the depth ablated by the  $m$ th scan (cf. Figure 2.5). The overall absorptance  $\eta_{A,G}$  resulting from multiple reflections inside the V-shaped groove may be calculated assuming specular reflections of a ray, which is incident in  $z$ -direction and is found to be [160]

$$\eta_{A,G}(d_G, z_{G,m-1}) = 1 - (1 - A)^{N_R(d_G, z_{G,m-1})} \quad (2.20)$$

where  $N_R$  denotes the number of reflections of the ray until it leaves the groove again. This number of reflections depends on the aspect ratio of the V-shaped groove and is given by [160]

$$N_R(d_G, z_{G,m-1}) = \left\lceil \frac{\pi}{2 \cdot \arctan\left(\frac{d_G}{2 \cdot z_{G,m-1}}\right)} - \frac{1}{2} \right\rceil, \quad (2.21)$$

where  $\lceil \cdot \rceil$  is the rounding up function.

The energy  $dE_{A,m}(x_j)$  absorbed from one single pulse of a Gaussian laser beam during the  $m$ th scan along the groove at the location  $x$  in a stripe with the width  $dx$  inside the groove between the edges at  $y = \pm d_G/2$  amounts to

$$dE_{A,m,j}(x) = dx \cdot \int_{-d_G/2}^{d_G/2} \eta_{A,G}(d_G, z_{G,m-1}) \cdot \phi_0 \cdot \exp\left(-2 \frac{(x - x_{c,j})^2 + y^2}{w_0^2}\right) dy \quad (2.22)$$

where  $x_{c,j} = j \cdot dx$  is the location of the beam axis along the  $x$ -axis at the time at which the  $j$ th pulse hits the workpiece and where  $j \in \mathbb{Z}$  and  $y_c$  was set to zero for the beam, which is centred on the groove.

The overall absorptance  $\eta_{A,G}(d_G, z_{G,m-1})$  only defines the amount of energy  $dE_{A,m,j}(x)$  absorbed in the groove but does not specify the transversal distribution of the fluence in the  $y$ - $z$ -plane (cf. Figure 2.5). As shown by raytracing simulations of V-shaped capillaries in [61], the effect of multiple reflections causes an elevated absorbed fluence near the tip of the groove. As a simple approximation for the transversal distribution of the absorbed fluence in the groove, it is assumed in the following that the absorbed fluence linearly increases with the depth along the sidewalls of the V-shaped groove in the  $y$ - $z$ -plane. In analogy to the model presented for percussion drilling [141] and assuming that multiple reflections only occur normal to the axis of the groove, the distribution of the absorbed fluence at a given location  $x$  along the groove is assumed to start with  $\phi_{A,th}$  at the edge of the groove (at  $y = \pm d_G/2$ ) and end with  $\phi_{A,G,m,j}(x)$  at the tip of the groove ( $y = y_c = 0$ ). With this assumption, the energy

$dE_{A,m,j}(x)$  absorbed at the location  $x$  from a single pulse  $j$  in a stripe of width  $dx$  amounts to

$$dE_{A,m,j}(x) = dx \cdot \sqrt{d_G^2 + 4 \cdot z_{G,m-1}^2} \cdot \left( \frac{\phi_{A,th} + \phi_{A,G,m,j}(x)}{2} \right) \quad (2.23)$$

where  $\sqrt{d_G^2 + 4 \cdot z_{G,m-1}^2}$  is the length of the two sidewalls together measured in the  $y$ - $z$ -plane (cf. Figure 2.5). As both Eq. (2.22) and Eq. (2.23) describe the same energy, it follows that

$$\begin{aligned} dx \cdot \sqrt{d_G^2 + 4 \cdot z_{G,m-1}^2} \cdot \left( \frac{\phi_{A,th} + \phi_{A,G,m,j}(x)}{2} \right) &= dx \cdot \eta_{A,G}(d_G, z_{G,m-1}) \cdot \phi_0 \\ &\cdot \exp\left( \frac{-2 \cdot (x - x_{c,j})^2}{w_0^2} \right) \cdot \int_{-d_G/2}^{d_G/2} \exp\left( \frac{-2 \cdot y^2}{w_0^2} \right) dy. \end{aligned}$$

Inserting Eq. (2.14) and replacing the integral with  $\sqrt{\frac{\pi}{2}} \cdot w_0 \cdot \operatorname{erf}\left(\frac{d_G}{\sqrt{2} \cdot w_0}\right)$ , where  $\operatorname{erf}$  is the well-known error function, one finds that the fluence deposited at the tip of the groove with the depth  $z_{G,m-1}$  at the location  $x$  by the  $j$ th pulse during the  $m$ th scan is given by

$$\begin{aligned} \phi_{A,G,m,j}(x) &= \frac{2 \cdot \sqrt{2} \cdot \eta_{A,G}(d_G, z_{G,m-1}) \cdot E_P}{\sqrt{\pi} \cdot w_0 \cdot \sqrt{d_G^2 + 4 \cdot z_{G,m-1}^2}} \cdot \operatorname{erf}\left(\frac{d_G}{\sqrt{2} \cdot w_0}\right) \\ &\cdot \exp\left( \frac{-2 \cdot (x - x_{c,j})^2}{w_0^2} \right) - \phi_{A,th}. \end{aligned} \quad (2.24)$$

Figure 2.6 shows a sequence of distributions of the fluence  $\phi_{A,G,m,j}(x)$  with a spatial offset of  $p_x$  each absorbed at the tip of the groove around an arbitrary point  $x_0$ . For

the sake of clarity, the figure is divided into two parts showing the pulses with  $j \leq 0$  in Figure 2.6 a) and the pulses with  $j \geq 0$  in Figure 2.6 b). The pulses are numbered in such a way that the beam axis coincides with  $x_0$  at the moment when the 0th pulse hits the workpiece ( $x_{c,0} = x_0$ ). Considering this diagram, it becomes evident that from the perspective of a point ( $x = x_0, y = 0$ ) located at  $x_0$  somewhere along the centre line of the groove, the individual pulses of a scan can only contribute to the ablation of the groove at this point  $x_0$  as long as the fluence absorbed at the tip  $\phi_{A,G,m,j}(x_0) > \phi_{A,th}$  exceeds the ablation threshold  $\phi_{th}$ . The fluence that is absorbed at the tip of the groove from each of the pulses  $j$  of one scan (with  $j = \dots, -3, -2, -1, 0, 1, 2, 3, \dots$ ) at the location  $x = x_0$  is given by the intersection of the fluence distribution  $\phi_{A,G,m,j}(x)$  with the ordinate at  $x = x_0$ , as indicated by the coloured small arrows in Figure 2.6.

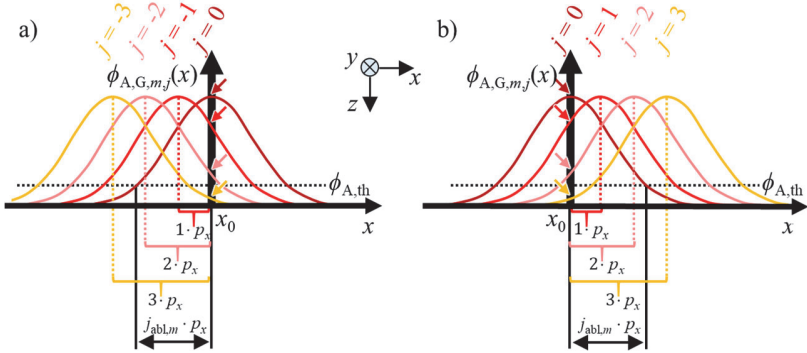


**Figure 2.6** Absorbed fluence distributions  $\phi_{A,G,m,j}(x)$  along the  $x$  axis at  $y = 0$  of the incident pulses a) from  $j = -3$  to  $j = 0$  and b) from  $j = 0$  to  $j = 3$ . The coloured small arrows indicate the absorbed fluence at the location  $x_0$ . The intersection of the fluence distributions  $\phi_{A,G,m,j}(x)$  with the ablation threshold  $\phi_{A,th}$  determines the maximum number of pulses  $j_{abl,m}$  contributing to ablation in this direction along the  $x$  axis.

In the example depicted in Figure 2.6, only the pulses from  $j = -2$  to  $j = 2$  contribute to material ablation at ( $x = x_0, y = 0$ ), as only their fluences  $\phi_{A,G,m,j}(x_0)$  exceed the ablation threshold  $\phi_{th}$ , whose value is indicated by the black dotted line. The intersection  $\phi_{A,G,m,j}(x) = j_{abl,m} \cdot p_x = \phi_{A,th}$  of the fluence distribution  $\phi_{A,G,m,j}(x)$  with the ablation threshold  $\phi_{A,th}$  determines the maximum number of pulses  $j_{abl,m}$  contributing to ablation in this direction. Using Eq. (2.24) and solving for  $j_{abl,m}$  yields

$$j_{abl,m} = \frac{w_0}{p_x} \cdot \sqrt{\frac{1}{2} \cdot \ln \left( \frac{\sqrt{2} \cdot \eta_{A,G}(d_G, z_{G,m-1}) \cdot E_p \cdot \operatorname{erf} \left( \frac{d_G}{\sqrt{2} \cdot w_0} \right)}{\phi_{A,th} \cdot \sqrt{\pi} \cdot w_0 \cdot \sqrt{d_G^2 + 4 \cdot z_{G,m-1}^2}} \right)}. \quad (2.25)$$

As a result, the depth ablated by the  $m$ th scan  $z_{S,m}$  as seen by the spot  $x = x_0$  located on the centre line of the groove corresponds to the accumulated depth ablated by the pulses  $j = -\lfloor j_{abl,m} \rfloor$  to  $j = \lfloor j_{abl,m} \rfloor$  and can be calculated by

$$z_{S,m} = \sum_{j=-\lfloor j_{abl,m} \rfloor}^{\lfloor j_{abl,m} \rfloor} z_{abl,m,j}(x) \quad (2.26)$$

where  $\lfloor \cdot \rfloor$  means rounding off and  $z_{abl,m,j}(x)$  denotes the depth ablated by the pulse  $j$  during the  $m$ th scan. According to the logarithmic ablation law [25,36], the depth increment ablated by a single pulse is given by

$$z_{abl,m,j}(x) = \delta_{\text{eff}} \cdot \ln \left( \frac{\phi_{A,G,m,j}(x)}{\phi_{A,th}} \right). \quad (2.27)$$

In the present model, a constant absorptance  $\eta_{A,G}(d_G, z_{G,m-1})$  as given by Eq. (2.20) and Eq. (2.21) is assumed during one scan over the groove. This induces a negligible error since  $\eta_{A,G}$  changes very slowly with an increasing number  $m$  of scans as long as  $z_{S,m} \ll d_G$ , which is typically the case in micromachining processes with a reasonable pulse overlap  $\Omega_x$  in the range of 30–95%.

With the above equations, the progress of the increasing groove depth  $z_{G,m}$  can be recursively calculated as a function of the number  $m$  of scans. A useful way to proceed is by starting with the calculation of the constant parameters that are not affected by the recursive calculation, such as the spatial offset  $p_x$  between the impact locations of two consecutive pulses using Eq. (2.18). Furthermore, the peak fluence  $\phi_0$  and

ablation threshold  $\phi_{A,th}$  can be calculated with Eq. (2.14) and Eq. (2.15), respectively, in order to determine the width of the groove  $d_G$  using Eq. (2.16). With the first scan ( $m = 1$ ) at the beginning of the recursive calculation, a very small value should be chosen for the initial groove depth, e.g.,  $z_{G,0} = 1 \text{ nm}$  ( $z_{G,0} \neq 0$ ), so as not to divide by 0 in the subsequent calculation of the absorptance  $\eta_{A,G}(d_G, z_{G,0})$  in Eq. (2.20) and Eq. (2.21). Then, the maximum number of pulses  $j_{abl,1}$  contributing to ablation in each direction is calculated using Eq. (2.25), followed by the calculation of the fluence  $\phi_{A,G,1,j}(x)$  deposited at the tip of the groove with Eq. (2.24) for each contributing pulse  $j$  during this first scan. The depth increment  $z_{abl,1,j}(x)$  ablated by each pulse  $j$  is calculated using Eq. (2.27) and accumulated according to Eq. (2.26). Then, the accumulated depth of the first scan  $z_{S,1}$  is added to the initial groove depth  $z_{G,0}$  as given by Eq. (2.19). The calculation of the absorptance  $\eta_{A,G}(d_G, z_{G,1})$  of the groove with increased depth  $z_{G,1}$  starts the second loop of the recursive calculation. This procedure must be repeated  $m$  times to receive the groove depth  $z_{G,m}$  after micromachining with  $m$  scans.

The absorbed fluence  $\phi_{A,G,m,j}(x)$  at the tip of the groove decreases with increasing groove depth due to the increasing length of the sidewalls  $\sqrt{d_G^2 + 4 \cdot z_{G,m-1}^2}$ . This reduction is partially compensated by an increased absorptance  $\eta_{A,G}(d_G, z_{G,m-1})$  due to the increasing number  $N_R$  of reflections within the groove (cf Eq. (2.20) and Eq. (2.21)). The maximum attainable groove depth  $z_{G,max}$  obtained after  $m \rightarrow \infty$  scans is reached when the fluence  $\phi_{A,G,m,j}(x = x_c)$  at the tip of the V-shaped groove converges to the value of the ablation threshold  $\phi_{th}$ . The maximum groove depth  $z_{G,max}$  can therefore be found with Eq. (2.24) by setting  $\phi_{A,G,m,j}(x = x_c) = \phi_{th}$ , and solving for  $z_{G,max}$ , which yields

$$z_{G,max} = \sqrt{\frac{\eta_{A,G,\infty} \cdot E_P^2}{2 \cdot \pi \cdot W_0^2 \cdot \phi_{A,th}^2} \cdot \left( \operatorname{erf} \left( \frac{d_G}{\sqrt{2} \cdot W_0} \right) \right)^2 - \frac{d_G^2}{4}} \quad (2.28)$$

where  $\eta_{A,G,\infty} = \eta_{A,G}(d_G, z_{G,\infty-1})$  denotes the absorptance of a groove micromachined with  $\infty-1$  scans. As the absorptance, in turn, depends on the groove depth  $z_{G,m-1}$  (cf. Eq. (2.20) and Eq. (2.21)), the maximum groove depth  $z_{G,max}$  cannot be calculated directly but has to be found by a recursive calculation using Eq. (2.19). Assuming a

high aspect ratio  $z_{G,\max}/d_G$  of the final groove, the absorptance can, however, be approximated to be  $\eta_{A,G,\infty} = 1$ , and the maximum achievable groove depth  $z_{G,\max}$  obtained with a given parameter set can directly be estimated using Eq. (2.28) by setting  $\eta_{A,G,\infty} = 1$ . Eq. (2.28) also shows that the maximum achievable groove depth does neither depend on the repetition rate  $f_P$  nor on the scanning parameters such as the scanning speed  $v_x$  and that - for a given beam radius  $w_0$  and with the material-specific value of  $\phi_{A,\text{th}}$  - it can only be increased by increasing the pulse energy  $E_P$ . It is noted that the model for the calculation of the depth progress presented in this section only requires five generally known laser and scanning parameters, namely the pulse energy  $E_P$ , the repetition rate  $f_P$ , the radius  $w_0$  of the laser beam, the scanning speed  $v_x$ , and the number of scans  $m$ , as well as the three material parameters, absorptivity  $A$ , energy penetration depth  $\delta_{\text{eff}}$ , and the enthalpy  $h_V$  for heating and complete vaporization of the material.

### 3 Experimental verification of the analytical model

The model for the prediction of the depth and width of laser micromachined grooves derived in the previous section was compared to experimental results obtained by micromachining samples with a size of 50 x 50 mm<sup>2</sup> and a thickness of 1 mm made of Ti6Al4V (ASTM Grade 5), a Ti-alloy often used in the aerospace industry and for biomechanical applications due to the high specific strength, corrosion resistance and biocompatibility. The ultrafast laser system *Pharos* from *Light Conversion* with a wavelength of 1030 nm was used for micromachining. The laser emitted pulses with a pulse duration of 260 fs. The circularly polarized laser beam with a Gaussian intensity distribution had a beam propagation factor of  $M^2 < 1.3$ . The beam was scanned over the surface of the samples by means of a Galvanometer scanner (*Scanlab, intelliSCAN 30*) and was focused by an F-Theta lens (*Sill Optics, S4LFT1330/328*) with a focal length of 340 mm, resulting in a focal radius of  $w_0 = 55 \pm 5 \mu\text{m}$ . The focus position was always set on the surface of the samples. Grooves with a length of 10 mm to 35 mm were micromachined in the Ti-samples with different pulse energies  $E_P$ , repetition rates  $f_P$ , scanning speeds  $v_x$  and number of scans  $m$ , as summarized in Table 2.2. The spatial offset  $p_x$  of the impact locations of two consecutive pulses and the corresponding pulse overlap  $\Omega_x$  were calculated according to Eq. (2.18) and Eq. (2.17), respectively.

	$P$ in W	$E_P$ in $\mu\text{J}$	$\phi_0$ in $\text{J}/\text{cm}^2$	$f_P$ in kHz	$v_x$ in m/s	$p_x$ in $\mu\text{m}$	$\Omega_x$	Number of scans $m$
P1	9.05	181	3.81	50	1.2	24	78%	300...10000
P2	3.45	69	1.45	50	1.2	24	78%	300...10000
P3	6.90	69	1.45	100	2.4	24	78%	600...20000
P4	3.45	69	1.45	50	2.4	48	56%	600...20000
P5	3.45	69	1.45	50	0.6	12	89%	150...5000

**Table 2.2** Sets of parameters as used for micromachining of grooves with different depths and widths.

After micromachining, the samples were cut perpendicular to the grooves ( $y$ - $z$ -plane), and cross sections were prepared by grinding and polishing in order to investigate the shape of the grooves and measure their depth and width using an optical microscope (*Leica, DM6 M*). Figure 2.7 shows the cross sections obtained with the parameter set P1 (cf. Table 2.2).

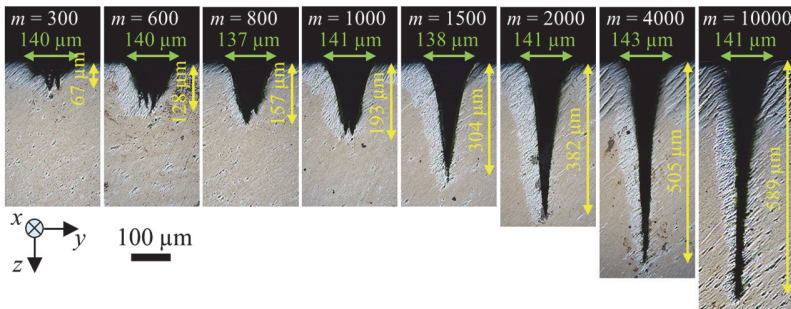


**Figure 2.7** Cross sections of grooves micromachined in Ti6Al4V with the parameter set P1. The depth and width of each groove are indicated by a yellow double arrow and a green double arrow, respectively.

Five grooves were machined with each of the parameter sets listed in Table 2.2. The measured values of the depth and width of the five grooves from each parameter set were used for averaging and calculating the maximum and minimum deviation. As expected from theory, the width of the groove remained constant at the value of  $d_G = 138_{-5}^{+8} \mu\text{m}$  independent of the number of scans, which is also in good agreement with the results shown in [54]. The V-shape clearly dominates the shape of the shown grooves for  $m \geq 800$ . Deviations from the V-shape can be seen for  $m = 300$  and  $m = 600$  due to rough structures at the bottom of the grooves. Bending of the tip of

the groove occurred for  $m = 10000$ , which was also observed in [55] for micromachining of deep grooves in a Ni-alloy and drilling of deep microholes in CVD diamond [182]. The cause for the bending of the tip has not been conclusively clarified yet, but a polarization-dependent behaviour was found in [182].

The material parameters for titanium published in [162,183] were used for the calculation of the volume-specific enthalpy of  $h_v = 47.1 \text{ J/mm}^3$ , which is required to heat and vaporize the material. The values are listed in Table 2.3. The absorptivity of titanium at normal incidence and at a wavelength of 1030 nm was set to  $A = 0.51$  [184]. The effective penetration depth was used as a fit parameter. A good agreement between the calculated and the experimental results was found with  $\delta_{\text{eff}} = 30 \text{ nm}$ . This value corresponds to an absorbed threshold fluence of  $\phi_{A,\text{th}} = 0.14 \text{ J/cm}^2$  (cf. Eq. (2.15)). The fitted value of  $\delta_{\text{eff}} = 30 \text{ nm}$  is consistent with experimentally determined values of the optical penetration depth of 26 nm for Ti6Al4V [185] and 30 nm for titanium [26].

Material parameter	Value
Density	$4506 \frac{\text{kg}}{\text{m}^3}$ [162]
Heat capacity for solid titanium	$523 \frac{\text{J}}{\text{kg} \cdot \text{K}}$ [162]
Melting temperature	$1668^\circ\text{C}$ [162]
Latent heat of melting	$440 \frac{\text{kJ}}{\text{kg}}$ [183]
Vaporisation temperature	$3287^\circ\text{C}$ [162]
Latent heat of vaporisation	$8305 \frac{\text{kJ}}{\text{kg}}$ [183]

**Table 2.3** Material properties of titanium, as published in [162,183] used for the calculation of the volume-specific enthalpy  $h_v$  for heating and vaporization.

The groove widths are given by Eq. (2.16) for the peak fluences of  $3.81 \text{ J/cm}^2$  (P1) and  $1.45 \text{ J/cm}^2$  (P2) and yield  $d_G = 126 \mu\text{m}$  and  $d_G = 100 \mu\text{m}$ , respectively. The experimentally determined widths of  $138_{-5}^{+8} \mu\text{m}$  (P1) and  $113_{-3}^{+4} \mu\text{m}$  (P2) are slightly

larger. The moderate deviations of less than 15% may be explained by the fact that no incubation effect is taken into account in the model.

The progress of the groove depth  $z_{G,m}$  as a function of the number  $m$  of scans was recursively calculated as described above. The calculations are compared to the experimental results in Figure 2.8. The groove depths as calculated by the model derived in the previous section and as measured from the cross sections for the different parameter combinations P1–P5 (cf. Table 2.2) are represented in different colours with dotted lines and data points, respectively. The value of the data points corresponds to the average values measured from up to five grooves micromachined with identical parameters. The error bars represent the deviation to the maximum and minimum measured groove depth of each parameter set.

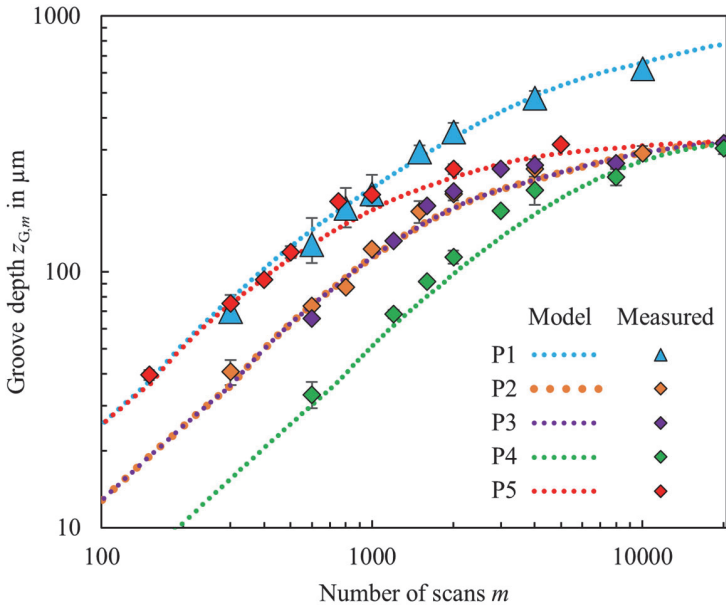


**Figure 2.8** Calculated groove depth (dotted lines, “Model”) and measured groove depth (data points, “Measured”) as a function of the number of scans for grooves micromachined in Ti6Al4V using the different parameter sets as given in Table 2.2.

Up to an aspect ratio (depth/width) of  $z_G/d_G \approx 1.5$ , the measured groove depth increases almost linearly with the number of scans. The progress of the depth is found

to slow down for aspect ratios beyond  $z_G/d_G > 1.5$ . At constant repetition rate  $f_P$  and scanning speed  $v_x$ , higher depth progress and deeper grooves were achieved for higher pulse energies (cf. P1 and P2). For constant pulse energy  $E_P$  and constant pulse overlap  $\Omega_x$ , the groove depth as a function of number of scans is similar (cf. P2 and P3). However, the net processing time is divided in half for P3 in comparison to P2 due to double the scanning speed  $v_x$  at a twofold repetition rate  $f_P$ . At constant pulse energy  $E_P$  and constant repetition rate  $f_P$ , higher depth progress is achieved with lower scanning speeds  $v_x$  (cf. P3, P4 and P5). The relations observed in this work regarding the depth progress in micromachining of grooves in Ti6Al4V confirm the observations made for semiconductors in [53,54] and for a Ni-alloy in [55]: The groove depth increases with increasing number of scans, and at high pulse energies and low scanning speeds, a greater increase in depth was observed with each scan. The maximum groove depth of  $624_{-38}^{+28}$   $\mu\text{m}$  was achieved with the highest investigated pulse energy  $E_P = 181$   $\mu\text{J}$  and the highest number of scans  $m = 10000$  for this parameter combination (P1). The maximum measured groove depth for a constant pulse energy  $E_P = 69$   $\mu\text{J}$  and different scanning parameters (from P2 to P5) is in the range of  $306_{-14}^{+13}$   $\mu\text{m}$ .

The groove depths as calculated by the model (dotted lines, “Model”) and as measured by the cross sections with the optical microscope (data points, “Measured”) are in very good agreement for the different parameter combinations and for the different number of scans. The depth progress predicted by the model decreases with increasing number of scans and stagnates when the fluence in the tip converges the ablation threshold, which corresponds well with the results from [54]. As a result, the calculated groove depths as a function of the number of scans for a constant pulse energy  $E_P = 69$   $\mu\text{J}$ , but micromachined with different scanning parameters (from P2 to P5) converge to the same maximum groove depth, which agrees well with the theoretical prediction of the model of  $326$   $\mu\text{m}$  calculated by Eq. (2.28) for  $\eta_{A,G,\infty} = 1$ . Deviations from calculation and measurement might result from uncertainties regarding the material parameters used for the calculation, in particular the fitted value for the effective penetration depth  $\delta_{\text{eff}}$ , or from deviations of the assumed ideal V-shape, as shown before in Figure 2.7 for  $m = 10000$ , with the bending of the tip. Complete vaporization is assumed in the proposed analytical model, whereas additional effects such as melting and spallation can cause a deviating process enthalpy and thus a different ablation rate [27].

Nevertheless, for a broad range of laser and scanning parameters, the V-shape and calculated groove dimensions by the model correspond to the shape and groove dimensions as measured by the cross sections shown in Figure 2.9 for some of the grooves from P1 to P5 and different number of scans. The coloured triangles were dimensioned according to the groove depth  $z_G$  and groove width  $d_G$ , as calculated by the model derived in the previous section.

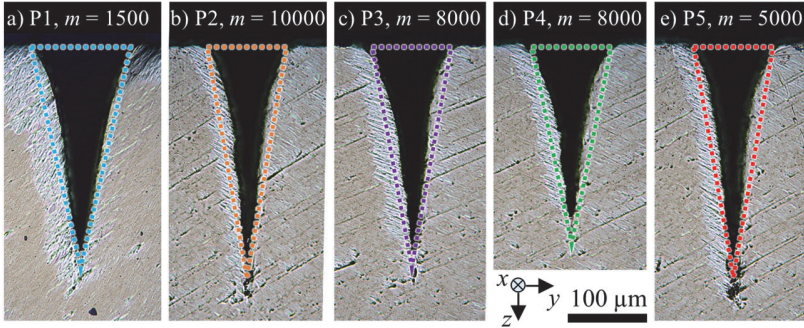


**Figure 2.9** Cross sections of grooves micromachined in Ti6Al4V with a) P1,  $m = 1500$ , b) P2,  $m = 10000$ , c) P3,  $m = 8000$ , d) P4,  $m = 8000$ , and e) P5,  $m = 5000$ . An isosceles triangle with the dimensions of the calculated depth and width of the corresponding groove using the model presented in section 2 is inserted for each parameter set in the respective colour.

Knowing the laser parameters  $E_P$  and  $f_P$ , the scanning speed  $v_x$  and beam radius  $w_0$ , and the three material parameters  $A$ ,  $\delta_{\text{eff}}$  and  $h_V$ , the model allows for the prediction of the groove dimensions as a function of the number of scans  $m$  and maximum achievable groove depth.

## 4 Conclusions

An analytical model for the prediction of the depth and width of V-shaped grooves in metals micromachined with ultrashort laser pulses was derived. The model predicts the progress of the micromachining depth for V-shaped grooves in a Ti-alloy with ultrashort laser pulses as a function of laser parameters, scanning parameters and material parameters. The corresponding assumptions for the model were experimentally validated for different pulse energies, repetition rates, scanning speeds and number of scans using cross sections and optical microscopy. The analytical model

derived in our paper provides a useful tool for the estimation of the groove dimensions, process windows of micromachining with high depth progress and the maximum achievable groove depth.

### **Funding**

This work was funded by the Federal Ministry for Economic Affairs and Climate Action (BMWK) in the frame of the project “BionicTools” (03EN4007G).

### **Acknowledgements**

The authors wish to thank Ulrich Höchner and *Light Conversion* for providing the ultrafast laser *Pharos*. Furthermore, the authors wish to thank Kim Glumann and Nils Ensminger for the support with the experiments and Liane Hoster for the support with the SEM images.

### **3 Investigation of depth-controlled laser milling for reliably achieving the target depth in advanced applications**

Section 1.3.2 highlighted the need for research on depth-controlled laser milling to reliably achieve the targeted depth in two demanding applications. Section 3.1 presents and describes post-processing of depth-controlled laser milling with ultrashort laser pulses of LPBF-generated aluminium parts to reduce the surface roughness and the deviations from the targeted net shape. Additional results with regard to the milling of deep and complex-shaped structures and removal of support structures are reported on in section 3.2. Section 3.3 presents and describes a method based on image processing that was developed for layer-accurate laser milling of stepped repair geometries in CFRP parts.

#### **3.1 High-quality net shape geometries from additively manufactured parts using closed-loop controlled ablation with ultrashort laser pulses**

This section contains a reproduction of the published article [153]. This article is subject to the "CC BY 4.0 Creative Commons" license (<http://creativecommons.org/licenses/by/4.0/>). Changes to text, symbols, equations, figures and numbering of references have been made solely for unification and consistency in this thesis. No changes have been made to the content.

Journal: Advanced Optical Technologies

Date of publication: 11.03.2020

DOI: <https://doi.org/10.1515/aot-2019-0065>

Daniel Holder<sup>1</sup>, Artur Leis<sup>1,2</sup>, Matthias Buser<sup>1</sup>, Rudolf Weber<sup>1</sup>, and Thomas Graf<sup>1</sup>

<sup>1</sup>*Institut für Strahlwerkzeuge (IFSW), University of Stuttgart, Pfaffenwaldring 43, 70569 Stuttgart, Germany*

<sup>2</sup>*Graduate School of Excellence advanced Manufacturing Engineering (GSaME), Nobelstraße 12, 70569 Stuttgart, Germany*

## Abstract

Additively manufactured parts typically deviate to some extent from the targeted net shape and exhibit high surface roughness due to the size of the powder particles that determines the minimum thickness of the individual slices and due to partially molten powder particles adhering on the surface. Optical coherence tomography (OCT)-based measurements and closed-loop controlled ablation with ultrashort laser pulses were utilized for the precise positioning of the LPBF-generated aluminium parts and for post-processing by selective laser ablation of the excessive material. As a result, high-quality net shape geometries were achieved with surface roughness, and deviation from the targeted net shape geometry reduced by 67% and 63%, respectively.

## 1 Introduction

Additive Manufacturing comprises a wide range of different manufacturing processes. With laser powder bed fusion (LPBF) complex metallic parts are generated from slices of selectively molten powder. The process offers a high flexibility with respect to the generation of highly individualized parts, bionic shapes, and light-weight construction [80,81]. The produced parts, however, typically deviate from the targeted net shape to some extent and exhibit high surface roughness values  $R_a$  in the order of 10 to 20  $\mu\text{m}$  due to partially molten powder [84], build orientation, non-ideal process parameters, material shrinkage and the staircase effect [83]. In particular the staircase effect limits the precision of the manufactured parts, while the

---

size of the powder particles determines the minimum thickness of the individual slices [85].

In order to improve precision and surface quality, different post-processing techniques and approaches have been investigated [84,85]. Laser-based approaches such as laser polishing or laser ablation have the advantage of avoiding significant mechanical impact on the post-processed parts. Laser polishing utilizes laser beam melting of the part's surface in order to smoothen the surface roughness by material flow. With this technique the roughness of LPBF parts manufactured from AlSi10Mg powder could be reduced by about 92% to  $R_a = 0.66 \mu\text{m}$  by scanning the surface with a cw-laser, but the shape of the surface topography remained wavy [89]. Waviness and roughness can be further reduced with adapted scanning strategies, e.g. multiple scans with different scanning angles. However, repetitive remelting of the surface layer by laser polishing causes the formation of a growing heat affected zone [87]. This effect can be avoided using laser ablation with short or ultrashort laser pulses, thanks to the reduced thermal load outside of the ablation zone. Laser ablation with a ns-laser allowed to reduce the roughness  $R_a$  of LPBF-generated steel parts from  $19 \mu\text{m}$  to  $5 \mu\text{m}$  and demonstrated that the roughness decreases with an increasing number of scans [86]. An approach using a fs-laser and a CCD-based imaging system to control the beam position during the ablation of LPBF-generated parts is presented in [88]. Ablation of multiple layers with adapted focal position allowed to remove most of the powder particles on the surface and reduced the roughness  $R_a$  from  $22 \mu\text{m}$  to below  $3 \mu\text{m}$ . Furthermore, the circularity of holes that were manufactured in the LPBF process was improved by the removal of excessive material.

Laser ablation cannot only be used to reduce surface roughness, but also to change the macroscopic geometry of the parts by an automated process by using optical coherence tomography (OCT) in combination with a Galvanometer-scanner in order to measure the actual geometry of the post-processed part and determine where further ablation is required [186]. The integration of the OCT-based measurements into a closed-loop control allowed the automated machining of a fabric texture on the original flat steel surface and the reduction of surface roughness compared to open-loop control. Webster *et al.* utilized a similar setup but with fixed optics for automated laser micromachining of heterogeneous materials, e.g. bone and wood. As a result, a remaining root-mean-square (RMS) deviation of the machined depth compared to the designed depth of  $14 \mu\text{m}/\text{pixel}$  for bone and  $35 \mu\text{m}/\text{pixel}$  for wood could be

achieved for a spiral-shaped geometry [14]. The suitability of OCT-based closed-loop controlled ablation of heterogeneous material has also been demonstrated by *Boley et al.* for precise machining of carbon fibre-reinforced plastics (CFRP) with uni-directional fibres. Compared to the open-loop controlled process, the surface roughness  $S_a$  could be reduced from 60  $\mu\text{m}$  to 7  $\mu\text{m}$  and the maximum deviation from the targeted depth was reduced from 200  $\mu\text{m}$  to 20  $\mu\text{m}$  [187]. In addition, the OCT-based measurement enables the determination of the fibre's orientation for layer-accurate laser ablation of CFRP with multidirectional fibres [188] and the detection of the position of the processed part in the working area of a processing station, e.g. during a laser beam decoating process [189].

The described applications show the high potential of OCT-based measurements and closed-loop control during laser ablation of various materials. In the following we present OCT-based closed-loop controlled laser ablation of LPBF-generated aluminium parts with ultrashort laser pulses in order to reduce the surface roughness and improve the geometrical accuracy. The OCT-measurements were used for both, the precise positioning of the workpiece and to determine the areas where further ablation is required to reach the targeted net shape of the additively produced parts. This approach combines the advantages of additive and subtractive laser manufacturing processes in order to create 3D-shaped geometries with high freedom of design and high precision. Section 2 presents the components and methods that are required for closed-loop controlled laser ablation of additively manufactured aluminium parts with ultrashort laser pulses and the analysis of the post-processed parts regarding their surface roughness and shape deviation. The impact of different peak fluences on the resulting surface roughness and surface structure of flat LPBF-generated aluminium parts is discussed in section 3 in order to determine suitable process parameters for the shape enhancement of various 3D-shaped geometries. Finally, the presented approach is evaluated with regard to the removal of surface defects and the achievable accuracy of manufacturing different geometries.

## 2 Methods

The approach of creating precise 3D-shaped geometries by first additive and then subtractive laser manufacturing processes is shown schematically in Figure 3.1.

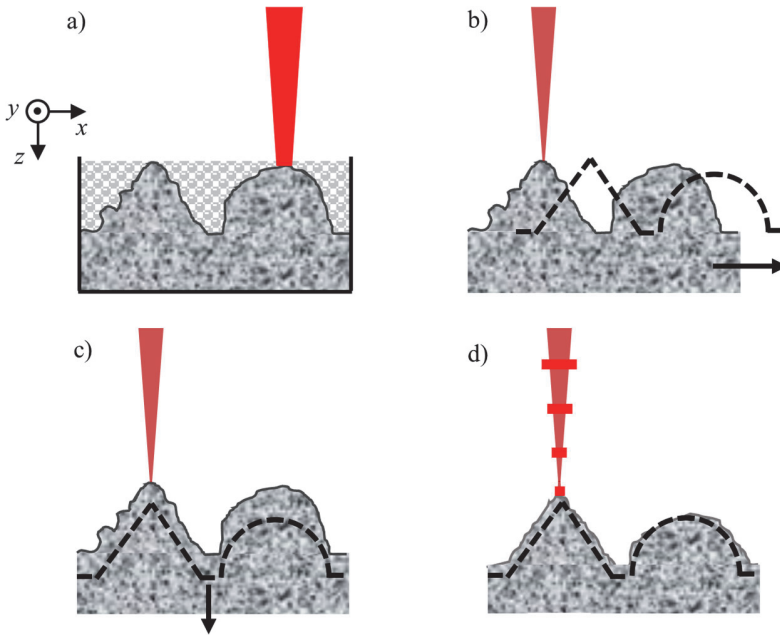


**Figure 3.1** The different steps of the used manufacturing process of 3D-shaped parts: a) LPBF process of the raw part with a cw laser; b) positioning of the raw part with the help of OCT-measurements to match to the position of the target geometry; c) axial offset of target geometry; d) Post-processing of the raw part with OCT-based closed-loop controlled ablation using ultrashort laser pulses.

Two different processing stations had to be utilized in order to manufacture the parts by LPBF (Figure 3.1 a) and post-process the parts by closed-loop controlled laser ablation with ultrashort laser pulses (Figure 3.1 d). Therefore, selective and local post-processing by controlled ablation requires precise positioning of the previously manufactured raw part with respect to the laser processing beam. With OCT-based measurements, positioning can be achieved with an accuracy of a few microns. This was achieved with an iterative procedure in which the processing field was measured, the current position of the workpiece compared with the target position (black dotted line in Figure 3.1 b), and the part moved and rotated until the deviations of current position and target position were minimized. The centre of the processing

field was defined as target position for processing of the part, as large deflection angles of the OCT-beam caused errors in the OCT-measurements. The target geometry for the controlled ablation process was identical to the one of the LPBF process, but with an axial offset of  $z = 400 \mu\text{m}$  shifted into the part (Figure 3.1) in order to assure that the whole part is ablated at least for a few scans, as this removed most of the powder particles in [88].

## 2.1 Additive manufacturing of aluminium parts

The parts were manufactured from an AlSi10Mg powder with a particle size between  $20 \mu\text{m}$  and  $56 \mu\text{m}$ . The LPBF process was performed in a *TruPrint 3000* machine from *Trumpf* in the transient regime between heat conduction and deep penetration welding at an average laser power of  $430 \text{ W}$  focused onto the powder bed with a beam diameter of  $100 \pm 5 \mu\text{m}$ . The beam was moved over the powder bed with a scanning speed of  $1300 \text{ mm/s}$  and a hatching distance of  $180 \mu\text{m}$  generating layer thicknesses of about  $60 \mu\text{m}$ . Nitrogen was used as inert gas to avoid oxidation. The temperature of the substrate plate was constantly kept at  $200^\circ\text{C}$ .

Two different geometries were manufactured. The first one, a simple plane part, was processed with various peak fluences in order to investigate their impact on the resulting surface topography. The roughness of the plane sample before post-processing was measured to be  $S_a = 14.1 \pm 1.7 \mu\text{m}$ , which is consistent with typically achieved roughness values of additively-manufactured parts [85]. The second one, a more complex geometry, is shown in Figure 3.2 and includes different challenges when creating additively manufactured 3D-shaped parts. Inclined surfaces with different orientations (e.g. cone, pyramid) and inclination angles (e.g. half sphere) are used to investigate the staircase effect. Sharp edges (e.g. pyramid), steep transitions (e.g. steps) and thin tip (e.g. cone, pyramid) are suitable to determine the achievable precision regarding the manufacturing of given geometrical features. The lateral dimensions of the sample geometry were  $8 \times 8 \text{ mm}^2$  with a maximum height of  $1.5 \text{ mm}$ . The grayscale of the geometry shown in Figure 3.2 is linearly scaled between maximum height (white,  $1.5 \text{ mm}$ ) and minimum height (black,  $0 \text{ mm}$ ).

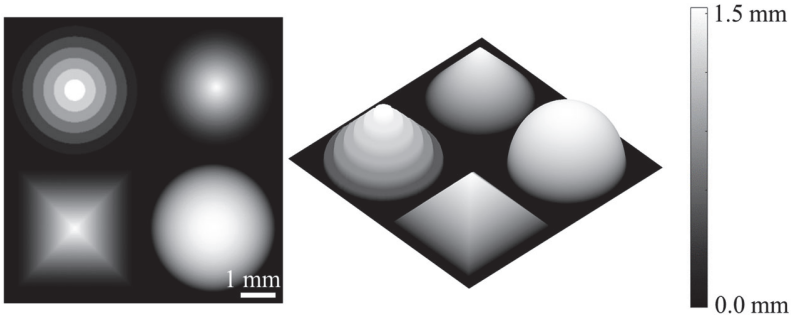


**Figure 3.2** Grayscale image of the target geometry from plan view and oblique view.

## 2.2 Closed-loop controlled ablation with ultrashort laser pulses

The setup for post-processing by means of closed-loop controlled laser ablation consists of three major components: The OCT system to detect the location of the surface and the shape of the workpiece, the processing laser system and the control system. Optical measurements of the surface were performed with the Fourier-domain OCT-based system *CHRcodile 2* from *Precitec* which provides an axial measurement range of about 6 mm. The measuring rate was set to 70 kHz. The processing laser system *Femto 30* from *Fibercryst* used for post-processing of the additively manufactured aluminium parts in this study emits laser pulses at a wavelength of 1030 nm and linear polarization with a pulse duration of  $\tau_P = 600$  fs and a beam quality factor  $M^2 < 1.3$ . The laser system was operated at the same repetition rate  $f_P = 70$  kHz as the measuring rate of the OCT in order to be able to measure the changes of the surface induced by every single applied laser pulse. Pulse energies of up to 85.7  $\mu\text{J}$  were used in the ablation experiments, corresponding to a maximum average power of 6 W.

The beams of the OCT and the processing laser were superposed by means of a dichroic mirror as shown schematically in Figure 3.3. The dichroic mirror was HR-coated for the beam of the processing laser at a wavelength of  $\lambda_L = 1030$  nm and AR-coated for the beam of the OCT centred at a wavelength of  $\lambda_O = 1080$  nm. Both beams were guided through a Galvanometer-scanner system for deflection. The focal

length of the used F-Theta lens was 163 mm resulting in focal diameters of  $50\pm 5\ \mu\text{m}$  for the processing laser and  $15\pm 5\ \mu\text{m}$  for the beam of the OCT.

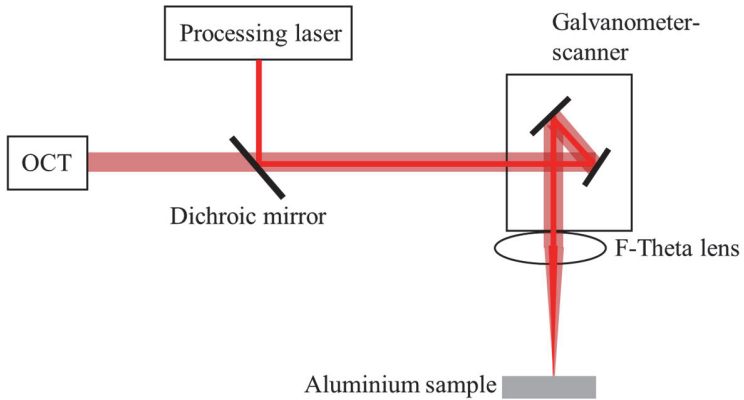


**Figure 3.3** Setup of the OCT-based closed-loop controlled laser ablation processes.

The pulse overlap in and perpendicular to the scanning direction was kept at 84% in order to avoid heat accumulation effects by pulse-to-pulse or scan-to-scan accumulation [106]. This was achieved using a scanning speed of  $v_x = 560\ \text{mm/s}$  and a hatching distance of  $8\ \mu\text{m}$ . The principle of the control system was already introduced in [187] and [188].

### 2.3 Analysis of surface roughness and shape deviation

Six different orders of shape deviations are defined in DIN 4760. The shape deviations are differentiated according to spatial dimensions and range from deviations of the characteristic dimensions of the part, e.g. increased length or thickness in the first order to increased surface roughness in the fourth order and the crystal structure in the sixth order [67]. In this work, the surfaces of the additively manufactured parts with and without post-processing by OCT-controlled ablation were analysed with regard to shape deviations of the first and the fourth order using a *Keyence 3D-Laser Scanning Microscope (LSM) VK-9710-K*. Furthermore, the surface structure of the surface was investigated using a scanning-electron-microscope (SEM) *Jeol JSM-6490LV*.

Using an objective with a magnification of 20 on the LSM for the measurement of the roughness led to a lateral resolution of 0.69  $\mu\text{m}/\text{pixel}$ . The axial scanning pitch was 0.2  $\mu\text{m}$ . The arithmetical mean height

$$S_a = \frac{1}{G \cdot H} \sum_{g=1}^G \sum_{h=1}^H \left| z(x_g, y_h) - \langle z \rangle \right|, \quad (3.1)$$

where  $z$  is the height measured at the coordinates  $x_g$  and  $y_h$  and  $G$  and  $H$  are the number of pixels, was determined according to EN ISO 25178 and was used to assess the effectiveness of the closed-loop controlled ablation with respect to the reduction of the surface roughness and hence the reduction of fourth-order deviations for additively manufactured parts. The effectiveness was investigated for different peak fluences

$$\phi_0 = \frac{2 \cdot E_p}{\pi \cdot w_0^2} \quad (3.2)$$

where  $E_p$  is the pulse energy and  $w_0$  the radius of the processing laser beam. For the evaluation of the first-order deviations from the net shape an objective with a magnification of 10 was used, leading to a lateral resolution of 1.38  $\mu\text{m}/\text{pixel}$ . The axial scanning pitch was 0.2  $\mu\text{m}$ . The mean deviation was calculated by

$$D_a = \frac{1}{G \cdot H} \sum_{g=1}^G \sum_{h=1}^H \left| z(x_g, y_h) - z_T(x_g, y_h) \right|, \quad (3.3)$$

where  $z_T$  is the targeted height of the workpiece.

### 3 Quality enhancement of additively manufactured parts by closed-loop controlled laser ablation with ultrashort laser pulses

#### 3.1 Smoothing of surface topography

Squared areas of  $1 \times 1 \text{ mm}^2$  were ablated on the plane samples using the setup and parameters described in section 2.2 with different peak fluences ranging from  $0.2 \text{ J/cm}^2$  to  $8.6 \text{ J/cm}^2$ . The targeted ablation depth of the closed-loop controlled post-processing was set to  $100 \text{ }\mu\text{m}$ . The number of scans to achieve the targeted ablation depth varied between 70 and 300, depending on the applied peak fluence. The lowest peak fluence of  $0.2 \text{ J/cm}^2$  required 300 scans and the highest peak fluence of  $8.6 \text{ J/cm}^2$  required 70 scans to reach the targeted depth of  $100 \text{ }\mu\text{m}$ . The impact of the peak fluence on the mean height  $S_a$  and the surface structure is shown in Figure 3.4 and Figure 3.5, respectively. The areas for the measurements by LSM and SEM were manually selected to represent the overall surface of the processed area.

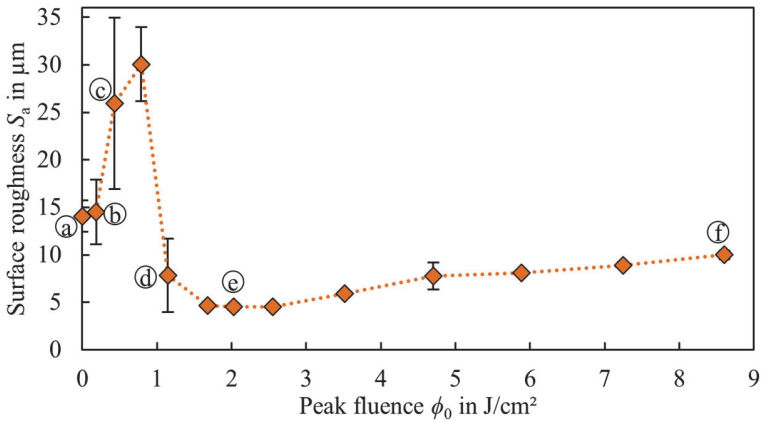


**Figure 3.4** Measured roughness  $S_a$  as a function of the applied peak fluence. The dashed line was inserted to guide the eye. The value at  $0 \text{ J/cm}^2$  represents the surface roughness of a non-ablated area on the test sample. Data points with corresponding SEM images in Figure 3.5 are marked with a) to f). Laser wavelength  $\lambda_L = 1030 \text{ nm}$ , pulse duration  $\tau_p = 600 \text{ fs}$ , repetition rate  $f_p = 70 \text{ kHz}$ , scanning speed  $v_x = 560 \text{ mm/s}$ .

The application of  $\phi_0 = 0.2 \text{ J/cm}^2$  leads to  $S_a = 14.5 \pm 3.4 \text{ }\mu\text{m}$ , which is close to the roughness value of  $S_a = 14.1 \pm 1.7 \text{ }\mu\text{m}$  of the non-ablated surface. However, the surface structures of these surfaces differ in shape and size, as shown in Figure 3.5 a) and b). Solidified melt drops, probably due to spatter formation during the LPBF process, and adhering powder particles are present on the non-ablated surface. The surface irradiated with  $0.2 \text{ J/cm}^2$  contains no solidified melt drops and shows a coarse surface with partially removed material, leading to pits with a depth of up to  $30 \text{ }\mu\text{m}$ .

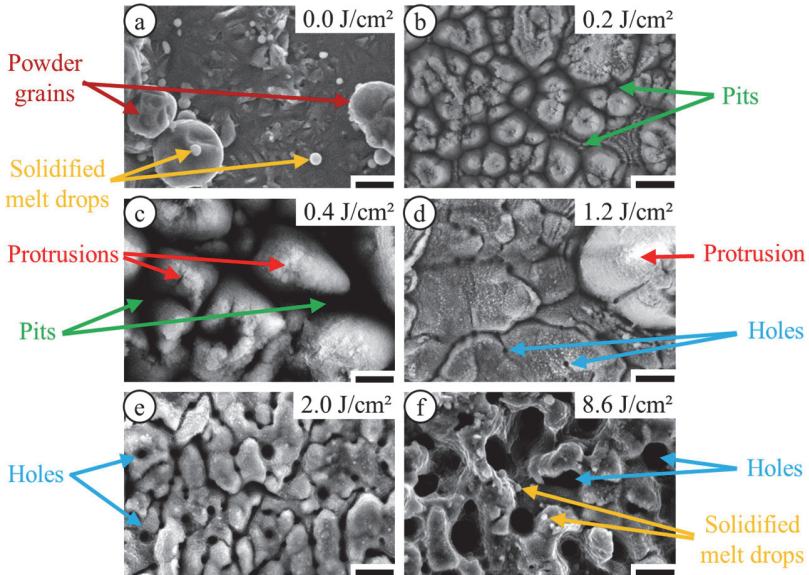


**Figure 3.5** Surface structure of the LPBF-generated test sample measured by the SEM after post processing with different applied peak fluences between 0.2 and 8.6 J/cm<sup>2</sup>. Scale bars represent a length of 20  $\mu\text{m}$ . Laser wavelength  $\lambda_L = 1030$  nm, pulse duration  $\tau_p = 600$  fs, repetition rate  $f_p = 70$  kHz, scanning speed  $v_s = 560$  mm/s.

The application of peak fluences exceeding  $\phi_0 = 0.4$  J/cm<sup>2</sup> and  $\phi_0 = 0.8$  J/cm<sup>2</sup> significantly increases the measured surface roughness to  $S_a = 25.9 \pm 9.0$   $\mu\text{m}$  and  $S_a = 30.1 \pm 3.9$   $\mu\text{m}$ , respectively. The inhomogeneous material removal results in pits as deep as 100  $\mu\text{m}$  and the increased roughness  $S_a$  (Figure 3.5 c). The growth of the pits is probably partially initiated by particles on top of the protrusions which act as light scattering centres. Increasing the applied peak fluence to  $\phi_0 = 1.2$  J/cm<sup>2</sup> leads to a significant reduction of the roughness to  $S_a = 7.8 \pm 3.9$   $\mu\text{m}$ , much lower than the initial value of  $S_a = 14.1 \pm 1.7$   $\mu\text{m}$ . Homogeneous material removal yields a smoothed surface without large pits and a reduced number of protrusions as can be seen in Figure 3.5 d). However, individual protrusions remain, which in combination with observations at lower peak fluence leads to the assumption that the complete removal of the protrusions require higher peak fluences. Additionally, small holes with a diameter of 3 to 5  $\mu\text{m}$  and a depth of up to 10  $\mu\text{m}$  can be seen in the grooves on the surface next to the remaining protrusion in Figure 3.5 d).

The lowest surface roughness of  $S_a = 4.6 \pm 0.3 \mu\text{m}$  was achieved within the range of  $1.7 \text{ J/cm}^2 < \phi_0 < 2.6 \text{ J/cm}^2$ , where no protrusions or large pits remained on the surface, as can be seen in Figure 3.5 e). The diameter and depth of the holes on the surface are increased to 4 to 6  $\mu\text{m}$  and 25  $\mu\text{m}$ , respectively.

With peak fluences exceeding  $2.6 \text{ J/cm}^2$ , the measured roughness is increased again due to the increased diameter and greater depth of the holes. This can be seen particularly well in Figure 3.5 f) in the form of a fissured surface with holes with diameters of up to 20  $\mu\text{m}$ , leading to a surface roughness of  $S_a = 10.0 \pm 0.5 \mu\text{m}$ . Furthermore, solidified melt drops can be seen again on the surface in between the holes, indicating an explosive melt ejection process, which was also observed in [190] at high irradiated peak fluences. The impact of peak fluences above  $1.2 \text{ J/cm}^2$  on the modulation period of the surface structure is consistent with the observations for the irradiation of steel with femtosecond laser pulses shown in [191]. Peak fluences in the range between  $1.7 \text{ J/cm}^2$  and  $2.6 \text{ J/cm}^2$  should be applied in order to reduce the roughness  $S_a$  by 67% as compared to the original surface.

### 3.2 Creating high-quality net shape geometries

The additively manufactured part of the 3D-shaped geometry shown in Figure 3.1 was positioned according to the method presented in section 2. The beam was focused on the highest position of the raw part ( $z = 0 \mu\text{m}$ ), where the peak fluence was set to  $\phi_0 = 3.5 \text{ J/cm}^2$ , as the focus position could not be adjusted within the control algorithm. The effective peak fluence on the workpiece is reduced with increasing ablation depth due to the divergence of the beam, but the peak fluence did not fall below the range of  $1.7 \text{ J/cm}^2 < \phi_0 < 2.6 \text{ J/cm}^2$  needed to achieve the minimum roughness as shown in Figure 3.4. On average about 400  $\mu\text{m}$  were ablated using a peak fluence of  $\phi_0 = 3.5 \text{ J/cm}^2$  and 1140 scans.

The SEM image of the cone-shaped geometry after the LPBF-process is seen in Figure 3.6 a). Several powder particles are present on the surface of the raw part and the tip is rounded off. The quantified deviations of the raw part from the targeted net shape are shown in Figure 3.6 b). The green colour corresponds to small deviations of less than  $\pm 15 \mu\text{m}$  and represents a high conformity of the manufactured part with the targeted geometry. Positive deviations of up to 150  $\mu\text{m}$  (dark red) reveal excessive material on the surface of the measured part, e.g. adherent, partially molten

powder particles which are present in the border areas of the image. Correspondingly, negative deviations of up to  $-150\ \mu\text{m}$  (dark blue) reveal missing material of the measured part, e.g. a thin tip that is too small to be manufactured in the LPBF-process due to slicing and minimum size of the powder particles. The slicing also prevents the manufacturing of smooth inclined surfaces, indicated by the ring-shaped deviations in Figure 3.6 b). These artefacts are also the reason for the rather high mean deviation  $D_a = 38.2\ \mu\text{m}$  of the raw part compared to  $D_a = 14.3\ \mu\text{m}$  of the post-processed part.

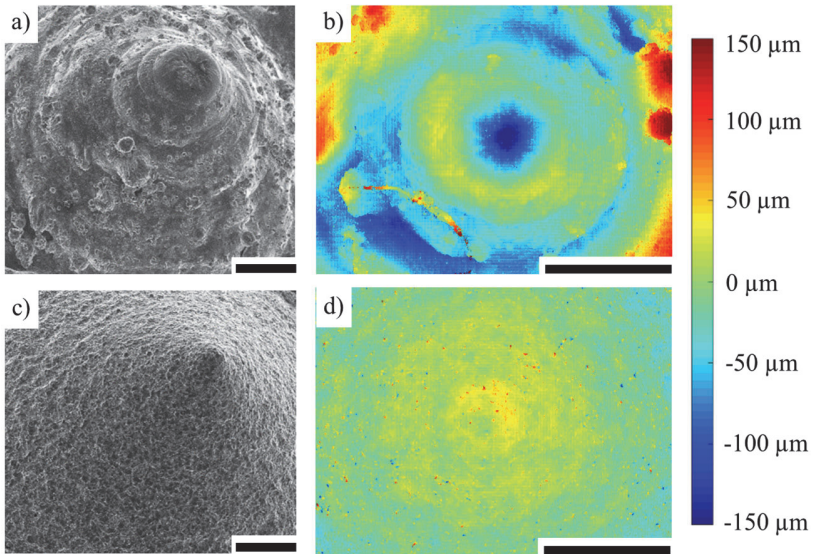


**Figure 3.6** Cone-shaped geometry: a) SEM image (oblique view) of the raw part manufactured by LPBF; b) Deviation of the raw part from the targeted geometry measured by LSM; c) SEM image (oblique view) of the post-processed part; d) Deviation of the post-processed part from the targeted net shape measured by LSM. Scale bars represent a length of  $500\ \mu\text{m}$ . Laser wavelength  $\lambda_L = 1030\ \text{nm}$ , pulse duration  $\tau_p = 600\ \text{fs}$ ,  $\phi_0 = 3.5\ \text{J}/\text{cm}^2$ , repetition rate  $f_r = 70\ \text{kHz}$ , scanning speed  $v_x = 560\ \text{mm}/\text{s}$ .

The SEM image of the post-processed part is shown in Figure 3.6 c). It does not have any partially molten powder particles adhering to the surface and exhibits a pronounced tip and a smooth conical surface. This visual impression is confirmed by the quantified deviation chart in Figure 3.6 d). Some remaining excessive material

in the order of  $20\ \mu\text{m}$  to  $40\ \mu\text{m}$  and a number of very small spots with deviations up to  $\pm 100\ \mu\text{m}$  can be seen near the tip. Since these dots are not seen in the SEM picture c) it can be assumed that this are measurement artefacts of the LSM.

Powder particles on the surface, a rounded off tip and wavy surface are also seen in the SEM and the deviation plot of the pyramid-shaped raw part in Figure 3.7 a) and b).

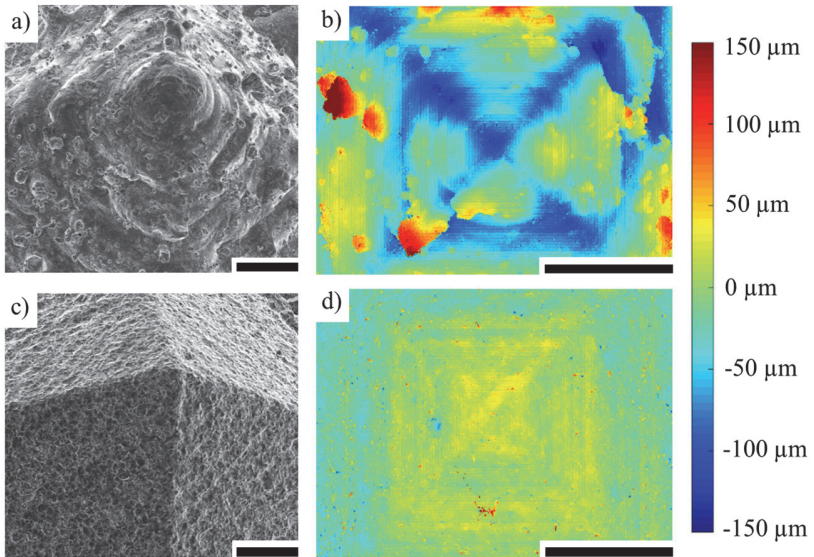


**Figure 3.7** Pyramid-shaped geometry: a) SEM image (oblique view) of the raw LPBF-generated part; b) Deviation of the raw part from the target geometry measured by LSM; c) SEM image (oblique view) of post-processed part; d) Deviation of the post-processed part from target geometry measured by LSM. Scale bars represent a length of  $500\ \mu\text{m}$ . Laser wavelength  $\lambda_L = 1030\ \text{nm}$ , pulse duration  $\tau_p = 600\ \text{fs}$ ,  $\phi_0 = 3.5\ \text{J}/\text{cm}^2$ , repetition rate  $f_p = 70\ \text{kHz}$ , scanning speed  $v_x = 560\ \text{mm}/\text{s}$ .

The edges of the pyramid deviate by  $-100 \pm 25\ \mu\text{m}$  (dark blue). As was the case with the tip, the cause of the deviations on the edges of the pyramid are again found in the LPBF-process due to slicing and the minimum size of the powder particles. The additional deviations on the edges lead to a significantly higher mean deviation of  $D_a = 43.5\ \mu\text{m}$  compared to the cone-shaped geometry with  $D_a = 38.2\ \mu\text{m}$ . In contrast

to this, the mean deviation of the pyramid-shaped post-processed part with  $D_a = 14.9 \mu\text{m}$  is close to  $D_a = 14.3 \mu\text{m}$  of the cone-shaped geometry, indicating that edges on inclined surfaces in the target geometry can well be manufactured by post-processing. This is also revealed by the SEM image and the deviation plot in Figure 3.7 c) and d) that show no significant deviations in the area of the edges.

The SEM and deviation images of the step-shaped geometry are shown in Figure 3.8.

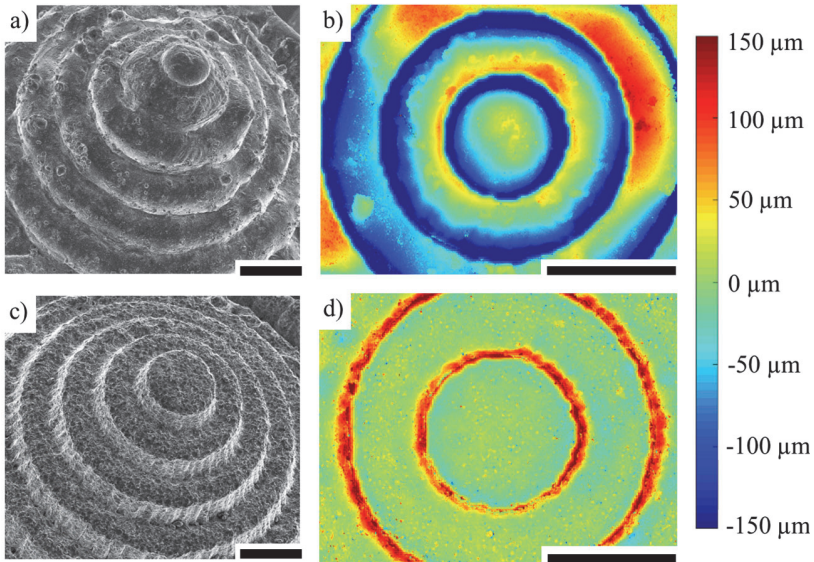


**Figure 3.8** Step-shaped geometry: a) SEM image (oblique view) of raw LPBF-generated part; b) Deviation of the raw part from the target geometry measured by LSM; c) SEM image (oblique view) of the post-processed part; d) Deviation of the post-processed part from target geometry measured by LSM. Scale bars represent a length of  $500 \mu\text{m}$ . Laser wavelength  $\lambda_l = 1030 \text{ nm}$ , pulse duration  $\tau_p = 600 \text{ fs}$ ,  $\phi_0 = 3.5 \text{ J/cm}^2$ , repetition rate  $f_p = 70 \text{ kHz}$ , scanning speed  $v_x = 560 \text{ mm/s}$ .

High positive and negative deviations with irregular shaped steps of the raw LPBF-generated part can be seen in the SEM image in Figure 3.8 a). The radii of the different circular steps are about  $50 \mu\text{m}$  smaller than specified with the target geometry, which was caused due to the limited minimum feature size in the LPBF process. Deviations of  $\pm 30 \mu\text{m}$  from the targeted step height of  $250 \mu\text{m}$  resulted from the

layer thickness of  $60\ \mu\text{m}$ , since the layer thickness is not an integer divider of the step height. The edges of the steps are rounded off due to the surface tension of the liquid melt in the LPBF process, preventing the manufacturing of sharp edges and steep flanks. These limits of the LPBF process cause a high mean deviation of  $D_a = 74.7\ \mu\text{m}$  which can be reduced to  $D_a = 23.5\ \mu\text{m}$  by post-processing. Although the radii of the raw part were about  $50\ \mu\text{m}$  too small, the radii and height of the different steps of the post-processed part are consistent with those of the target geometry. This was enabled by the axial offset of the target geometry of  $400\ \mu\text{m}$  into the workpiece, resulting in enough material available for compensation. However, a taper angle is present on the sidewalls between two adjacent steps, which is represented as excessive material (dark red) in Figure 3.8 d). The formation of a taper angle is a well-known phenomenon from laser drilling and cutting [58] which can be minimized using helical optics [192].

The SEM and deviation image of the half-sphere-shaped geometry are shown in Figure 3.9. The deviations of the raw part from the target geometry are mainly caused by excessive material on the surface, again due to adherent powder particles and the minimum layer thickness of the LPBF process. The mean deviation was calculated to be  $D_a = 43.2\ \mu\text{m}$ . These deviations were effectively removed by post-processing, resulting in a smooth surface and a low mean deviation of  $D_a = 9.9\ \mu\text{m}$ .

The investigations confirm the high potential of OCT-based closed-loop controlled laser ablation with ultrashort laser pulses for manufacturing of different high-quality net shape geometries from LPBF-generated aluminium parts. Depending on the geometry, the mean deviation was reduced by at least 63% by selective ablation of excessive material resulting from the slicing in the LPBF process. Features like thin tips, smooth inclined surfaces and pronounced edges can be realized using the presented approach. The results show the great potential that is offered by combining different laser-based manufacturing processes [5].

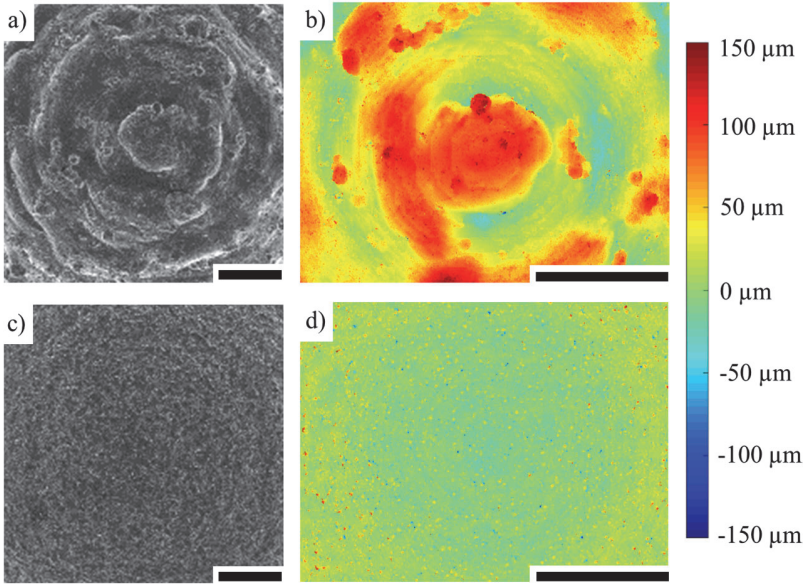


**Figure 3.9** Half-sphere-shaped geometry: a) SEM image (oblique view) of the raw LPBF-generated part; b) Deviation of the raw part from the target geometry measured by LSM; c) SEM image (oblique view) of post-processed part; d) Deviation of the post-processed part from target geometry measured by LSM. Scale bars represent a length of 500  $\mu\text{m}$ . Laser wavelength  $\lambda_L = 1030$  nm, pulse duration  $\tau_p = 600$  fs,  $\phi_0 = 3.5$  J/cm<sup>2</sup>, repetition rate  $f_p = 70$  kHz, scanning speed  $v_x = 560$  mm/s.

#### 4 Conclusion

In summary, we have presented a post-processing method for LPBF-generated aluminium parts based on OCT closed-loop controlled laser ablation with ultrashort laser pulses that can be used to reduce the surface roughness and the shape deviations. The surface roughness was reduced by about 67% to  $S_a = 4.6 \pm 0.3$   $\mu\text{m}$  by applying a suitable peak fluence in the range of 1.7 J/cm<sup>2</sup> to 2.6 J/cm<sup>2</sup> in order to avoid cavities or protrusions on the surface while minimizing surface defects. The OCT-measurements were used for both, precise positioning of the raw part and determination of the areas where further ablation is required to reach the targeted net shape. Post-processing by closed-loop controlled ablation reduced the mean deviation of the manufactured part from the target geometry by 63% to 77% for different shapes such

as cone, pyramid, steps and a half sphere. Precise manufacturing of geometrical features like thin tips, smooth inclined surfaces and pronounced edges was realized using the presented post-processing method. Future work will include the removal of support structures and integration of functional structures by laser ablation into the manufactured parts.

### Acknowledgements

The authors thank Markus Kogel-Hollacher and *Precitec* for the loan of the OCT-based measurement system *CHRcodile 2*, *Fibercryst* for the loan of the ultrafast laser *Femto 30*, and *Trumpf* for the deployment of the LPBF machine *TruPrint 3000* as part of the project *GrantSLAM* and in cooperation with *GSaME*. Furthermore, the authors thank Johannes Wahl for the SEM images and Gennadij Nikitin for the LSM measurements.

## 3.2 Additional results for additively manufactured parts built with support structures

Depth-controlled micromachining was also used for the removal of support structures from LPBF-generated parts made from Ti6Al4V and for subsequent smoothing and milling of deep and complexly shaped geometries. The results of the investigations were published in [193]. Only the main differences in terms of the laser system and the processed material as well as the main results of this publication are summarised in the following, since this publication has a similar introduction and methodology as the publication presented in section 3.1.

The ultrafast laser system *Pharos* from *Light Conversion* with a wavelength of  $\lambda_L = 1030$  nm and a pulse duration of  $\tau_P = 260$  fs was used for micromachining. The laser beam was linearly polarized and had a beam propagation factor of  $M^2 < 1.3$ . The maximum average power on the processed surface was 13 W, which corresponds to a maximum pulse energy of  $E_P = 260$   $\mu$ J at the pulse repetition rate of  $f_P = 50$  kHz. The measuring rate of the OCT-based depth measurement system was set to 50 kHz to correspond to the pulse repetition rate of the processing laser. Both

beams were superimposed by means of a dichroic mirror, guided through a Galvanometer-scanner and focused by an F-Theta lens with a focal length of  $f=163$  mm. The resulting focal diameters of the processing laser beam and the OCT probe beam were  $60\pm 5$   $\mu\text{m}$  and  $15\pm 5$   $\mu\text{m}$ , respectively.

The samples were generated by LPBF from a Ti6Al4V powder that had a distribution of the diameter of particles between 15  $\mu\text{m}$  and 45  $\mu\text{m}$ . A single-mode fibre laser with a wavelength of 1075 nm, an average power of 155 W and a beam diameter of 30  $\mu\text{m}$  was used to melt layers with a thickness of 20  $\mu\text{m}$  in an inert gas atmosphere of argon without an additionally heated substrate. Block support structures were generated first to fix the generated part to the base plate during the LPBF process. The block support structures were built with a wall distance of 700  $\mu\text{m}$  and a wall height of 800  $\mu\text{m}$ . The part was generated with lateral dimensions of 8 mm and a thickness of approximately 1.5 mm by hatching with a scanning speed of 1.2 m/s and a line hatching distance of 60  $\mu\text{m}$ .

An image of the LPBF-generated sample is shown in Figure 3.10 a). The sample was flipped after the LPBF process to characterize the support structures. Smearred material adhered locally between the support structures due to the sample being mechanically sawed off the base plate of the powder bed (Figure 3.10 a)). The excess material from the support structures was detected and measured by OCT-based depth measurement, as shown by the false colour representation in Figure 3.10 b).

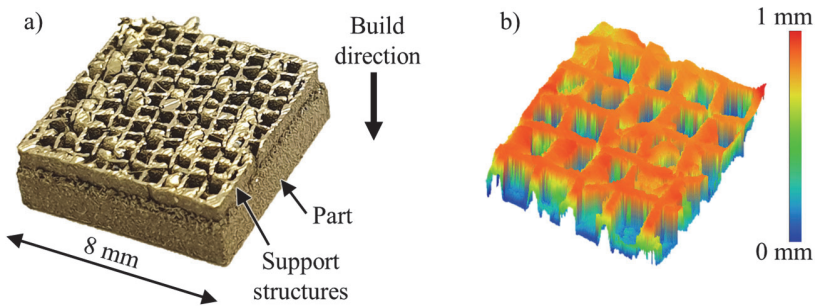


**Figure 3.10** a) Image and b) section of the OCT-based depth measurement of the LPBF-generated sample made from Ti6Al4V built with block support structures. The sample was flipped after the LPBF process to characterize the support structures.

The spatial offset between pulses in scanning direction and perpendicular to the scanning direction was kept constant at  $15\ \mu\text{m}$  during depth-controlled micromachining, which corresponds to an overlap of 74%. This was obtained by using a scanning speed of  $v_x = 750\ \text{mm/s}$  and a line hatching distance of  $p_y = 15\ \mu\text{m}$ . The target depth was set to  $100\ \mu\text{m}$  below the surface of the actual part in order to completely remove the excess material. The maximum available average power of  $P = 13\ \text{W}$  was used for the removal of the support structures at a peak fluence of  $\phi_0 = 20.2\ \text{J/cm}^2$ . The axial position of the beam waist of both beams was set to be on the top surface of the support structures. The support structures were completely removed from the sample after depth-controlled micromachining with 400 scans over the surface. Figure 3.11 depicts the surface topography before (red coloured area, Figure 3.11 a)) and after depth-controlled micromachining of the part (yellow coloured area, Figure 3.11 b)).

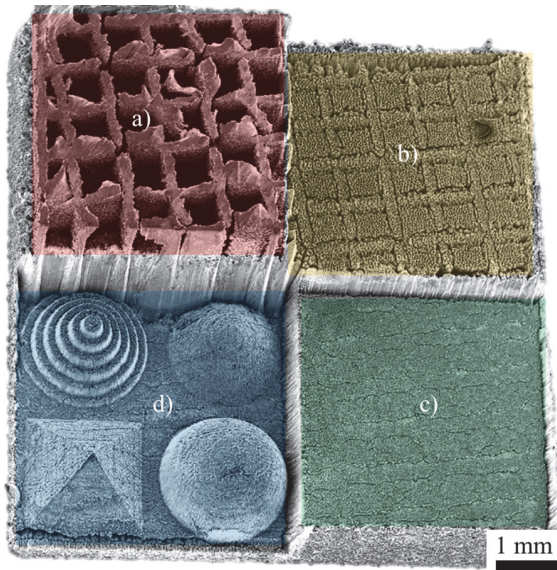


**Figure 3.11** SEM image of the LPBF-generated sample after different stages of post-processing, indicated by different colouration: a) No post-processing (red), b) support structures removed (yellow), c) support structures removed and the surface smoothed (green) and d) support structures removed and different geometries machined into the sample (blue).

A lattice-shaped surface structure is visible on the sample marked by the yellow-coloured area of Figure 3.11 b), with pits with a depth of up to 100  $\mu\text{m}$  between the former support structure and the surface of the sample. The pits are deeper than the targeted machining depth and presumably result from the reflection of the laser beam on the sidewalls of the support structures. The formation of rough surface structures as well as the formation of the pits yield a rather high surface roughness of  $S_a = 33.7 \mu\text{m}$ .

An additional smoothing step was therefore applied using depth-controlled micromachining at a lower peak fluence of  $\phi_0 = 1.9 \text{ J/cm}^2$  and for 2400 scans. The position of the beam waist was shifted to the surface level of the previous target depth and the new target depth was set to 600  $\mu\text{m}$  below this surface level. The green-coloured area in Figure 3.11 c) shows the surface topography after the removal of the support structures and the additional smoothing. A fine lattice-shaped surface structure is still visible on the surface with pits with a depth of up to 30  $\mu\text{m}$ . The surface roughness was reduced by 81% to  $S_a = 6.3 \mu\text{m}$  compared to the roughness  $S_a = 33.7 \mu\text{m}$ , which was measured after the removal of the support structures.

Depth-controlled micromachining also allows direct machining of different geometries in addition to post-processing of a predetermined geometry (presented in the publication in the previous section), removal of support structures and smoothing of the surface. Geometries with different challenges for an LPBF process such as sharp contours, thin tips, and inclined surfaces were fabricated after the removal of the support structures using depth-controlled laser micromachining with a peak fluence of  $\phi_0 = 1.9 \text{ J/cm}^2$  and 3700 scans. The result is shown by the blue-coloured area in Figure 3.11 d). High-quality geometries with well-pronounced features of each shape and a smooth surface were achieved. The mean shape deviation calculated from the OCT-based depth measurements across all geometries was low with  $D_a = 16.3 \mu\text{m}$ .

### **3.3 Image processing based detection of the fibre orientation during depth-controlled laser ablation of CFRP monitored by optical coherence tomography**

This section contains a reproduction of the published article [154]. This article is subject to the "CC BY 4.0 Creative Commons" license (<http://creativecommons.org/licenses/by/4.0/>). Changes to text, symbols, equations, figures and numbering of references have been made solely for unification and consistency in this thesis. No changes have been made to the content.

Journal: Materials and Design

Date of publication: 13.02.2021

DOI: <https://doi.org/10.1016/j.matdes.2021.109567>

Copyright: © Elsevier Ltd

Daniel Holder<sup>1</sup>, Matthias Buser<sup>1</sup>, Steffen Boley<sup>1</sup>, Rudolf Weber<sup>1</sup>, and Thomas Graf<sup>1</sup>

<sup>1</sup>*Institut für Strahlwerkzeuge (IFSW), University of Stuttgart, Pfaffenwaldring 43, 70569 Stuttgart, Germany*

#### **Abstract**

Layer-accurate and precisely stepped removal of damaged areas is required for the repairing process of parts made of carbon fibre-reinforced plastic (CFRP) to obtain a high bonding strength of the repair plies in the rebuilding process. Conventional techniques are characterized by a high degree of manual labour and mechanical load of the processed part. Here, a novel laser-based and controlled approach for automated and layer-accurate removal of damaged areas is presented. In-line depth measurements by optical coherence tomography during nanosecond laser ablation enable depth-controlled homogeneous material removal with minimum damage <10 µm

and low surface roughness in the range of 7  $\mu\text{m}$  to 13  $\mu\text{m}$ . The processed layer must be detected for an unknown or varying layer thickness to stop the ablation process at the interface between two layers and not somewhere within one ply. The image processing-based determination of the fibre orientation from the depth measurements allow for a reliable online detection of the processed layer with a maximum error of  $4^\circ$  and root mean square error of  $1.1^\circ$ . As a result, layer-accurate damage removal is demonstrated for a complex repairing geometry. The suitability of the automated laser-based approach as preparation for repairing is proven by cross-sections and scanning-electron-microscopy.

## **1 Introduction**

Carbon Fibre Reinforced Plastic (CFRP) materials are used for structural components in aeronautical applications due to their light weight, high strength and stiffness [194]. Damages that may occur during the service life of these components need to be detected and removed [92]. The extent of damage in CFRP components can be detected with techniques such as 3D X-ray tomography [195] or laser-ultrasound scanning [196]. The damaged area is removed and prepared for the rebuilding process in a tapered scarf geometry or stepped geometry [92], whereas the latter is easier to perform [75] with conventional procedures such as sanding or grinding. Drawbacks of these conventional procedures are the high degree of manual labour and thus the dependency on the skills of the worker on the quality of the result [197] as well as the lack of reproducibility. End milling is a technique that allows for automated and reproducible removal of damaged areas. However, milling often results in matrix cracks, damaged fibre-matrix interfaces and partially debonded fibres [198] which can decrease the structural strength of the processed part. Furthermore, cleaning of the processed surfaces is required after mechanical treatment to remove particle residues and contaminants from the surface which reduce the bond strength of adhesively bonded parts [198]. Cleaning and pre-treatment of the mechanically processed surfaces can be obtained using laser surface activation as shown in [74]. The oxidation of fibres due to the surface activation improved the wetting and bonding between fibres and adhesive, which led to a full restoration of the tensile strength of the part [74].

### *3.3 Image processing based detection of the fibre orientation during depth-controlled laser ablation of CFRP monitored by optical coherence tomography* 113

A certifiable and cost-effective repairing process for aeronautical applications requires a robust, reliable and repeatable bonded repair technology [92]. One promising approach for an automated repair process of damaged parts is the laser-based removal of the damaged area in a stepped geometry [93,94] and laser surface treatment of the interface between original plies and repair plies [74], followed by a rebuilding process using repair plies that precisely fit into the removed area [93]. For this approach to work, layer-accurate laser ablation is necessary to maintain the structural strength of the repaired part, which means that the ablation should always stop at the interface between two layers and not somewhere within one ply. This requirement is hardly achievable with conventional laser ablation, as the direction-dependent thermal properties of composites lead to inhomogeneous material removal with depth deviations up to 30% of the average ablated depth [77]. Furthermore, damaging the underlying ply must be avoided during the removal of damaged layers as it results in a reduced adhesion of the repair plies and thus reduced bonding strength [94].

Layer-accurate laser ablation can be achieved using optical coherence tomography (OCT) for inline depth control as it is already established in medical applications such as laser ablation of bone [13] and tooth [199] and mechanical engineering, e.g. surface post-processing of additively-manufactured parts [153] or laser beam welding of aluminium [200]. An OCT-based depth measurement system in combination with a Galvanometer-scanner can be used to measure the surface topography of a scanned sample [201] and detect the sample's position and orientation within a processing station to guarantee reproducible and accurate process conditions, e.g. during a laser-based decoating process on free-form surfaces [189]. The authors of the present work have already reported on a depth-controlled ablation process in previous publications [187,188] in which a superordinated control system used the data of the OCT-based depth measurement to determine locations in the processing area that have not reached the target depth and still need to be processed. In comparison to conventional ablation without depth control, this allowed the reduction of the resulting surface roughness and therefore an improved surface quality when processing CFRP [187,188]. However, depth-controlled ablation alone cannot ensure the required layer-accurate ablation that is necessary for the repairing process. Due to manufacturing-related variations of the layer thicknesses, the appropriate target depth for the controlled ablation process of each layer is usually not known in advance. This issue can be solved when the fibre orientation of the layer that is being ablated can

be monitored. Then, a change of the fibre orientation indicates a transition from one layer to the next. With this the ablation can locally be stopped exactly at the interface between two layers. To this end, however, the fibre orientation must be detected during the ablation process to be able to detect the transition from one layer to the next. It is worth noting that the knowledge about the orientation of the fibres additionally allows for the implementation of specific CFRP processing strategies to significantly increase the surface quality in laser surface treatment of fabric laminate [202] and enhance the ablation rate when processing multidirectional laminate [203].

In the following we present a holistic laser-based approach for automated and layer-accurate removal of damaged areas in parts made from CFRP as preparation for repairing. Section 2 will focus on the experimental setup and processing strategy for the depth-controlled laser ablation process monitored by OCT and requirements and limits for automated manufacturing of ablation geometries with minimum damage, high shape accuracy and low roughness. The use of the OCT-based measurement of the surface topography generated during the depth-controlled ablation process and the image processing to determine the fibre orientation and thus the processed layer is described and validated in section 3. Finally, the proposed method is used to demonstrate layer-accurate stepped laser ablation of a multidirectional laminate CFRP part in section 4. The suitability of the presented approach for damage removal as preparation for repairing is proven by cross-sections and scanning-electron-microscopy.

## 2 Controlled laser ablation of CFRP with minimum damage for automated manufacturing of precise geometries

### 2.1 Material and experimental setup

The investigated CFRP samples were laminates manufactured by vacuum-assisted resin infusion (VARI). The multidirectional laminates (*CM-Preg T UD*) used were carbon fibres in an epoxy matrix (*CP003*) with 200 g/m<sup>2</sup> and a tensile strength (0°) of 1,900 MPa (DIN ISO 527). The volume fraction of carbon fibres in the CFRP laminates was 60%. The carbon fibres were arranged in eight layers of different fibre orientations of 0°, -45°, 45°, 0°, 0°, 45°, -45° and 0° with a total sample thickness of 5.2±0.4 mm. Each layer had a thickness ranging between 500 µm and 1000 µm with

### 3.3 Image processing based detection of the fibre orientation during depth-controlled laser ablation of CFRP monitored by optical coherence tomography 115

variations resulting from the manufacturing process. A matrix layer with a thickness of approximately 50  $\mu\text{m}$  covered layer 1 and layer 8 and was present at the interface between layer 4 and layer 5. The fabric laminates (*CM-Preg F Köper 2/2*) used were carbon fibres in an epoxy matrix (*CP003*) with 245  $\text{g}/\text{m}^2$  and a tensile strength ( $0^\circ$ ) of 1,100 MPa. The volume fraction of carbon fibres in warp direction was 60%. The carbon fibres were arranged in 20 layers of different warp directions of  $0^\circ/90^\circ$  and  $-45^\circ/45^\circ$  with a total sample thickness of  $9.4 \pm 0.1$  mm.

The laser system used for material processing in this study emits pulses at a wavelength of  $\lambda_L = 1047$  nm with a pulse duration of 60 ns and a beam quality factor  $M^2 < 1.3$ . The maximum average output power was 20 W at a pulse repetition rate of  $f_p = 15$  kHz, corresponding to a maximum pulse energy of  $E_p = 1.33$  mJ. The laser beam was circularly polarized and had a Gaussian intensity distribution. The Fourier-domain OCT-based depth measurement system *CHRocodile 2* from *Precitec* was used for optical distance measurements. The superluminescence diode (SLD) of the measurement system is a broadband light source that emits at a central wavelength of 1080 nm with a bandwidth of 40 nm and a beam quality factor of  $M^2 < 1.1$ . The average output power of the SLD was 100 mW and the measuring rate was set to the maximum of 70 kHz. The depth measurement system provided an axial measurement range of approximately 6 mm with an axial measurement accuracy of down to  $\pm 1$   $\mu\text{m}$ . The beam of the processing laser was superposed with the beam of the OCT-based depth measurement system by means of a dichroic mirror as sketched by Figure 3.12.

The dichroic mirror was reflective for the beam of the processing laser at a wavelength of  $\lambda_L = 1047$  nm and transparent for the broadband measurement beam centred at a wavelength of  $\lambda_O = 1080$  nm. The superposed beams were guided into a Galvanometer-scanner system which deflected the beams for fast movement over the sample's surface. An F-Theta lens with a focal length of 163 mm was used to focus the superposed beams on the sample's surface. The resulting beam diameters in the focal plane of this setup were  $d_0 = 45 \pm 5$   $\mu\text{m}$  for the processing laser and  $15 \pm 5$   $\mu\text{m}$  for the measurement beam.

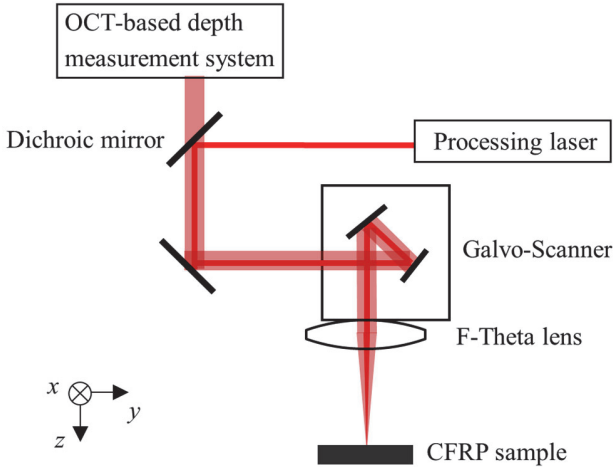


**Figure 3.12** Concept of the OCT-based depth-controlled laser processing setup.

The principle of the OCT-based depth-controlled ablation process is described in [187] and [188]. In brief, the topography of the sample surface is measured using the OCT-based depth measurement system to receive the depth value ( $z$ -direction in Figure 3.12) while the measurement beam is deflected across the sample surface ( $x$ - $y$ -plane in Figure 3.12) in a rasterized manner by the Galvanometer-scanner. After each scan across the sample surface, a 3D-measurement of the surface topography is generated and compared to the desired target topography by the control system. Locations with excess material are processed in the following scan, until the measured topography fits to the target topography within a tolerance of  $\pm 5 \mu\text{m}$ . When contaminants or other measurable surface defects are present on the surface and above the targeted depth, the control system attempts to remove the excess material. A signal-to-noise ratio (SNR) value is assigned to each measured depth value by the OCT-based depth measurement system, which allows to identify measurement errors with low SNR and replace these values, e.g. with the median of adjacent valid depth values. In the experiments, less than 0.1% of the measured depth values had to be replaced this way, due to a sufficiently high signal quality.

## 2.2 Processing strategy for minimum damage and smooth surfaces

The extent of damage in CFRP laser processing is often measured with the matrix evaporation zone (MEZ). The minimum achievable damage depends on the absorbed intensity, which is in the range of  $1 \mu\text{m}$  for an absorbed intensity  $>10^9 \text{ W/cm}^2$  [204]. A maximum absorbed intensity up of  $10^9 \text{ W/cm}^2$  can be achieved with the experimental setup used in this work, due to short laser pulses with a pulse duration of  $60 \text{ ns}$  and maximum pulse energy of  $E_p = 1.33 \text{ mJ}$  focused to a beam diameter of  $d_0 = 45 \mu\text{m}$  and an absorptance for carbon fibres of about  $71\%$  for the laser wavelength of  $\lambda_L = 1047 \text{ nm}$  and for circular polarization [204]. For processing of CFRP with multiple pulses, the extent of the MEZ also depends on the pulse overlap. A low pulse overlap is required during scanned processing of CFRP in order to avoid heat accumulation effects by pulse-to-pulse or scan-to-scan accumulation that result in the formation of a MEZ [205]. The pulse overlap in scanning direction  $\Omega_x$  can be calculated by

$$\Omega_x = 1 - \frac{v_x}{f_p \cdot d_0}, \quad (3.4)$$

where  $v_x$  is the scanning speed,  $f_p$  is the pulse repetition rate and  $d_0$  is the beam diameter. Hence, a low pulse overlap  $\Omega_x$  for a given beam diameter  $d_0$  can be achieved using high scanning speeds  $v_x$  [206] and low pulse repetition rates  $f_p$  [207]. For the experiments, a low pulse overlap in scanning direction of  $\Omega_x = 11\%$  was attained with the given pulse repetition rate of  $f_p = 15 \text{ kHz}$  and beam diameter of  $d_0 = 45 \mu\text{m}$  by using a scanning speed of  $v_x = 600 \text{ mm/s}$ . The pulse overlap perpendicular to the scanning direction  $\Omega_y$  can be calculated by

$$\Omega_y = 1 - \frac{p_x}{d_0}, \quad (3.5)$$

where  $p_y$  denotes the hatching distance. Hence, a low pulse overlap  $\Omega_y$  perpendicular to the scanning direction for a given beam diameter  $d_0$  can be achieved using high hatching distances [208]. In the experiments, a low pulse overlap perpendicular to the scanning direction of  $\Omega_y = -33\%$  was attained with the given beam diameter of  $d_0 = 45 \mu\text{m}$  by using a hatching distance of  $p_y = 60 \mu\text{m}$ .

Areas of  $2 \times 2 \text{ mm}^2$  with a mean ablation depth of  $200 \mu\text{m}$  were ablated with the maximum power of  $20 \text{ W}$ , a pulse repetition rate of  $f_p = 15 \text{ kHz}$ , a scanning speed of  $v_x = 600 \text{ mm/s}$  and a hatching distance of  $p_y = 60 \mu\text{m}$  in order to investigate the extent of the MEZ in multidirectional laminate. Cross-sections of the sidewalls and the bottom of the ablated areas are shown in Figure 3.13 with the MEZ marked in green colour.

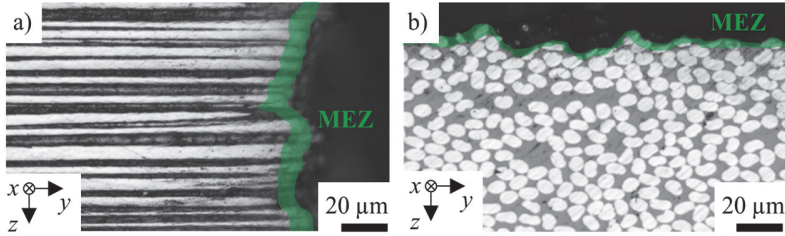


**Figure 3.13** Micrographs of cross-sections of the MEZ marked in green colour a) on the sidewalls and b) at the bottom of the ablated areas.

A MEZ in the range of  $10 \mu\text{m}$  was achieved on the sidewalls (Figure 3.13 a) and a MEZ in the range of  $5 \mu\text{m}$  was achieved at the bottom (Figure 3.13 b) of the ablated areas. Although an intensity  $>10^9 \text{ W/cm}^2$  and low pulse overlaps of  $\Omega_y = 11\%$  and  $\Omega_z = -33\%$  were used, the MEZ is larger than  $1 \mu\text{m}$ . This deviation is presumably caused by the Gaussian intensity distribution, which is not considered in the model for the prediction of the MEZ by [204].

Besides a small  $\text{MEZ} \leq 10 \mu\text{m}$ , high material removal rates are desired for short process times and therefore fast repairing processes. For conventional processing of CFRP, the ablation rate was shown to linearly increase with the peak fluence [77]. The peak fluence  $\phi_0$  is given by

$$\phi_0 = \frac{8 \cdot E_p}{\pi \cdot d_0^2}, \quad (3.6)$$

where  $E_p$  denotes the pulse energy and  $d_0$  denotes the beam diameter. Additionally, an increased deviation of the minimum and maximum ablation depth in relation to the average ablation depth, which can also be represented by the surface roughness, was found in [77] with increasing peak fluence. For depth-controlled ablation with a

target ablation depth of  $250\ \mu\text{m}$ , the influence of the peak fluence with  $f_p = 15\ \text{kHz}$ ,  $v_x = 600\ \text{mm/s}$ ,  $p_y = 60\ \mu\text{m}$  and scanning directions parallel and perpendicular to the fibre orientation is shown in Figure 3.14.

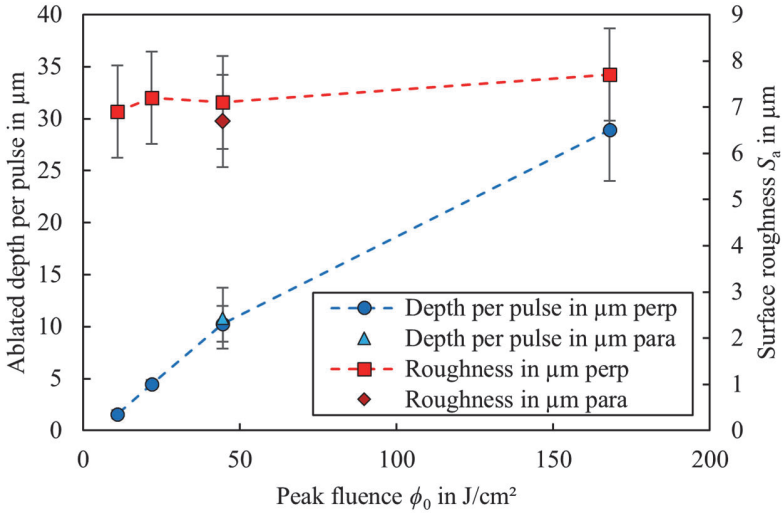


**Figure 3.14** Depth-controlled ablation with peak fluences ranging from  $11\ \text{J}/\text{cm}^2$  to  $168\ \text{J}/\text{cm}^2$ . Ablated depth per pulse for scanning direction perpendicular (blue dots) and parallel (blue triangle) to the fibre orientation. Surface roughness  $S_a$  for scanning direction perpendicular (red squares) and parallel (red diamond) to the fibre orientation.

From peak fluences of  $11\ \text{J}/\text{cm}^2$  to  $168\ \text{J}/\text{cm}^2$ , which corresponds to average powers from  $1.3\ \text{W}$  to  $20\ \text{W}$ , the ablated depth per pulse is increased from  $1.6 \pm 0.4\ \mu\text{m}$  to  $28.9 \pm 4.9\ \mu\text{m}$  (blue dots in Figure 3.14). For comparison, the diameter of a single carbon fibre is typically in the range of  $5$  to  $10\ \mu\text{m}$ . At a peak fluence  $\phi_0 = 45\ \text{J}/\text{cm}^2$ , the ablated depth per pulse is  $10.3 \pm 1.7\ \mu\text{m}$  for scanning perpendicular (blue dot) and  $10.8 \pm 2.9\ \mu\text{m}$  for scanning parallel (blue triangle) to the fibre orientation. Therefore, the scanning direction in relation to the fibre orientation has no significant influence on the ablation rate in depth-controlled ablation. The measured surface roughness  $S_a$  for different scanning directions is also well within the error bars, with  $S_a = 7.1 \pm 1.0\ \mu\text{m}$  for scanning perpendicular (red square) and  $S_a = 6.7 \pm 1.0\ \mu\text{m}$  for scanning parallel (blue triangle) to the fibre orientation. However, in contrast to conventional ablation [77], the resulting surface roughness for depth-controlled ablation remains constant with values in the range of  $S_a = 7 \pm 1\ \mu\text{m}$  for peak fluences of

11 J/cm<sup>2</sup> to 168 J/cm<sup>2</sup>. The highest peak fluence of  $\phi_0 = 168$  J/cm<sup>2</sup>, which corresponds to an average power of 20 W, seems favourable for automated manufacturing of flat geometries with high ablation rates and low surface roughness. No significant influence of the scanning direction on the ablation rate and the resulting surface roughness was observed.

### 2.3 Potentials and limits of depth-controlled ablation

In the following, the depth-controlled ablation is used to demonstrate the potential of automated manufacturing of different geometries in CFRP. A complex geometry consisting of different shapes such as pyramid, half sphere, cone, and steps was set as target geometry for processing of the fabric laminate. The shapes represent different challenges in manufacturing, such as inclined surfaces with different inclination angles, sharp edges, and thin tips. The lateral dimensions of the target geometry were 25 x 25 mm<sup>2</sup> with a maximum height of 5 mm. A photograph of the CFRP fabric laminate sample from oblique view and the corresponding measurement of the surface topography after the depth-controlled ablation process with  $\phi_0 = 168$  J/cm<sup>2</sup>,  $f_p = 15$  kHz,  $v_s = 600$  mm/s and  $p_y = 60$   $\mu$ m is depicted in Figure 3.15.

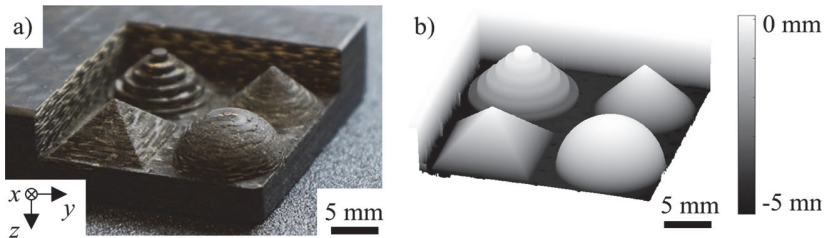


**Figure 3.15** a) Photograph from oblique view and b) OCT-based measurement of the complex target geometry manufactured in fabric laminate CFRP by depth-controlled ablation.

High-quality geometries independent of the targeted shape with the features of each shape well pronounced and a rather smooth surface for an inhomogeneous material such as CFRP can be seen in the photograph in Figure 3.15 a) and the OCT-based measurement in Figure 3.15 b). The latter was used to determine the shape deviation of the manufactured geometries from the targeted shape, as also shown in [153] for additively manufactured aluminium parts. A mean shape deviation of below 50  $\mu$ m

### 3.3 Image processing based detection of the fibre orientation during depth-controlled laser ablation of CFRP monitored by optical coherence tomography 121

was calculated for the complex geometry, which is approximately 1% in relation to the ablated depth of 4.9 mm. The roughness measured on the bottom of the ablated area, a flat geometry in the  $x$ - $y$ -plane, yields  $S_a = 11 \mu\text{m}$ . The increased roughness of the fabric laminate of  $S_a = 11 \mu\text{m}$  in comparison to the roughness of the multidirectional laminate of  $S_a = 7 \pm 1 \mu\text{m}$  is caused by local ablation of matrix clusters between warp and weft, resulting in holes with larger depth than in the adjacent area. The higher mean deviation of  $50 \mu\text{m}$  of the complex geometry compared to the roughness  $S_a = 11 \mu\text{m}$  of the flat geometry results from the inhomogeneous composite structure in  $z$ -direction. In particular, the shape deviations are caused at the transitions of one layer to another, which is clearly visible for the half sphere geometry in Figure 3.15 a). Additionally, shape deviations are present in the stepped geometry on locations with ideally vertical walls, which show a taper angle in the measurement. Nevertheless, steep walls were achieved with an angle of up to  $87.5^\circ$  between the original surface and the bottom of the ablated area in 4.9 mm depth.

In terms of machining space as well as processing quality and processing accuracy, the depth-controlled ablation process is mainly limited by the used experimental setup and resulting process parameters. For the setup of this work, the maximum machining space in the  $x$ - $y$ -plane (cf Figure 3.12) is the scanning field of the Galvanometer-scanner with  $120 \times 120 \text{ mm}^2$ . With a fixed position of the focus plane to the sample surface, the machining space in  $z$ -direction is limited to 6 mm by the axial measurement range of the OCT-based depth measurement system. The SNR of the measured depth values decreases from 400 to 100 with increasing ablation depths up to 5 mm, but remained above the minimum quality threshold of 50. As the extent of the MEZ was  $< 10 \mu\text{m}$  and below the diameter of the OCT measurement beam of  $15 \pm 5 \mu\text{m}$ , no significant influence of the MEZ on the SNR of measured depth values could be detected. The beam diameter of the processing laser is increased from  $45 \mu\text{m}$  on the sample surface to  $183 \mu\text{m}$  in 5 mm ablated depth due to beam divergence. As shown by Eq. (3.4) and Eq. (3.5), an increased beam diameter of  $183 \mu\text{m}$  on the processed sample surface results in increased pulse overlap parallel to the scanning direction from 11% to 78% and increased pulse overlap perpendicular to the scanning direction from -33% to 67%, which in turn can cause an increased MEZ due to heat accumulation effects by pulse-to-pulse or scan-to-scan accumulation [205]. However, a MEZ  $< 10 \mu\text{m}$  was measured even in 5 mm ablated depth, as heat accumulation can be avoided with low pulse repetition rates in the range of  $f_p = 15 \text{ kHz}$  [205]. The processing accuracy, e.g. the minimum feature size that can

be manufactured, is dependent on the beam diameter and the peak fluence  $\phi_0$ . The beam diameter and peak fluence define the minimum feature size in the  $x$ - $y$ -plane, which is approximately  $50\ \mu\text{m}$ . Furthermore, the peak fluence defines the spatial resolution of features in  $z$ -direction with the ablated depth per pulse (cf. Figure 3.14). In future work, the machining space could be increased and the processing quality and processing accuracy maintained for even greater material thicknesses and ablation depths, when the setup described in Figure 3.12 is modified with a 6-axis robot for flexible positioning in the workspace of the robot as demonstrated in [189].

Within the limitations mentioned before, a wedge geometry with an inclination angle of  $24^\circ$  was set as target geometry for processing of the multidirectional laminate to investigate depth-controlled ablation for the automated manufacturing of repair geometries for tapered scarf repair. A micrograph of the cross-section after the ablation process with  $\phi_0 = 168\ \text{J}/\text{cm}^2$ ,  $f_p = 15\ \text{kHz}$ ,  $v_x = 600\ \text{mm}/\text{s}$  and  $p_y = 60\ \mu\text{m}$  is shown in Figure 3.16.

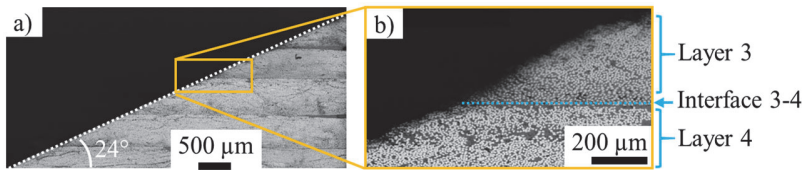


**Figure 3.16** a) Micrograph of the cross-section of a wedge geometry with an inclination angle of  $24^\circ$  marked by a white dotted line manufactured by depth-controlled ablation in the multidirectional laminate CFRP sample. b) The magnified image marked by the yellow frame shows the transition from layer 3 to layer 4.

In inclination angle is marked with the white dotted line in the micrograph and was measured to  $24^\circ$  (Figure 3.16 a), which was also confirmed by evaluation of the OCT-based measurement (not shown here). The mean shape deviation of the surface topography measured by OCT to the targeted wedge geometry yields  $12\ \mu\text{m}$ , which is a sufficiently high shape accuracy for most repairing processes. The magnified image in Figure 3.16 b) shows the transition from layer 3 to layer 4, with the interface of the two layers marked by a blue dotted line. Although there is a change in fibre orientation from  $45^\circ$  in layer 3 to  $0^\circ$  in layer 4, the transition between the two layers remains smooth when using depth-controlled ablation. Hence, depth-controlled ablation is suitable for manufacturing the wedge geometry for tapered scarf repair of CFRP with a defined inclination angle, high shape accuracy and smooth

transitions between adjacent layers. For the manufacturing of stepped repair geometries, the target ablation geometry must be adapted to each step and hence to each layer. However, the targeted ablation depth to achieve layer-accurate ablation is not known in advance, due to manufacturing-related variations of the layer thicknesses. This issue can be solved by detecting the transition between the layers with the determination of the fibre orientation for the currently processed layer as described in the following.

### 3 Determination of fibre orientation for detection of the processed layer

#### 3.1 Principle of the image processing method

The fibre orientation can be determined using the OCT-based measurement of the surface topography that is generated during the depth-controlled ablation process to compare the current topography with the target topography. The measured surface topography for an ablated area of  $1 \times 1 \text{ mm}^2$  with a mean ablation depth of approximately  $250 \mu\text{m}$  and the fibre orientation of the multidirectional laminate marked as a red arrow is shown in Figure 3.17 a).

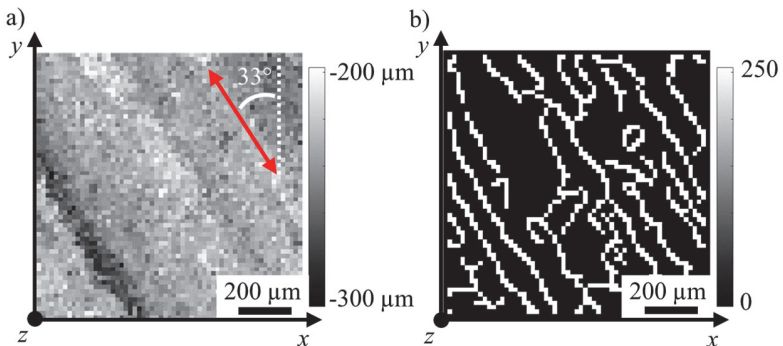


**Figure 3.17** a) Measured surface topography of an ablated area of  $1 \times 1 \text{ mm}^2$  with a mean ablation depth of approximately  $250 \mu\text{m}$  and the fibre orientation marked as a red arrow. b) Result of Canny edge detection applied to the measured surface topography.

As the fibre orientation of the first layer of the multidirectional laminate is  $0^\circ$ , the value of  $33^\circ$  marked by the red arrow in the OCT-based measurement results from a rotation of the sample around the z axis. In a previous work [188] it was shown that the 2D-Fourier transform of the measured surface topography yields certain spatial frequencies only perpendicular to the fibre orientation. These spatial frequencies can be detected in the measurements of the surface from both depth-controlled and conventional ablation and are in the range of 2 /mm to 5 /mm, which corresponds to wavelengths between 200  $\mu\text{m}$  to 500  $\mu\text{m}$ . It can be assumed that the waviness is caused by the fibre rovings that are used in the production process of CFRP and have a diameter of about 200  $\mu\text{m}$  to 700  $\mu\text{m}$  [209]. As the diameter of a single carbon fibre is typically in the range of 5  $\mu\text{m}$  to 10  $\mu\text{m}$  and the focus diameter of the OCT beam is  $15\pm 5$   $\mu\text{m}$ , individual carbon fibres cannot be detected with the setup used. As shown in [188], the 2D-Fourier transform can be used to determine the processed layer of multidirectional laminate. However, this method does not directly yield the value of the angle at which the fibres are orientated and can be corrupted by measurement errors and steep edges in the measurement that cause high-frequency noise. Furthermore, an automated repair process for parts of different materials and different surfaces requires a reliable and validated determination process. Therefore, a new image processing-based approach was investigated and validated for different materials, original surfaces, image sizes and rotation angles. The image processing mainly consists of two steps, image preparation and angle calculation. For the preparation of the image, the Canny edge detection method [210] is used in this work to detect and extract the orientation of the fibre rovings from the measured surface topography. For the calculation of the angles, the Hough transform as presented in [211] or the Radon transform [212] can be applied to the Canny-filtered measurement. Artefacts can occur for angles of  $45^\circ$  or  $-45^\circ$  when using the Hough transform [213], which are values of typical lay-up configurations in CFRP laminates. Hence, only the Radon transform is used in this work to avoid these artefacts. Furthermore, the Radon transform was found to be an effective method to determine the fibre orientation from composites in X-ray absorption measurements [214].

The Canny edge detector is an algorithm consisting of multiple steps to extract edges in an image [215]. To this end, noise that is caused by measurement errors is reduced in a first step by applying a Gaussian filter to the image. In the second step, the derivatives in x and y direction are computed to obtain the distribution of the intensity gradients. In the third step non-maximum suppression is applied to find the

sharpest change of the intensity value for thinning out the edges. In the last step, hysteresis thresholding is used to reduce the probability of streaking and isolated false edge points [215]. Applying the Canny edge detection to the 3D measurement from Figure 3.17 a) yields the binary image with edges marked in white lines shown in Figure 3.17 b).

Subsequently, the Radon transform [212] is applied to determine the angles of the lines present in the Canny filtered image. The Radon transform uses the point line duality to transform a line from the space domain, e.g.  $x$ - $y$ -space (Figure 3.17 b)), into a point in the Radon domain. The lines in the space domain can be described in the normal form by

$$y(x) \cdot \sin(\theta) + x \cdot \cos(\theta) - \beta = 0 , \quad (3.7)$$

with  $x$  being the independent variable of the function  $y(x)$ ,  $\theta$  being the angle of inclination of the normal segment that is perpendicular to the described line and contains the point of origin and  $\beta$  as the length of this normal segment. The resulting image of the Radon transform in the Radom domain yields a  $\theta$ - $\beta$ -Radon space matrix of the lines occurring in the space domain. Figure 3.18 shows the  $\theta$ - $\beta$ -Radon space matrix of the Canny filtered image shown in Figure 3.17 b). The brightness value of a pixel for a specific combination of  $\theta$  and  $\beta$  in the Radom space matrix is a measure for how frequently lines with this combination of  $\theta$  and  $\beta$  are found in the space domain, high brightness values corresponding to a frequent occurrence. In order to assess the angle  $\theta$  of lines that appear comparably often in the space domain, the  $\theta$ - $\beta$ -Radon space has to be searched for the highest brightness values and their corresponding  $\theta$ -values.

The evaluation of the three pixels with the highest brightness values of the example shown in Figure 3.18 yields  $\theta$ -values of  $31^\circ$ ,  $34^\circ$  and  $28^\circ$  in order of decreasing brightness and hence decreasing incidence in the space domain. The angle coordinate  $\theta_1 = 31^\circ$  of the pixel with the highest brightness value deviates only by  $2^\circ$  from the actual orientation of the fibres in the measured surface shown in Figure 3.17 a).

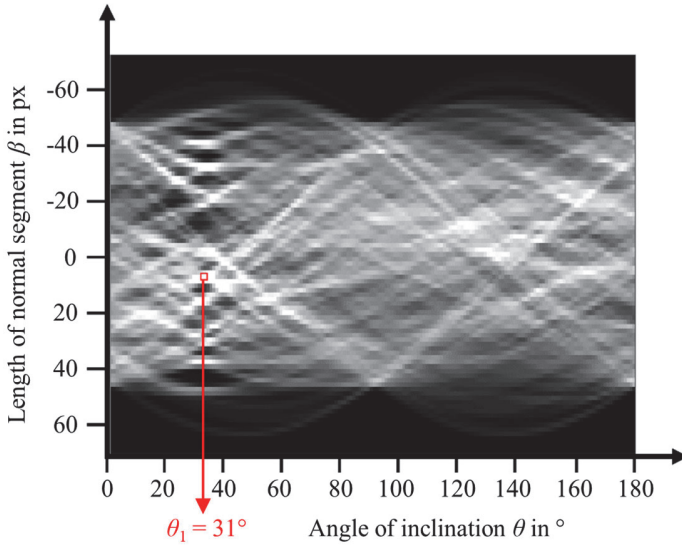


**Figure 3.18** Radon space matrix obtained by applying the Radon transform to the image that was filtered by the Canny edge detection from Figure 3.17. The coordinates of the pixel with the highest brightness value indicate the most frequent combination of  $\theta$  and  $\beta$  of the lines in the space domain and is marked with a red square which yields  $\theta_1 = 31^\circ$  for the analysed image.

### 3.2 Accuracy of the image processing method

The accuracy of the presented method was validated for different rotation angles and measurement field sizes of an ablated area of  $10 \times 10 \text{ mm}^2$  with a mean ablation depth of approximately  $250 \mu\text{m}$ . The sample was positioned on a manual rotation stage that offers a rotation range over  $360^\circ$  around the z-axis and adjustable rotation angle with an accuracy  $< 0.1^\circ$ . The sample was rotated in steps of  $1^\circ$  and measured by the OCT-based depth measurement system in an iterative manner from  $0^\circ$  to  $180^\circ$ . From each measurement of the surface topography, the centred area with a defined field size was used for the determination of the fibre orientation. The measured angle  $\theta_1$  of the pixel with the highest brightness value as a function of the rotation angle for a field size of  $2.0 \times 2.0 \text{ mm}^2$  is depicted in Figure 3.19 a).

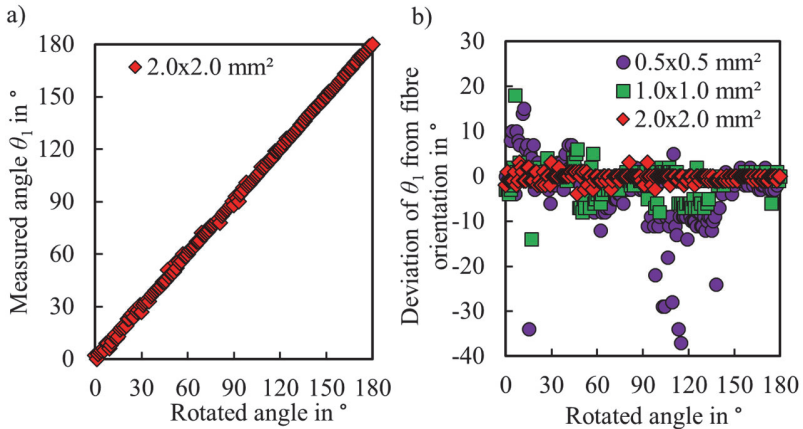


**Figure 3.19** a) Measured angle  $\theta_1$  of the pixel with the highest brightness value as a function of the rotated angle using Canny edge detection and Radon transform of a surface measurement with a field size of  $2.0 \times 2.0 \text{ mm}^2$ . b) Deviation of measured angle  $\theta_1$  from the fibre orientation as a function of the rotation angle for surface measurements with different field sizes of  $0.5 \times 0.5 \text{ mm}^2$  (violet dots),  $1.0 \times 1.0 \text{ mm}^2$  (green squares) and  $2.0 \times 2.0 \text{ mm}^2$  (red diamonds).

The measured angle  $\theta_1$  increases linearly with the rotation angle from  $0^\circ$  to  $180^\circ$  and only small deviations to the linear progression are visible. The deviation of the measured angle  $\theta_1$  to the fibre orientation for different field sizes is shown in Figure 3.19 b). With the field size of  $2.0 \times 2.0 \text{ mm}^2$  (red diamonds), the maximum deviation and root mean square error amount to only  $4^\circ$  and  $1.1^\circ$ , respectively. By decreasing the evaluated field size to  $1.0 \times 1.0 \text{ mm}^2$  (green squares) and  $0.5 \times 0.5 \text{ mm}^2$  (violet dots), the maximum deviation increases to  $18^\circ$  and  $37^\circ$  and the root mean square error increases to  $3.3^\circ$  and  $7.7^\circ$ , respectively. The increasing deviations with decreasing field size result from errors in the determination of the fibre orientation from the fibre rovings. For field sizes of  $1.0 \times 1.0 \text{ mm}^2$  and  $0.5 \times 0.5 \text{ mm}^2$ , the evaluated area for the image processing is in the range of the wavelength of fibre rovings, which seems to be critical in the analysed surface topography for rotation angles in the range of  $0^\circ$  to  $20^\circ$  and  $90^\circ$  to  $140^\circ$ . However, it is only necessary to achieve an angular accuracy and thus a maximum deviation of better than  $\pm 22.5^\circ$  for CFRP parts with fibre orientations of  $0^\circ$ ,  $-45^\circ$ , and  $45^\circ$  to reliably distinguish between two layers of different fibre orientations. Ablation geometries larger than the minimum required

---

field size can be divided into smaller field sizes to locally and precisely detect the fibre orientation with the required accuracy.

### 3.3 Validation for different laminates and surface conditions

The determination of the fibre orientation using the presented method requires at least one scan of material ablation to remove the matrix layer on top of the upper carbon fibre layer and detect the fibre rovings in the surface measurement. However, for precise positioning of the CFRP sample in the processing area and the fibre orientation-dependent scanning strategy for multidirectional laminate described in [203] it is necessary to determine the fibre orientation before the first scan of material ablation. In this case, the sewing threads that are often used for the fixation of the rovings can be measured by OCT as shown in Figure 3.20 a). Two of the sewing threads on the CFRP sample are marked with violet dotted lines to guide the eye. The magnified area (Figure 3.20 b) shows a section of the sewing thread on the sample with a violet dotted line fitted into the image to overlap the present sewing thread. The angle of the violet dotted line is rotated  $68^\circ$  with respect to the orientation of the fibres of the first layer which is marked with a red arrow.

Application of the image processing method introduced before yields an angle of  $\theta_1 = 68^\circ$ . This value is perfectly consistent with the rotation determined by fitting the violet dotted line onto the sewing thread detected in the OCT-based measurement, hence proving the capability of the presented method for precise determination of the fibre orientation of non-ablated parts. If no sewing threads are present but the location and extent of the damaged area have been detected, e.g. with X-ray tomography as mentioned in the introduction, and the damaged part is accordingly positioned below the Galvanometer-scanner in the processing area, one scan of laser ablation is typically sufficient to remove the matrix layer on the surface and expose the fibre rovings of the first layer. Then, the fibre orientation can again be determined from the waviness caused by the fibre rovings.

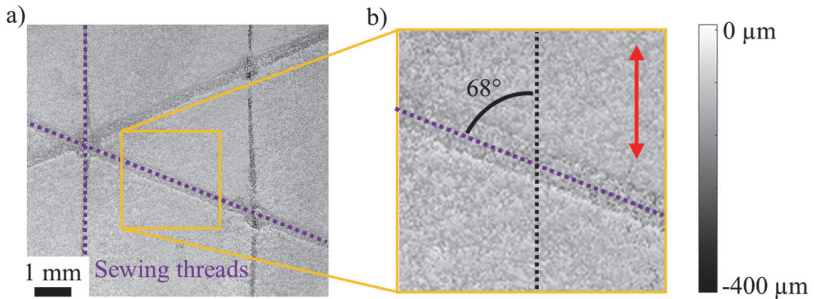


**Figure 3.20** OCT-based measurement of a) a non-ablated CFRP sample with two of the sewing threads marked with violet dashed lines and b) a magnified area of the non-ablated CFRP sample and a sewing thread which is rotated by  $68^\circ$  to the fibre orientation of the first fibre layer. The fibre orientation is marked with a red arrow.

The method can also be applied to determine the fibre orientation during processing of fabric laminate. The measured surface topography of the complex geometry shown in Figure 3.15 was used for image processing and determination of the fibre orientation. The central area of the complex target geometry with a field size of  $3 \times 3 \text{ mm}^2$  in approximately 4.9 mm ablated depth is shown in Figure 3.21 a). Two different fibre orientations are present in the image,  $45^\circ$  and  $135^\circ$ , each marked with a red arrow. The orientation of  $135^\circ$  corresponds to  $-45^\circ$  in typical lay-up denotation. Application of Canny edge detection and Radon transform yields Figure 3.21 b). In this case, the five pixels with the highest brightness values in Figure 3.21 b) were analysed in order to gain knowledge about multiple fibre orientations in the space domain (Figure 3.21 a).

The evaluation of the five pixels with the highest brightness values yields  $\theta$ -values of  $\theta_1 = 50^\circ$ ,  $\theta_2 = 47^\circ$ ,  $\theta_3 = 129^\circ$ ,  $\theta_4 = 53^\circ$  and  $\theta_5 = 136^\circ$ , listed in order of decreasing brightness and hence decreasing incidence in the space domain. With deviations of  $<10^\circ$ ,  $\theta_1$ ,  $\theta_2$  and  $\theta_4$  are in good agreement with the fibre orientation of  $45^\circ$  and  $\theta_3$  and  $\theta_5$  correspond well with the fibre orientation of  $135^\circ$  (or  $-45^\circ$ ). If a distinct result with only one dominant angle in the evaluated image is required, the image size can be reduced to  $1.0 \times 1.0 \text{ mm}^2$  as shown in Figure 3.19 b). The lower limit of the image size is given by the diameter of the fibre rovings.

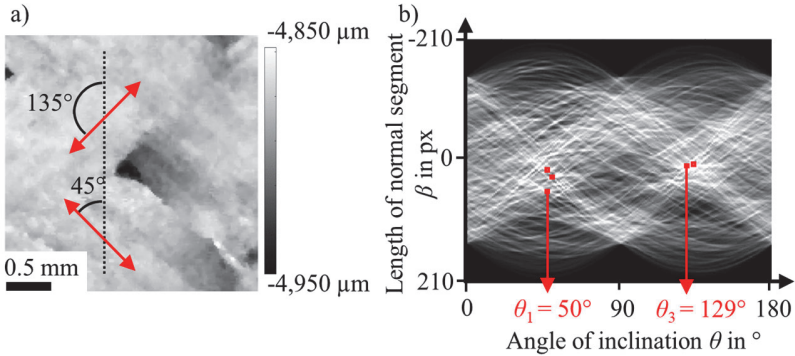


**Figure 3.21** OCT-based measurement of the central area of the complex target geometry shown in Figure 3.15 b) with a field size of  $3 \times 3 \text{ mm}^2$  and the fibre orientations marked with red arrows. b) Radon space matrix obtained by applying the Radon transform after filtering a) by the Canny edge detection. The five pixels with the highest brightness are marked with red squares and yield angles of  $\theta_1 = 50^\circ$ ,  $\theta_2 = 47^\circ$ ,  $\theta_3 = 129^\circ$ ,  $\theta_4 = 53^\circ$  and  $\theta_5 = 136^\circ$ , listed in order of decreasing incidence in the space domain.

## 4 Layer-accurate laser ablation for stepped repair geometries

### 4.1 Manufacturing of demonstration part

Finally, depth-controlled ablation in combination with the determination of the fibre orientation was used to achieve layer-accurate laser ablation of a complex ablation geometry on two sides of a multidirectional laminate CFRP demonstration part. One side of the targeted ablation geometry is shown in Figure 3.22 a) with the fibre layers numbered according to their position from the top (1) to the bottom (8) side of the workpiece. Each greyscale represents a different fibre layer and hence a different targeted ablation depth. The ablation geometry is mirrored on the drawn black line for the other side of the CFRP part. In contrast to circular scarfing, this ablation geometry minimizes the ablated volume while maintaining a high bonding strength of the repair plies after the rebuilding process. After positioning, the CFRP part was ablated using depth-controlled ablation with  $\phi_0 = 168 \text{ J/cm}^2$ ,  $f_p = 15 \text{ kHz}$ ,  $v_x = 600 \text{ mm/s}$  and  $p_y = 60 \text{ μm}$  and the targeted geometry shown in Figure 3.22 a). Every  $50 \text{ μm}$  ablated depth, the controlled ablation algorithm was paused in order to

### 3.3 Image processing based detection of the fibre orientation during depth-controlled laser ablation of CFRP monitored by optical coherence tomography 131

determine the fibre orientation with a measurement field size of  $1 \times 1 \text{ mm}^2$ . Whenever a transition from one layer to the next was detected due to a change of the fibre orientation, the ablation process was stopped, and the ablation geometry was adjusted to the assigned geometry of the respective fibre layer. A camera image after processing all layers of one side of the CFRP part can be seen in Figure 3.22 b).

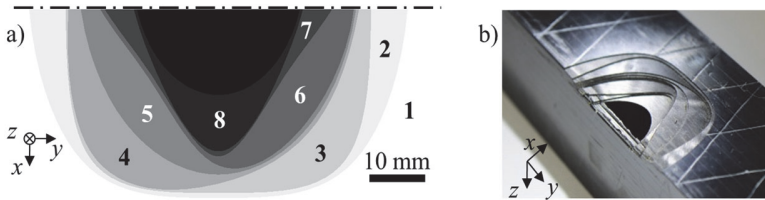


**Figure 3.22** a) Targeted ablation geometry for one side of the CFRP part with each greyscale representing a different fibre layer and numbered according to their order in the workpiece. b) Photograph of the layer-accurate ablated geometry on one side of the CFRP part.

The light reflecting surface in the camera image indicates a smooth surface with a comparably low roughness. This is confirmed by the measured surface roughness for the different layers. The achieved surface roughness  $S_a$  is in the range of 8 to  $13 \mu\text{m}$ , even in an ablated depth of about 4.7 mm. The low roughness provides a bonding surface for the repair plies without large gaps between part and repair ply. The layer thickness varies between 461 and  $1008 \mu\text{m}$  which demonstrates again the necessity to detect a change of layers during the ablation process for layer accurate laser ablation. The deviation of the detected fibre orientation from its real value was less than  $\pm 10^\circ$ , which enabled a reliable determination of the fibre layers in the case of repairing of CFRP parts with orientations of the fibres of  $0^\circ$ ,  $-45^\circ$  or  $45^\circ$ . The transition between layer 4 and layer 5 could not be detected by a change of fibre orientation, as both have the same fibre orientation of  $0^\circ$ . However, the matrix layer of  $50 \mu\text{m}$  in between these layers was ablated within one scan and led to a significantly increased ablation rate and thus significant change of ablated depth, which was detected by the control system.

After processing the first side, the CFRP part was manually rotated  $90^\circ$  to ablate the mirrored image of the ablation geometry shown in Figure 3.22 a) onto the second side of the part. The measurement of the surface topography as shown in section 2

and detection of sewing threads as presented in section 3 allowed for precise positioning of the part after the manual rotation. The final result of layer-accurate laser ablated CFRP part can be seen from the top view in the camera image in Figure 3.23.

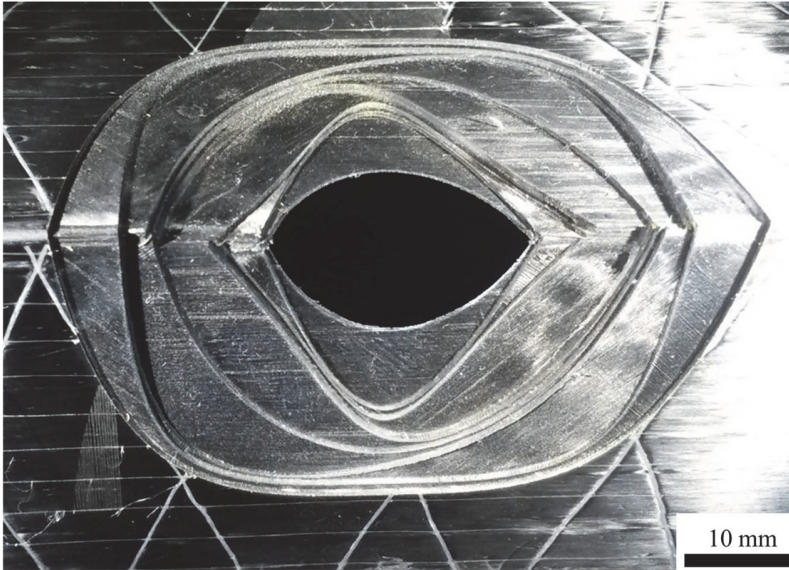


**Figure 3.23** Photograph (top view) of the layer-accurate ablated geometry on both sides of the CFRP part as preparation for the rebuilding process.

#### 4.2 Layer-accuracy and surface structure

A cross-section was prepared to investigate the precision of the controlled ablation process with regard to layer-accuracy. The micrograph of the cross-section from layer 5 to layer 7 is shown in Figure 3.24. The layers are labelled accordingly and the interfaces between the layers are marked with blue dotted lines.

The depth-controlled ablation process allowed for homogeneous material removal and manufacturing of plane steps, which are required in the rebuilding process for fitting the repair plies into the removed area. The surface of each step is approximately 50  $\mu\text{m}$  below the interface of the related layers, as the fibre orientation was determined in an interval of 50  $\mu\text{m}$  ablated depth, which corresponds to two scans of

### 3.3 Image processing based detection of the fibre orientation during depth-controlled laser ablation of CFRP monitored by optical coherence tomography 133

laser processing. The fibre orientation must be calculated in shorter intervals if higher layer-accuracy is required. Higher layer-accuracy can be achieved, for example, by the determination of the fibre orientation after every scan and reduction of the peak fluence for a reduced ablated depth per pulse (cf. Figure 3.14) when the currently ablated layer is almost removed and the ablated depth is close to the estimated transition from one layer to the next.

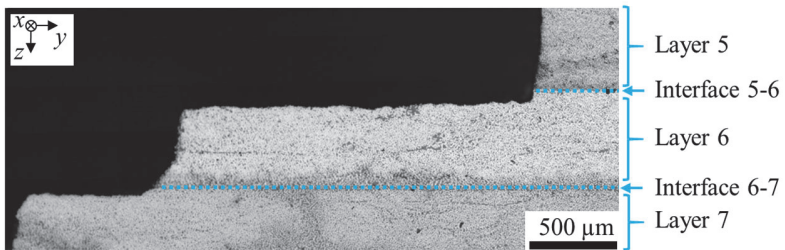


**Figure 3.24** Micrograph of the cross-section of the ablated multidirectional laminate CFRP part in the range of layer 5 to layer 7.

With regard to a later repair process, the surface of each layer was investigated using a scanning-electron-microscope (SEM) after sputtering the part with a thin gold layer. The SEM images of the surfaces from different layers are depicted in Figure 3.25. Independent of the fibre orientation and ablated depth the surfaces of the different layers show stripped fibres with the lower half being embedded in the matrix and the upper half of the fibres being exposed to the ambient atmosphere. Some of the fibres were partially ablated and are either still embedded in the underlying matrix (Figure 3.25 c) or stick to the surface as a fractured fibre fragment (Figure 3.25 b)). Matrix clusters were also observed locally on the surface (Figure 3.25 b)). The fibre thinning at the exposed ends of partially ablated fibres indicates local oxidation. Oxidation occurs when the temperature of the fibres exceeds 400°C and oxygen is present in the atmosphere [216]. Both criteria were fulfilled during the experiments of this work, due to laser processing in ambient atmosphere with laser-based material removal. In [74], a surface with partially ablated and oxidised fibres was obtained after laser surface activation with similar laser parameters (pulse duration 100 ns, pulse repetition rate  $f_p = 20$  kHz, pulse energy  $E_p = 2.5$  mJ and beam diameter  $d_0 = 75$  μm). The activated surface improved the wetting of the

fibres with the adhesive in the subsequent rebuilding process with the repair plies and led to a full restoration of the tensile strength [74]. A similar mechanical behaviour after the repairing process is expected for the CFRP demonstration part manufactured by layer-accurate laser ablation, due to the partially ablated and oxidised fibres.

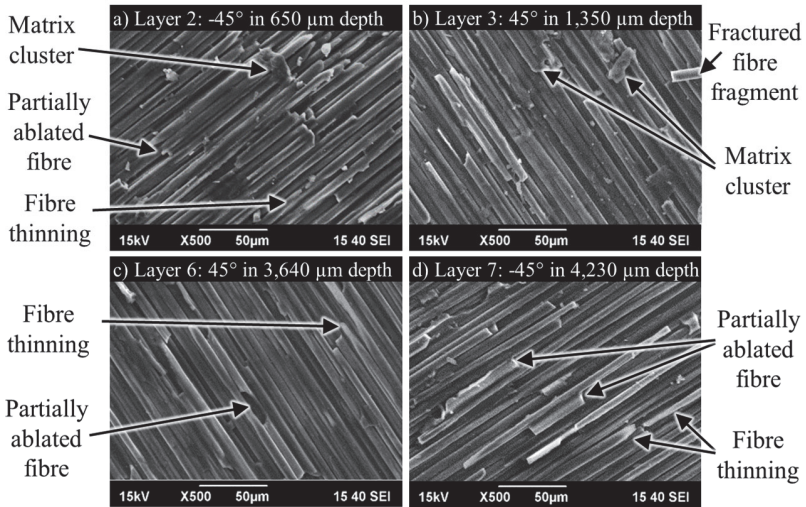


**Figure 3.25** SEM images of resulting layer surface from layer-accurate laser ablation of the CFRP demonstration part shown in Figure 3.24. a) Layer 2 with  $-45^\circ$  fibre orientation in  $650\ \mu\text{m}$  ablated depth. b) Layer 3 with  $45^\circ$  fibre orientation in  $1,350\ \mu\text{m}$  ablated depth. c) Layer 6 with  $45^\circ$  fibre orientation in  $3,640\ \mu\text{m}$  ablated depth. d) Layer 7 with  $-45^\circ$  fibre orientation in  $4,230\ \mu\text{m}$  ablated depth.

The approach of this work with an image processing-based detection of the fibre orientation during depth-controlled laser ablation monitored by OCT allows for automated and layer-accurate damage removal as a preparation for repairing of CFRP parts. The technique is suitable for CFRP parts of multidirectional laminate or fabric laminate with dimensions from few hundreds of millimetres up to several meters with appropriate systems engineering for processing and positioning of large parts.

## **5 Conclusion**

In summary, we have presented a novel method based on processing of images of the surface generated during depth-controlled laser ablation that can be used to determine the fibre orientation during the processing of CFRP in order to achieve layer-accurate laser ablation.

Depth-controlled nanosecond-laser ablation monitored by optical coherence tomography (OCT) was used for automated manufacturing of complex geometries with minimum damage. High shape accuracy with a mean deviation below 50  $\mu\text{m}$  (about 1% of the maximum ablated depth) and a low roughness  $S_a$  in the range of 7  $\mu\text{m}$  to 13  $\mu\text{m}$  was achieved with depth-controlled ablation for different geometries in multidirectional laminate and fabric laminate. The extent of the matrix evaporation zone (MEZ) was measured to  $<10 \mu\text{m}$  with the laser processing strategy of high intensity and low pulse overlap.

The Canny edge detection method followed by the Radon transform was applied to the images of the surfaces in order to extract the orientation of the fibre rovings of the currently processed layer. With this approach the fibre orientation of multidirectional laminate and fabric laminate could be reliably detected for different angles with an angular accuracy better than  $\pm 4^\circ$  when the analysed image size was larger than the diameter of the fibre rovings, e.g. 2.0 x 2.0 mm<sup>2</sup>. Furthermore, the orientation of the sewing threads that are often used for the fixation of the rovings can be detected for a precise positioning of the unprocessed part before depth-controlled ablation.

The effectiveness of the presented approach was confirmed by the successful layer-accurate ablation of a CFRP demonstration part with a stepped repair geometry and different fibre orientations of 0°, -45° and 45°. The investigation of the surface with SEM revealed partially ablated and oxidised fibres on each layer independent of fibre orientation and ablated depth, which was previously found to be beneficial to achieve high tensile strength of the part after the repairing process [74].

The presented approach is a promising technique for automated and layer-accurate damage removal of damaged parts with dimensions from few hundreds of millimetres up to several meters as a preparation for repairing. For the implementation of the

approach in an environment of automated repairing of structural components for aeronautical applications, further optimization with regard to processing and calculation times is required. Regarding a later repair process, the 3D-measurements generated during the removal of the damaged areas are also suitable for the design of the repair plies. The 3D-measurements provide accurate information on the required dimensions of the repair ply for each layer, enabling the manufacturing of repair plies that perfectly fit into the removed area.

### **Acknowledgements**

This work was supported by the German Federal Ministry of Education and Research (grant number 13N12922).

## **4 Scaling the throughput of high-quality laser milling with a 1 kW sub-picosecond laser**

Section 1.4.2 described the need for research in developing and demonstrating a machining strategy for laser milling of silicon and metals using an ultrafast laser with an average power exceeding 1 kW to achieve material removal rates in the order of 100 mm<sup>3</sup>/min. Section 4.1 describes the processing strategy used for the demonstration of high-quality, high-throughput laser milling of silicon up to a depth of several hundred micrometres. Additional results with regard to laser milling of high-quality geometries in metals with high material removal rates are demonstrated in section 4.2.

### **4.1 High-quality high-throughput silicon laser milling using a 1 kW sub-picosecond laser**

This section contains a reproduction of the published article [180]. Changes to text, symbols, equations, figures and numbering of references have been made solely for unification and consistency in this thesis. No changes have been made to the content.

Journal: Optics Letters

Date of publication: 14.01.2021

DOI: <https://doi.org/10.1364/OL.411412>

Copyright: © 2021 Optica Publishing Group.

Daniel Holder<sup>1</sup>, Rudolf Weber<sup>1</sup>, Christoph Röcker<sup>1</sup>, Gerhard Kunz<sup>2</sup>, David Bruneel<sup>3</sup>, Martin Delaigue<sup>4</sup>, Thomas Graf<sup>1</sup>, and Marwan Abdou Ahmed<sup>1</sup>

<sup>1</sup>*Institut für Strahlwerkzeuge (IFSW), University of Stuttgart, Pfaffenwaldring 43, 70569 Stuttgart, Germany*

<sup>2</sup>*Robert Bosch GmbH, Robert Bosch Campus 1, 71272 Renningen, Germany*

<sup>3</sup>*Lasea, Rue des Chasseurs Ardennais 10, 4031 Angleur, Belgium*

<sup>4</sup>*Amplitude Systemes, 11, Avenue de Canteranne, 33600 Pessac, France*

We report on high-quality high-throughput laser milling of silicon with a sub-ps laser delivering more than 1 kW of average laser power on the workpiece. In order to avoid heat accumulation effects, the processing strategy for high-quality laser milling was adapted to the available average power by using five-pulse bursts, a large beam diameter of 372  $\mu\text{m}$  to limit the peak fluence per pulse to approximately 0.7 J/cm<sup>2</sup>, and a high feed rate of 24 m/s. As a result, smooth surfaces with a low roughness of  $S_a \leq 0.6 \mu\text{m}$  were achieved up to the investigated milling depth of 313  $\mu\text{m}$  while maintaining a high material removal rate of 230 mm<sup>3</sup>/min.

Laser processing with ultrafast lasers is a significantly growing field which offers high flexibility for advanced materials processing [7]. Recently, laser milling of silicon has gained widespread attention for applications such as dry etching of micro-electro-mechanical systems (MEMS) [217] and manufacturing of optics for THz radiation [10,218]. Most applications require high surface quality with a low roughness of  $S_a < 1 \mu\text{m}$  and the absence of surface defects, e.g. to achieve low scattering and hence high transmission in optics for THz radiation [100].

The surface quality obtained from laser milling of silicon with ultrashort laser pulses depends on various processing parameters. The applied fluence defines the resulting surface morphology on silicon, which can range from wavelength-sized laser-induced periodic surface structures (LIPSS) for low fluences to several micrometer large cones [102,103] and holes [111] as well as nanoscale solidification cracks on the silicon surface [105] for high fluences with single pulses. For equal fluence, pulse bursts can lead to smoother surfaces without holes in comparison to single pulses

[111]. The surface morphology is also affected by the ambient environment. For instance, the formation of sharp spikes can be reduced using vacuum, N<sub>2</sub> or He [102]. Another processing parameter affecting the resulting surface morphology is the scanning speed. With decreasing scanning speed, a transition from a smooth reflecting surface to a bumpy dark surface was observed for processed metal surfaces [39]. The bumpy surface at lower scanning speeds is caused by higher surface temperatures due to heat accumulation of consecutive pulses [38,39]. Multiple scans over the processing area increase the milled depth, but also result in a coarser surface morphology [103], which typically corresponds to higher surface roughness values [10,39,103,111].

In addition to high surface quality, a high ablation efficiency is desired in order to achieve the maximum throughput with the available laser power. For laser milling, the ablation efficiency is often defined as the energy-specific volume and the throughput is defined as the material removal rate. As shown in [108,111], pulse bursts can significantly increase the energy-specific volume of laser milling of silicon. The maximum attainable efficiency increases with increasing number of pulses per burst, however, accompanied by an increase of the surface roughness [108]. A trade-off for high quality and high efficiency silicon laser milling is to use five to eight pulses in burst in combination with a fluence at or slightly below the optimum fluence of maximum energy-specific volume. A roughness of  $S_a = 0.5 \mu\text{m}$  and an energy-specific volume of  $\Delta V_E = 4.1 \mu\text{m}^3/\mu\text{J}$  was achieved with a five-pulse burst and a peak fluence per pulse of  $1.5 \text{ J/cm}^2$  as reported in [111]. According to [108], eight pulses per burst and a peak fluence of  $0.7 \text{ J/cm}^2$  per pulse resulted in a similar roughness of  $S_a = 0.6 \mu\text{m}$ , but with a significantly higher energy-specific volume of  $\Delta V_E = 4.9 \mu\text{m}^3/\mu\text{J}$ . However, the throughput was rather low, with material removal rates of  $\dot{V} = 0.52 \text{ mm}^3/\text{min}$  and  $\dot{V} = 0.23 \text{ mm}^3/\text{min}$ , due to the low average laser power of 2.1 W and 0.9 W, respectively. Higher material removal rates of up to  $\dot{V} = 20 \text{ mm}^3/\text{min}$  have been demonstrated for silicon laser milling with up to 50 W of average laser power, but without further characterizing the surface roughness [132]. In the past, the average laser power limited the achievable throughput of ultrafast laser processes. With the upscaling of ultrafast lasers to powers exceeding 1 kW, high throughput has been made possible in many applications [219], such as multi-pass cutting of carbon fiber-reinforced plastics [220], surface functionalization of steel [221] or single-pass cleaving of glass [222].

Here, we report on high-quality high-throughput laser milling of silicon with a sub-ps laser with more than 1 kW of average power, which – to the best of our knowledge – is the first demonstration of material processing with sub-ps laser pulses at this power level.

A home-built ultrafast laser emitting pulses at a wavelength of  $\lambda_L = 1030$  nm with a pulse duration of  $\tau_p < 600$  fs was used for the experiments and is presented in detail in [223]. The ultrafast laser delivered a maximum average power of  $P = 1110$  W with a beam quality factor of  $M^2 < 1.5$ . The linearly polarized laser beam was guided into a processing station (*Lasea, LS 5-1*) for the material processing experiments. The focusing optic (*Scanlab, varioSCAN<sub>de</sub> 40i*) with a focal length of 580 mm was mounted to the Galvanometer-scanner (*Scanlab, intelliSCAN<sub>de</sub> 30*) used for beam deflection. The transmission of the optics within the processing station was measured to be 91%, which results in a maximum average power of  $P = 1010$  W on the work-piece. The laser was operated at a burst repetition rate of  $f_B = 500$  kHz, corresponding to a maximum available total burst energy of  $E_B = 2020$   $\mu$ J. In all experiments presented here, the burst energy was divided evenly over five pulses within the burst ( $N_{ppb} = 5$ ). The temporal intraburst pulse distance was 22.7 ns. The focal diameter was measured to be  $d_0 = 90 \pm 5$   $\mu$ m with the technique presented in [103]. The maximum available scanning speed was  $v_x = 24$  m/s, limited by the dynamics of the Galvanometer-scanner.

The processed samples were single side polished silicon wafers with a diameter of  $100 \pm 0.3$  mm, a thickness of  $1000 \pm 20$   $\mu$ m, and a crystal orientation of  $\langle 100 \rangle$ . The ablation experiments were conducted in ambient air on the polished side by scanning squares of  $5 \times 5$  mm<sup>2</sup> along parallel offset lines with the hatching distance  $p_y$ . The sky-writing mode of the Galvanometer-scanner was used to ensure a constant scanning speed  $v_x$  during scanning of the squares, resulting in a constant offset  $p_x$  between the impact locations of the individual bursts even at high scanning speeds. Multiple scans over the same squares were used to increase the depth of the milled cavities. The processed areas were characterized by means of a 3D-Laser Scanning Microscope (*Keyence, VK-9710-K*). The measured cavity depth  $z_C$  was used to calculate the immanent material removal rate

$$\dot{V} = \frac{P_x \cdot P_y \cdot z_C \cdot f_B}{m}, \quad (4.1)$$

where  $p_x$  and  $p_y$  denote the offset of the impact locations of the bursts on the surface in and perpendicular to the scanning direction, respectively,  $f_B$  denotes the repetition rate and  $m$  denotes the number of scans over the processed area. The material removal rate represents the ablated material volume per unit of time and is typically used to evaluate the throughput of an ablation process, and the definition from Eq. (4.1) only holds as long as the offsets  $p_x$  and  $p_y$  are kept so small to ensure a uniform ablation depth. The energetic efficiency of the ablation process is defined by the ratio of the ablated volume and the irradiated energy and is obtained by

$$\Delta V_E = \frac{\dot{V}}{P}, \quad (4.2)$$

where  $P$  denotes the average laser power.

In a first step, we confirmed the advantageousness of a 5-pulse burst and low peak fluence per pulse of approximately  $\phi_0 = 0.7 \text{ J/cm}^2$ , which were found to be beneficial in laser milling of silicon with regard to ablation efficiency and surface roughness as reported in [108,111], also for the pulse duration and repetition rate of our experimental setup, which significantly differs from the ones in [108,111]. The focal position was set on the sample's surface, corresponding to a beam diameter on the surface of  $d_0 = 90 \text{ }\mu\text{m}$ . The scanning speed of  $v_x = 10 \text{ m/s}$  and the hatching distance  $p_y = 20 \text{ }\mu\text{m}$  led to a burst overlap on the surface of 78% in both directions. The surface structure obtained by processing with  $m = 20$  as measured by scanning electron microscope (SEM, *Jeol JSM-6490LV*) is shown in Figure 4.1. The surface is partially covered with LIPSS and nanoparticles. The period of the LIPSS was measured to  $1040 \pm 40 \text{ nm}$ , which is close to the wavelength  $\lambda_L = 1030 \text{ nm}$  of the irradiating laser beam and consistent with observations made in [102]. The nanoparticles detected on the surface vary in diameter from approximately 90 nm to 900 nm. The used parameters were suitable to avoid the formation of surface damages such as nanocracks or melt droplets larger than 1  $\mu\text{m}$  in diameter. The impression of the smooth surface shown in Figure 4.1 was confirmed by the low surface roughness which was measured to be  $S_a = 0.5 \text{ }\mu\text{m}$ . This value is in good agreement with the values published in [108] and [111]. The energy-specific volume was measured to  $\Delta V_E = 3.1 \text{ }\mu\text{m}^3/\mu\text{J}$ , which corresponds to a material removal rate of  $\dot{V} = 10.6 \text{ mm}^3/\text{min}$  at an average power of  $P = 57 \text{ W}$ .

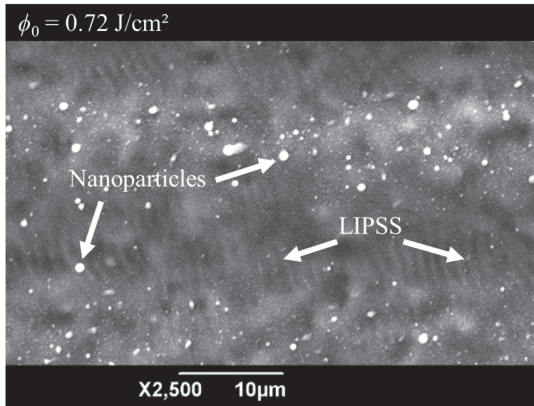


**Figure 4.1** SEM image of laser-milled surface. Process parameters:  $\lambda_L = 1030 \text{ nm}$ ,  $P = 57 \text{ W}$ ,  $f_B = 500 \text{ kHz}$ ,  $E_B = 114 \mu\text{J}$ ,  $N_{\text{ppb}} = 5$ ,  $d_0 = 90 \mu\text{m}$ ,  $\phi_0 = 0.72 \text{ J/cm}^2$ ,  $v_x = 10 \text{ m/s}$ ,  $p_y = 20 \mu\text{m}$ ,  $m = 20$ .

In a second step, the average laser power was increased from  $P = 57 \text{ W}$  to  $P = 950 \text{ W}$ , which leads to an increase of the burst energy from  $E_B = 114 \mu\text{J}$  to  $E_B = 1900 \mu\text{J}$ . By shifting the focus position of the laser beam 17 mm (corresponding to approximately 4 Rayleigh lengths) below the sample surface, the beam diameter on the sample surface was increased from  $d_0 = 90 \mu\text{m}$  to  $d = 372 \mu\text{m}$  to maintain a moderate peak fluence of  $\phi_0 = 0.70 \text{ J/cm}^2$  at the high burst energy of  $E_B = 1900 \mu\text{J}$ . As the surface temperature of the sample determines the formed surface structure, the increased amount of heat at this increased average power requires an adapted scanning speed, which was shown to be a critical parameter affecting the accumulated heat on the surface [39]. The influence of the scanning speed on the resulting surface structure and roughness for laser milling of silicon at the high average power of  $P = 950 \text{ W}$  is shown in Figure 4.2.

The number of scans  $m$  were adapted with respect to the scanning speed  $v_x$  so that the incident number of pulses and hence the total incident laser energy per unit area remains constant for all investigated data points. With the large beam diameter of  $d = 372 \mu\text{m}$  required to keep the fluence at the desired value, the roughness obtained at a scanning speed of  $v_x = 10 \text{ m/s}$  amounts to  $S_a = 3.6 \mu\text{m}$  which is significantly

higher than the one obtained in the aforementioned experiments with  $P = 57$  W. At this low scanning speed the elevated surface temperature caused by the high average power of 950 W led to the formation of melt, which resulted in a solidified melt film and nanoscale solidification cracks, as shown in Figure 4.2 b).

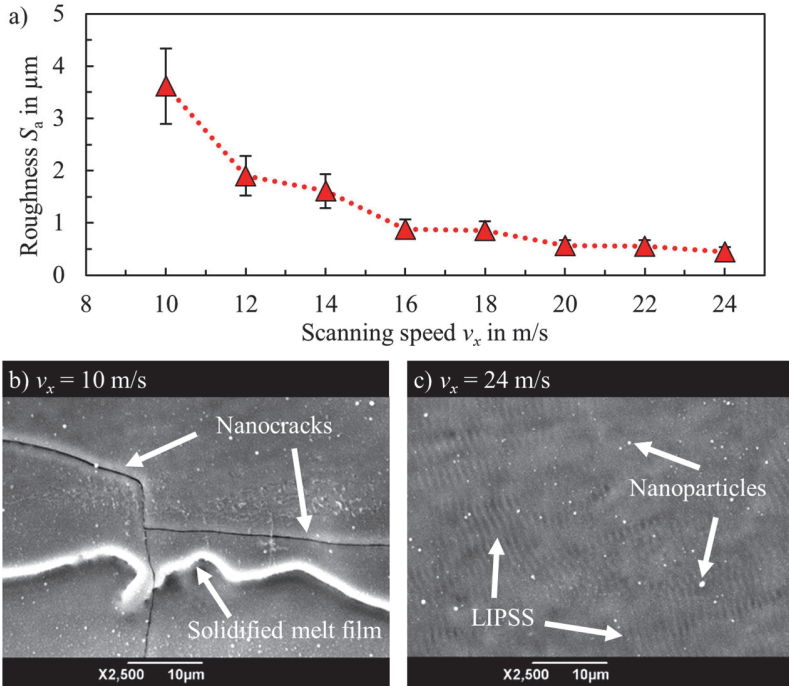


**Figure 4.2** a) Mean roughness of the processed surfaces as a function of the scanning speed with adapted number of scans to keep the total incident energy per unit area at a constant value of  $19 \text{ J/mm}^2$ . Error bars represent measurement uncertainties of  $\pm 20\%$ . SEM images of corresponding surfaces at b)  $v_x = 10$  m/s and c)  $v_x = 24$  m/s. Process parameters:  $\lambda_L = 1030 \text{ nm}$ ,  $P = 950 \text{ W}$ ,  $f_b = 500 \text{ kHz}$ ,  $E_B = 1900 \mu\text{J}$ ,  $N_{ppb} = 5$ ,  $d = 372 \mu\text{m}$ ,  $\phi_0 = 0.70 \text{ J/cm}^2$ ,  $p_y = 50 \mu\text{m}$ .

These surface defects were also observed in [105], however for ablation of craters with  $\lambda_L = 355 \text{ nm}$  and  $\tau_p = 20 \text{ ps}$  at a comparably higher peak fluence of  $\phi_0 = 40 \text{ J/cm}^2$  and a much lower pulse repetition rate of 50 Hz. With increasing scanning speed, the roughness decreases up to the lowest achieved value of  $S_a = 0.4 \mu\text{m}$

at the maximum available scanning speed of  $v_x = 24$  m/s. The surface structure obtained with  $v_x = 24$  m/s is shown in Figure 4.2 c). The surface is covered with LIPSS and nanoparticles without larger surface damage. A major transition of the surface quality occurs in the scanning speed range of about 14 m/s to 16 m/s, also referred to as the critical scanning speed [39]. At 14 m/s and below, the roughness was  $S_a > 1 \mu\text{m}$  and the surface was mainly characterized by solidified melt films and nanocracks. As shown in Figure 4.2 b), LIPSS are absent on the sample surface for a scanning speed of  $v_x = 10$  m/s due to the strong melt formation indicated by the solidified melt films. At 16 m/s and above, the roughness was  $S_a < 1 \mu\text{m}$  and the surface was covered only with LIPSS and nanoparticles. No significant changes in the diameter and distribution of nanoparticles were observed on the structured surfaces at the investigated scanning speeds.

The comparison of the results achieved at high power ( $P = 950$  W) and  $v_x = 24$  m/s (cf. Figure 4.2 c) with the results achieved at low power ( $P = 57$  W) and  $v_x = 10$  m/s (cf. Figure 4.1) shows similar surface structure and roughness values with  $S_a = 0.4 \mu\text{m}$  and  $S_a = 0.5 \mu\text{m}$ , respectively. However, at a power of 950 W the material removal rate is increased by a factor of 20 to  $\dot{V} = 216 \text{ mm}^3/\text{min}$ , which corresponds to an energy-specific volume of  $\Delta V_E = 3.8 \mu\text{m}^3/\mu\text{J}$ . The increased energy-specific volume at a similar peak fluence may be caused by defocusing the laser beam in order to increase the beam diameter on the sample surface. As the energy-specific volume is sensitive to the energy distribution on the irradiated surface, defocusing presumably changed the energy distribution of the defocused non-perfect Gaussian beam with the beam quality factor of  $M^2 < 1.5$ . An even higher energy-specific volume of  $\Delta V_E = 9.6 \mu\text{m}^3/\mu\text{J}$  was recently reported in [112] using 1.76-GHz bursts with 100 pulses in the burst, but this caused an increased roughness of  $S_a = 1.5 \mu\text{m}$ . The increased efficiency at the expense of quality with GHz bursts results primarily from a melt-assisted ablation process. For high surface quality with low roughness, a vaporization-dominated ablation process as demonstrated with our approach seems favourable.

The depth of the cavity milled with  $v_x = 24$  m/s and  $m = 24$  was measured to be  $z_c = 72 \mu\text{m}$ . The low roughness and the avoidance of surface defects with diameters larger than  $1 \mu\text{m}$  have to be maintained over a range of the cavity depth from a few microns up to several hundred microns in order to ensure surfaces that are suitable for the manufacturing of devices such as MEMS and THz optics. A simple method

to adjust the cavity depth is the adaption of the number of scans  $m$  over the processed area. The resulting cavity depth and surface roughness using the parameters  $P = 950$  W,  $\phi_0 = 0.70$  J/cm<sup>2</sup> and  $v_x = 24$  m/s for different number of scans are shown in Figure 4.3.

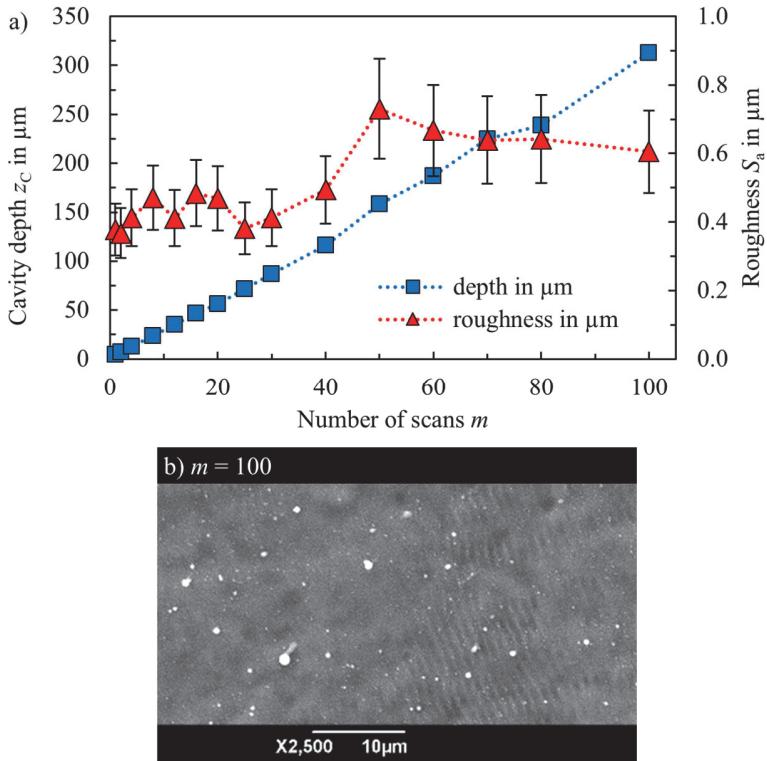


**Figure 4.3** a) Roughness and milled depth as a function of the number of scans. Error bars represent measurement uncertainties of  $\pm 20\%$ . b) SEM image of corresponding surfaces at  $m = 100$ . Process parameters:  $\lambda_L = 1030$  nm,  $P = 950$  W,  $f_B = 500$  kHz,  $E_B = 1900$   $\mu\text{J}$ ,  $N_{ppb} = 5$ ,  $\phi_0 = 0.70$  J/cm<sup>2</sup>,  $d = 372$   $\mu\text{m}$ ,  $v_x = 24$  m/s,  $p_y = 50$   $\mu\text{m}$ .

Two distinct regimes can be identified with respect to the resulting roughness. The first regime with a roughness  $S_a < 0.5$   $\mu\text{m}$  reaches until a maximum of about 40 scans, which corresponds to a cavity depth of  $z_c = 116$   $\mu\text{m}$ . The milled depth per

scan in this first regime is approximately  $3.0 \mu\text{m}$ . The second regime exhibits an increased roughness of  $0.6 \mu\text{m} < S_a < 0.8 \mu\text{m}$  and ranges from 50 to 100 scans up to the maximum investigated cavity depth of  $z_c = 313 \mu\text{m}$ . The milled depth per scan in the second regime is approximately  $3.2 \mu\text{m}$ . A coarser surface structure and increased roughness with an increasing cavity depth was also observed for laser milling of silicon in [103] and [10]. However, in the present work, a low roughness  $S_a < 0.8 \mu\text{m}$  and fine surface structure partially covered with LIPSS could be maintained up to the maximum milled depth of  $313 \mu\text{m}$  (cf. Figure 4.3 b)). Both are required to avoid scattering and achieve maximum transmission when laser ablation is used for the manufacturing of optics for THz radiation.

Finally, we also demonstrated laser milling of a chamfer geometry by applying an average laser power in excess of 1 kW. To the best of our knowledge, this is the first demonstration of laser processing with sub-ps pulse durations and an average power of more than 1 kW. For this experiment, the available average power on the workpiece was increased to  $P = 1010 \text{ W}$  by realignment of the laser system. As the beam diameter was kept constant, the resulting peak fluence on the workpiece was slightly increased to  $\phi_0 = 0.74 \text{ J/cm}^2$ . The chamfer geometry was milled by decreasing the width of one side of the initially squared-shaped scanning area after each scan by  $50 \mu\text{m}$ , which corresponds to one parallel offset line with the hatching distance of  $p_y = 50 \mu\text{m}$ . A LSM measurement (*Olympus, OLS4000*) of the manufactured geometry is shown in Figure 4.4.

The evaluation of the LSM measurements reveal low roughness values, with  $S_a = 0.4 \mu\text{m}$  in the upper area of the chamfer geometry (marked with I in Figure 4.4) and  $S_a = 0.6 \mu\text{m}$  in the lower area of the chamfer geometry (marked with II in Figure 4.4). The surface is again covered with LIPSS and nanoparticles (not shown here). This is consistent with the results obtained for laser milling of the flat surfaces shown in Figure 4.3. Furthermore, the flatness of the tilted surface was investigated by calculation of the peak-to-valley height after filtering the LSM measurement with a cutoff wavelength of  $250 \mu\text{m}$ . The tilted surface is smooth with a low peak-to-valley height of  $5.7 \mu\text{m}$  over the large area of  $3.5 \times 3.5 \text{ mm}^2$ . Although the ablated depth per scan is about  $3 \mu\text{m}$ , no steps were detected along the offset parallel processed lines.

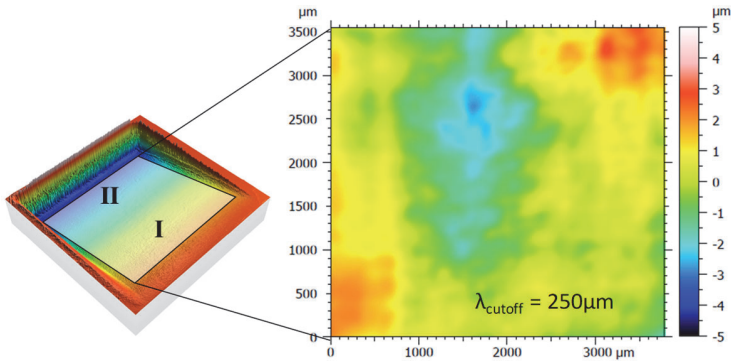


**Figure 4.4** LSM measurement of chamfer milled on the surface of a silicon wafer. Process parameters:  $\lambda_L = 1030$  nm,  $P = 1010$  W,  $f_B = 500$  kHz,  $E_B = 2020$   $\mu$ J,  $N_{ppb} = 5$ ,  $\phi_0 = 0.74$  J/cm<sup>2</sup>,  $d = 372$   $\mu$ m,  $v_x = 24$  m/s,  $p_y = 50$   $\mu$ m,  $m$  was adapted for each scanning vector, up to 100 scans.

The energy-specific volume of  $\Delta V_E = 3.8$   $\mu$ m<sup>3</sup>/ $\mu$ J during laser milling with  $P = 1010$  W corresponds to a high material removal rate of  $\dot{V} = 230$  mm<sup>3</sup>/min. To the best of our knowledge, this is the highest material removal rate reported so far for laser milling of silicon with ultrafast lasers, while at the same time achieving high surface quality with  $S_a \leq 0.6$   $\mu$ m and no surface defects with diameters exceeding 1  $\mu$ m. In comparison to previously reported results for laser milling of silicon achieving low surface roughness, this is a 740 times higher removal rate than reported in [108] and a 443 times higher material removal rate than reported in [111]. Hence, the presented results show that high-power ultrafast lasers in combination with appropriate processing strategies such as bursts, low peak fluence and high scanning speeds can significantly enhance the throughput of silicon laser milling while maintaining high surface quality. If small feature sizes are required which cannot be processed with a defocused laser beam, other techniques like beam shaping and beam splitting may be applied to distribute the pulse energy and effectively reduce the peak fluence on the workpiece.

In conclusion, we demonstrated high-quality high-throughput silicon laser milling with an ultrafast laser delivering an average power of 1 kW which – to the best of our knowledge – is the first demonstration of material processing with sub-ps laser pulses at this elevated power level. To achieve this, a high-power ultrafast laser in

combination with adapted processing strategies were used. A low surface roughness  $S_a \leq 0.6 \mu\text{m}$  and smooth surface structure with LIPSS and nanoparticles was obtained at high average power by using pulse bursts, low peak fluences, and high scanning speeds. Furthermore, a low roughness was maintained up to the maximum investigated milling depth of  $313 \mu\text{m}$ . The energy-specific volume was measured to be  $\Delta V_E = 3.8 \mu\text{m}^3/\mu\text{J}$  at  $1010 \text{ W}$  on the workpiece, which corresponds to a material removal rate of  $\dot{V} = 230 \text{ mm}^3/\text{min}$ . Hence, high-power ultrafast lasers in combination with appropriate processing strategies can significantly enhance the throughput while maintaining high surface quality.

## 4.2 Additional results for high-quality high-throughput laser milling of metals

The ultrafast laser with sub-ps pulse duration and an average power of  $P = 1010 \text{ W}$  was also used for the laser milling of metals. Identical parameters of  $\lambda_L = 1030 \text{ nm}$ ,  $P = 1010 \text{ W}$ ,  $f_B = 500 \text{ kHz}$ ,  $E_B = 2020 \mu\text{J}$ ,  $N_{\text{ppb}} = 5$ ,  $\phi_0 = 0.74 \text{ J/cm}^2$ ,  $d = 372 \mu\text{m}$ ,  $v_x = 24 \text{ m/s}$ ,  $p_y = 50 \mu\text{m}$  and  $m = 50$  were applied for milling of cavities with an edge length of  $10 \times 10 \text{ mm}^2$  on the widely used metals stainless steel (AISI 304), copper (Cu-DHP), and aluminium (AlSi1Mg).

The results were published in [224] and are shown in Figure 4.5. The compatibility of high quality and simultaneously high throughput in micromachining with ultrafast lasers and average power exceeding  $1 \text{ kW}$  is not limited to silicon with the developed processing strategy. Micromachining of metals yielded similar results as micromachining of silicon, with a fine ripple structure on the surface as depicted by the SEM images in Figure 4.5. The surface roughness was measured to  $S_a = 1.5 \mu\text{m}$  on stainless steel, to  $S_a = 0.8 \mu\text{m}$  on copper, and to  $S_a = 1.1 \mu\text{m}$  on aluminium. The corresponding material removal rates were measured to be  $\dot{V} = 180 \text{ mm}^3/\text{min}$ ,  $\dot{V} = 126 \text{ mm}^3/\text{min}$ , and  $\dot{V} = 174 \text{ mm}^3/\text{min}$ , respectively, and represent the highest reported material removal rates so far for laser milling with ultrafast lasers while achieving high surface quality with  $S_a \leq 1.5 \mu\text{m}$ . Even geometries with lateral dimensions up to tens of millimetres and with depths in the order of hundreds of micrometres can be machined with high-power ultrafast lasers in a reasonable amount of time to achieve high throughput.

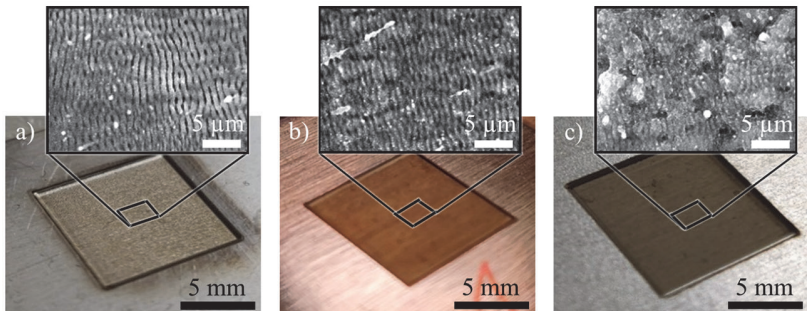


**Figure 4.5** Photograph of the micromachined surfaces and SEM image of the corresponding surface structure of a) stainless steel, b) copper, and c) aluminium. Process parameters:  $\lambda_L = 1030 \text{ nm}$ ,  $P = 1010 \text{ W}$ ,  $f_B = 500 \text{ kHz}$ ,  $E_B = 2020 \text{ μJ}$ ,  $N_{ppb} = 5$ ,  $\phi_0 = 0.74 \text{ J/cm}^2$ ,  $d = 372 \text{ μm}$ ,  $v_x = 24 \text{ m/s}$ ,  $p_y = 40 \text{ μm}$ ,  $m = 50$ .

This is illustrated in Figure 4.6 by the institute’s logo, which was machined 1 mm deep into stainless steel using the aforementioned process parameters.



**Figure 4.6** Photograph of the logo of the institute micromachined on a stainless steel sample with a resulting depth of 1 mm. Process parameters:  $\lambda_L = 1030 \text{ nm}$ ,  $P = 1010 \text{ W}$ ,  $f_B = 500 \text{ kHz}$ ,  $E_B = 2020 \text{ μJ}$ ,  $N_{ppb} = 5$ ,  $\phi_0 = 0.74 \text{ J/cm}^2$ ,  $d = 372 \text{ μm}$ ,  $v_x = 24 \text{ m/s}$ ,  $p_y = 40 \text{ μm}$ ,  $m = 350$ .



## 5 Conclusion

Laser micromachining with short and ultrashort laser pulses enables the flexible creation of a wide range of geometries on a micrometre scale in different materials to influence the functionality of a machined component. Reliably achieving the target depth in a short time is particularly relevant in the economic manufacture of products and components where the depth or aspect ratio of the generated geometry determines the functionality. Each of the three aspects - analytical modelling, process control and process scaling - must therefore be considered to produce mass-customized products "*first time right*" and with high throughput using laser micromachining. Analytical modelling of the depth progress enables the prediction of the machining depth as a function of the process parameters, so that the process parameters can be designed accordingly. Monitoring and controlling the machining depth during micromachining ensures that the targeted depth is achieved reliably and with high accuracy by adjusting the process parameters. Scaling the process to high average laser powers while maintaining the required quality and precision enables high throughput and to reach the target depth in a short process time.

The overall aim of this work was to advance the capabilities of laser micromachining processes with target depth by enhancing each of the three aforementioned aspects.

Two analytical models were derived to calculate the depth progress when machining geometries with high aspect ratios (depth/width) using ultrashort laser pulses: The analytical model for the calculation of the depth progress of percussion-drilled holes is based on the assumptions of a conically shaped hole throughout the drilling process, increasing absorptance with increasing aspect ratio due to multiple diffuse reflections within the hole, and the assumption that the absorbed fluence increases linearly from the entrance to the bottom of the hole. The theoretical prediction agrees well with experimental results obtained from percussion drilling of holes with depths of up to 1.5 mm in stainless steel using picosecond laser pulses.

The analytical model for the calculation of the depth progress of micromachined grooves is based on the assumptions of a V-shaped groove, increasing absorptance with increasing aspect ratio due to multiple specular reflections within the groove, and the assumption that the absorbed fluence increases linearly from the entrance to the bottom of the groove. The theoretical prediction agrees well with experimental results obtained from the engraving of grooves with depths of up to 624  $\mu\text{m}$  in a Ti-alloy using femtosecond laser pulses.

The models derived in this work extend the available analytical models for the calculation of the depth progress of holes and grooves from previously only shallow geometries with low aspect ratios and constant deepening rate to deep geometries with high aspect ratios and decreasing or ceasing deepening rate. The models provide a useful tool estimate the dimensions of the holes and grooves, process windows of micromachining with a high deepening rate, and the maximum achievable depth.

Depth-controlled laser milling was investigated to reliably achieve the targeted depth in two demanding applications:

LPBF-generated parts made from AlSi10Mg and Ti6Al4V typically require post-processing due to excess material from support structures, deviations from the targeted net shape, and high surface roughness. The originally unknown surface topography resulting from complex geometries with shape deviations, free-form surfaces or block support structures were measured by OCT in order to quantify the local amount of excess material. Depth-controlled laser milling with ultrashort laser pulses allowed for locally adapted machining and automated removal of block support structures with a wall height of up to 800  $\mu\text{m}$ . The shape deviation to the targeted net shape was reduced by 63% to 15  $\mu\text{m}$ . Furthermore, the surface roughness was reduced by 81% to 5  $\mu\text{m}$ . As a result, high-quality net shape geometries with a smooth surface were achieved on LPBF-generated metal parts.

Layer-accurate removal of damaged areas is required in the repairing process of parts made from CFRP as preparation for rebuilding the part with repair plies that precisely fit into the removed area. The changing surface topography during laser milling of CFRP was measured by OCT and allowed to determine the local fibre orientation. Determining the fibre orientation with an angular accuracy of better than  $\pm 4^\circ$  allowed to reliably detect the transition between two adjacent layers and thus to stop the laser milling process or change the machined geometry between two layers without knowing the respective layer thickness or target depth in advance. As a result, automated and layer-accurate material removal of CFRP for stepped repair geometries was achieved for parts with a thickness of up to 5 mm.

Process scaling was performed for laser milling of cavities in metals and silicon with an ultrafast laser with an average power exceeding 1 kW, which was the first demonstration of material processing with sub-ps laser pulses at this elevated power level. High-power ultrafast lasers in combination with appropriate processing strategies such as bursts, low fluences and high scanning speeds can significantly enhance the throughput in laser milling while maintaining high surface quality.

The high-power ultrafast laser in combination with an adapted processing strategy was used to demonstrate record-breaking material removal rates of  $126 \text{ mm}^3/\text{min} \leq \dot{V} \leq 180 \text{ mm}^3/\text{min}$  for different metals and  $\dot{V} = 230 \text{ mm}^3/\text{min}$  for silicon. Figure 5.1 depicts the achieved values for comparison with the state of the art (in June 2022).

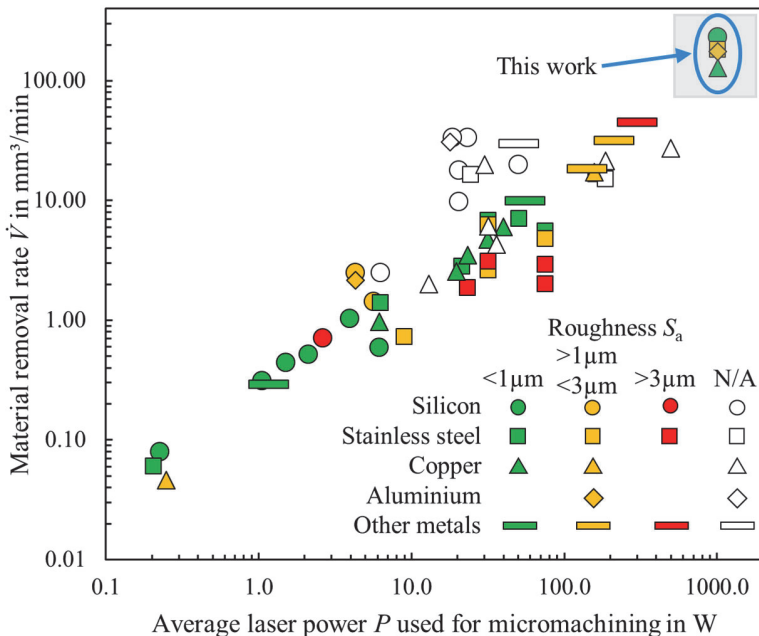


**Figure 5.1** Overview of the state of the art (in June 2022) [60,108,110–112,114,116,125–134] and results of this work [180,224]. No data regarding the roughness were available for white symbols. The results achieved in this work are marked by a blue ellipse.

High surface quality with a roughness  $S_a < 1 \mu\text{m}$  in stainless steel was obtained with material removal rates of up to  $\dot{V} = 16.5 \text{ mm}^3/\text{min}$  before this work [129]. Compared to this the throughput was increased by more than a factor of 11 in this work with only slightly reduced quality with a roughness  $S_a = 1.5 \mu\text{m}$  and a material removal rate of up to  $\dot{V} = 180 \text{ mm}^3/\text{min}$  at an average laser power of  $P = 1010 \text{ W}$ . The throughput for micromachining of cavities in aluminium was increased by a factor of almost 82 to  $\dot{V} = 174 \text{ mm}^3/\text{min}$  compared to [112] at a similar surface quality of  $1.1 \mu\text{m} \leq S_a \leq 1.2 \mu\text{m}$ . The throughput for micromachining cavities in copper with a roughness  $S_a < 1 \mu\text{m}$  was increased by a factor of more than 21 to  $\dot{V} = 126 \text{ mm}^3/\text{min}$  as compared to [134]. High surface quality with a roughness  $S_a < 1 \mu\text{m}$  on silicon was obtained with material removal rates of up to  $\dot{V} \approx 1 \text{ mm}^3/\text{min}$  at an average laser power of  $P = 3.9 \text{ W}$  before this work [111]. In this work the throughput could be increased by a factor of more than 224 to  $\dot{V} = 230 \text{ mm}^3/\text{min}$  at an average laser power of  $P = 1010 \text{ W}$ , while maintaining a surface quality in the high-quality range of  $S_a < 1 \mu\text{m}$  up to a machining depth of several hundred micrometres.

## References

- [1] BUNDESMINISTERIUM FÜR BILDUNG UND FORSCHUNG: *Industrie 4.0*, <https://www.bmbf.de/bmbf/de/forschung/digitale-wirtschaft-und-gesellschaft/industrie-4-0/industrie-4-0.html>, accessed 11.07.2022.
- [2] TSENG, M. M, WANG, Y., JIAO, R. J: *Mass Customization*. In: The International Academy for Production Engineering, IUL-Inst Tech Univ Dortmund, Consiglio Nazionale delle Ricerche: CIRP Encyclopedia of Production Engineering. Springer Berlin, Heidelberg, 2017, 1–8.
- [3] GILMORE, J. H, PINE II, B. J: *The Four Faces of Mass Customization*, 01/02 1997.
- [4] POPRAWA, R., HINKE, C., MEINERS, W. ET AL.: *Digital photonic production along the lines of industry 4.0*. In: NEUENSCHWANDER B, RAČIUKAITIS G, MAKIMURA T et al.: Laser Applications in Microelectronic and Optoelectronic Manufacturing (LAMOM) XXIII. SPIE, 2018, 1–17.
- [5] GRAF, T., ABDOU AHMED, M., BERGER, P. ET AL.: *The laser: One universal tool for manufacturing*. Industrial Laser Solutions **13-15** (2019).
- [6] GOWER, M. C: *Industrial applications of laser micromachining*. Optics express **7** (2000) no.2, 56–67.
- [7] SUGIOKA, K., CHENG, Y.: *Ultrafast lasers—reliable tools for advanced materials processing*. Light: Science & Applications **3** (2014) no.4, 1-12.
- [8] FEUER, A., KUNZ, C., KRAUS, M. ET AL.: *Influence of laser parameters on quality of microholes and process efficiency*. In: NAKATA Y, XU X, ROTH S

- et al.: Laser Applications in Microelectronic and Optoelectronic Manufacturing (LAMOM) XIX., Proc. SPIE, 2014, 1-10.
- [9] ESCH, P., KLOCKE, F., BAUERNHANSL, T. ET AL.: *Methodic development of laser micro structured cutting tools with microscale textures for AW7075 aluminum alloy using a Plackett–Burman screening design*. CIRP Journal of Manufacturing Science and Technology **32** (2021), 188–195.
- [10] KONONENKO, T. V, KNYAZEV, B. A, SOVYK, D. N ET AL.: *Silicon kinoform cylindrical lens with low surface roughness for high-power terahertz radiation*. Optics & Laser Technology **123** (2020), 105953.
- [11] PRICE, F.: *Right First Time*. Using quality control for profit. 1st ed., Routledge, London, 2017.
- [12] BÄUERLE, D.: *Laser Processing and Chemistry*, Springer, Heidelberg, 2011.
- [13] WEBSTER, P. JL, YU, J. XZ, LEUNG, B. YC ET AL.: *In situ 24 kHz coherent imaging of morphology change in laser percussion drilling*. Optics letters **35** (2010) no.5, 646–648.
- [14] WEBSTER, P. JL, WRIGHT, L. G, JI, Y. ET AL.: *Automatic laser welding and milling with in situ inline coherent imaging*. Optics letters **39** (2014) no.21, 6217–6220.
- [15] TIEN, J. M: *Manufacturing and services: From mass production to mass customization*. Journal of Systems Science and Systems Engineering **20** (2011) no.2, 129–154.
- [16] MOTTAY, E., LIU, X., ZHANG, H. ET AL.: *Industrial applications of ultrafast laser processing*. MRS Bulletin **41** (2016) no.12, 984–992.
- [17] WEBER, R., GRAF, T.: *The challenges of productive materials processing with ultrafast lasers*. Advanced Optical Technologies **10** (2021) no.4-5, 239–245.

- 
- [18] REIFF, C., BUSER, M., BETTEN, T. ET AL.: *A Process-Planning Framework for Sustainable Manufacturing*. *Energies* **14** (2021) no.5811, 1–27.
- [19] HÜGEL, H., GRAF, T.: *Materialbearbeitung mit Laser*. Grundlagen und Verfahren. 4th ed., Springer Vieweg, Wiesbaden, 2022.
- [20] LIGHT CONVERSION: *Data sheet Pharos Laser*, <https://lightcon.com/product/pharos-femtosecond-lasers/#specifications>, accessed 12.07.2022.
- [21] TRUMPF: *Data sheet TruMicro 2000 Laser*, [https://www.trumpf.com/de\\_DE/produkte/laser/kurz-und-ultrakurzpuls-laser/trumicro-serie-2000/](https://www.trumpf.com/de_DE/produkte/laser/kurz-und-ultrakurzpuls-laser/trumicro-serie-2000/), accessed 12.07.2022.
- [22] AMPLITUDE: *Data sheet Satsuma Laser*, <https://amplitude-laser.com/wp-content/uploads/2018/10/Satsuma-Ref.-163-i.pdf>, accessed 12.07.2022.
- [23] EKSPLA: *Data sheet Atlantic 5 Laser*, <https://ekspla.com/wp-content/uploads/products/industrial-lasers/Atlantic-5/Atlantic5-datasheet-20220125.pdf>, accessed 12.07.2022.
- [24] SILL OPTICS: *Laser Optics*. F-Theta Lenses - Beam Expanders - Aspheric Lenses - Trapped Ion Lenses, [https://www.silloptics.de/fileadmin/user\\_upload/pdf/Katalog/Laser\\_Optics\\_Sill\\_Optics\\_03\\_2022.pdf](https://www.silloptics.de/fileadmin/user_upload/pdf/Katalog/Laser_Optics_Sill_Optics_03_2022.pdf), accessed 12.07.2022.
- [25] NOLTE, S., MOMMA, C., JACOBS, H. ET AL.: *Ablation of metals by ultrashort laser pulses*. *Journal of the Optical Society of America B* **14** (1997) no.10, 2716–2722.
- [26] MANNION, P., MAGEE, J., COYNE, E. ET AL.: *The effect of damage accumulation behaviour on ablation thresholds and damage morphology in ultrafast laser micro-machining of common metals in air*. *Applied Surface Science* **233** (2004) no.1-4, 275–287.
- [27] ZHIGILEI, L. V., LIN, Z., IVANOV, D. S: *Atomistic Modeling of Short Pulse Laser Ablation of Metals: Connections between Melting, Spallation, and*

- Phase Explosion*. The Journal of Physical Chemistry C **113** (2009) no.27, 11892–11906.
- [28] BORN, M., WOLF, E.: *Principles of optics: Electromagnetic theory of propagation, interference and diffraction of light*, Cambridge Univ. Press, Cambridge, 2009.
- [29] AUDOUARD, E., LOPEZ, J., ANCELOT, B. ET AL.: *Optimization of surface engraving quality with ultrafast lasers*. Journal of Laser Applications **29** (2017) no.2, 1–9.
- [30] LIU, J. M.: *Simple technique for measurements of pulsed Gaussian-beam spot sizes*. Optics letters **7** (1982) no.5, 196–198.
- [31] RACIUKAITIS, G., BRIKAS, M., GECYS, P. ET AL.: *Accumulation effects in laser ablation of metals with high-repetition-rate lasers*. In: PHIPPS CR: High-Power Laser Ablation VII. Proc. SPIE, 2008, 1-11.
- [32] WINTER, J., SPELLAUGE, M., HERMANN, J. ET AL.: *Ultrashort single-pulse laser ablation of stainless steel, aluminium, copper and its dependence on the pulse duration*. Optics express **29** (2021) no.10, 14561–14581.
- [33] JEE, Y., BECKER, M. F., WALSER, R. M.: *Laser-induced damage on single-crystal metal surfaces*. Journal of the Optical Society of America B **5** (1988) no.3, 648–659.
- [34] DI NISO, F., GAUDIUSO, C., SIBILLANO, T. ET AL.: *Role of heat accumulation on the incubation effect in multi-shot laser ablation of stainless steel at high repetition rates*. Optics express **22** (2014) no.10, 12200–12210.
- [35] ASHKENASI, D., LORENZ, M., STOIAN, R. ET AL.: *Surface damage threshold and structuring of dielectrics using femtosecond laser pulses: the role of incubation*. Applied Surface Science **150** (1999) no.1-4, 101–106.
- [36] NEUENSCHWANDER, B., JAEGGI, B., SCHMID, M. ET AL.: *Factors controlling the incubation in the application of ps laser pulses on copper and iron sur-*

- 
- faces*. In: XU X, HENNIG G, NAKATA Y et al.: Laser Applications in Micro-electronic and Optoelectronic Manufacturing (LAMOM) XVIII. Proc. SPIE, 2013, 86070D.
- [37] VOROBYEV, A. Y, GUO, C.: *Enhanced absorptance of gold following multipulse femtosecond laser ablation*. Physical Review B **72** (2005) no.195422, 1–5.
- [38] WEBER, R., GRAF, T., BERGER, P. ET AL.: *Heat accumulation during pulsed laser materials processing*. Optics express **22** (2014) no.9, 11312–11324.
- [39] BAUER, F., MICHALOWSKI, A., KIEDROWSKI, T. ET AL.: *Heat accumulation in ultra-short pulsed scanning laser ablation of metals*. Optics express **23** (2015) no.2, 1035–1043.
- [40] BRINKMEIER, D., HOLDER, D., LOESCHER, A. ET AL.: *Process limits for percussion drilling of stainless steel with ultrashort laser pulses at high average powers*. Applied Physics A **128** (2022) no.35, 1–9.
- [41] AHUIR-TORRES, J. I, ARENAS, M. A, PERRIE, W. ET AL.: *Influence of laser parameters in surface texturing of Ti6Al4V and AA2024-T3 alloys*. Optics and Lasers in Engineering **103** (2018), 100–109.
- [42] MELIANI, H., ASSOUL, M., FONTAINE, M. ET AL.: *Femtosecond laser-matter interaction of tungsten carbide*. Applied optics **60** (2021) no.3, 621–625.
- [43] GRUNER, A., SCHILLE, J., LOESCHNER, U.: *Experimental Study on Micro Hole Drilling Using Ultrashort Pulse Laser Radiation*. Physics Procedia **83** (2016), 157–166.
- [44] HÄFNER, T.: *Multipulseeffekte beim Mikro-Materialabtrag von Stahllegierungen mit Pikosekunden-Laserpulsen*, FAU University Press, Erlangen. Dissertation, 2021.
- [45] DÖRING, S., RICHTER, S., TÜNNERMANN, A. ET AL.: *Evolution of hole depth and shape in ultrashort pulse deep drilling in silicon*. Applied Physics A **105** (2011) no.1, 69–74.

- 
- [46] DÖRING, S.: *Analysis of the Hole Shape Evolution in Ultrashort Pulse Laser Drilling*, Cuvillier Verlag, Jena. Dissertation, 2014.
- [47] ZHAO, W., LIU, H., SHEN, X. ET AL.: *Percussion Drilling Hole in Cu, Al, Ti, and Ni Alloys Using Ultra-Short Pulsed Laser Ablation*. *Materials*, **13** (2019) no.1, 1–12.
- [48] KONONENKO, T. V, FREITAG, C., SOVYK, D. N ET AL.: *Influence of pulse repetition rate on percussion drilling of Ti-based alloy by picosecond laser pulses*. *Optics and Lasers in Engineering* **103** (2018), 65–70.
- [49] FÖRSTER, D. J, WEBER, R., HOLDER, D. ET AL.: *Estimation of the depth limit for percussion drilling with picosecond laser pulses*. *Optics express* **26** (2018) no.9, 11546–11552.
- [50] DÖRING, S., RICHTER, S., NOLTE, S. ET AL.: *In situ imaging of hole shape evolution in ultrashort pulse laser drilling*. *Optics express* **18** (2010) no.19, 20395–20400.
- [51] ABREU FERNANDES, S., SCHOEPS, B., KOWALICK, K. ET AL.: *Femtosecond Laser Ablation of ITO/ZnO for Thin Film Solar Cells*. *Physics Procedia* **41** (2013), 802–809.
- [52] FURMANSKI, J., RUBENCHIK, A. M, SHIRK, M. D ET AL.: *Deterministic processing of alumina with ultrashort laser pulses*. *Journal of Applied Physics* **102** (2007) no.073112, 1–4.
- [53] BOROWIEC, A., HAUGEN, H. K: *Femtosecond laser micromachining of grooves in indium phosphide*. *Applied Physics A* **79** (2004) no.3, 521–529.
- [54] FORNAROLI, C., HOLTkamp, J., GILLNER, A.: *Dicing of thin Si wafers with a picosecond laser ablation process*. In: *LIA - The Laser Institute: International Congress on Applications of Lasers & Electro-Optics*. Laser Institute of America, 2013, 667–671.

- 
- [55] ZHAO, W., WANG, L., YU, Z. ET AL.: *A processing technology of grooves by picosecond ultrashort pulse laser in Ni alloy: Enhancing efficiency and quality*. Optics & Laser Technology **111** (2019), 214–221.
- [56] SCHNELL, G., DUENOW, U., SEITZ, H.: *Effect of Laser Pulse Overlap and Scanning Line Overlap on Femtosecond Laser-Structured Ti6Al4V Surfaces*. Materials, **13** (2020) no.4.
- [57] PALLARÉS-ALDEITURRIAGA, D., CLAUDEL, P., GRANIER, J. ET AL.: *Femtosecond Laser Engraving of Deep Patterns in Steel and Sapphire*. Micromachines **12** (2021) no.7.
- [58] SALAMA, A., YAN, Y., LI, L. ET AL.: *Understanding the self-limiting effect in picosecond laser single and multiple parallel pass drilling/machining of CFRP composite and mild steel*. Materials & Design **107** (2016), 461–469.
- [59] CHENG, J., PERRIE, W., EDWARDSON, S. P ET AL.: *Effects of laser operating parameters on metals micromachining with ultrafast lasers*. Applied Surface Science **256** (2009) no.5, 1514–1520.
- [60] MARIMUTHU, S., DUNLEAVEY, J., SMITH, B.: *Picosecond laser machining of tungsten carbide*. International Journal of Refractory Metals and Hard Materials **92** (2020) no.105338.
- [61] MICHALOWSKI, A.: *Untersuchungen zur Mikrobearbeitung von Stahl mit ultrakurzen Laserpulsen*, Herbert Utz Verlag, München, 2014.
- [62] NEUENSCHWANDER, B., JAEGGI, B., SCHMID, M. ET AL.: *Optimization of the volume ablation rate for metals at different laser pulse-durations from ps to fs*. In: HENNIG G, XU X, GU B et al.: Laser Applications in Microelectronic and Optoelectronic Manufacturing (LAMOM) XVII., Proc. SPIE, 2012, 1–13.
- [63] OGAWA, K., NAKAGAWA, H., IMADA, T. ET AL.: *Laser irradiation method for high-efficiency pulsed laser milling integrated die/mold machining: effects of laser-tracking irradiation on laser milling accuracy*. Advances in Materials and Processing Technologies **4** (2018) no.1, 158–165.

- [64] SCHULZE, V., WEBER, P., RUHS, C.: *Increase of process reliability in the micro-machining processes EDM-milling and laser ablation using on-machine sensors*. Journal of Materials Processing Technology **212** (2012) no.3, 625–632.
- [65] CHANG, G., TU, Y.: *Closed-loop control in ultrafast laser milling process using laser triggered plasma*. International Journal of Machine Tools and Manufacture **60** (2012), 35–39.
- [66] RAELE, M. P., PRETTO, L. R de, ROSSI, W. de et al.: *Focus Tracking System for Femtosecond Laser Machining using Low Coherence Interferometry*. Scientific reports **9** (2019) no.1, 4167.
- [67] BÜCHE, D., KLOSTERMANN, S., ROGÉ, G. ET AL.: *Uncertainties in Compressor and Aircraft Design*. In: HIRSCH C, WUNSCH D, SZUMBARKSI J et al.: *Uncertainty Management for Robust Industrial Design in Aeronautics: Findings and Best Practice Collected During UMRIDA, a Collaborative Research Project (2013–2016) Funded by the European Union*. Springer International Publishing, Cham, Switzerland, 2019, 35–51.
- [68] BERGSTRÖM, D., POWELL, J., KAPLAN, A.: *The absorptance of steels to Nd:YLF and Nd:YAG laser light at room temperature*. Applied Surface Science **253** (2007) no.11, 5017–5028.
- [69] MUSTAFA, H., MEZERA, M., MATTHEWS, D. ET AL.: *Effect of surface roughness on the ultrashort pulsed laser ablation fluence threshold of zinc and steel*. Applied Surface Science **488** (2019), 10–21.
- [70] WIESNER, M., IHLEMANN, J., MÜLLER, H. H ET AL.: *Optical coherence tomography for process control of laser micromachining*. The Review of scientific instruments **81** (2010) no.033705, 1–7.
- [71] SCHMITT, R., MALLMANN, G., WINANDS, K. ET AL.: *Automated Process Initialization of Laser Surface Structuring Processes by Inline Process Metrology*. Physics Procedia **41** (2013), 887–895.

- 
- [72] OVERMEYER, L., DUESING, J. F., SUTTMANN, O. ET AL.: *Laser patterning of thin film sensors on 3-D surfaces*. CIRP Annals **61** (2012) no.1, 215–218.
- [73] BOERNER, P., HAJRI, M., WAHL, T. ET AL.: *Picosecond pulsed laser ablation of dielectric rods: Angle-dependent ablation process model for laser micromachining*. Journal of Applied Physics **125** (2019) no.23, 234902.
- [74] SCHMUTZLER, H., POPP, J., BÜCHTER, E. ET AL.: *Improvement of bonding strength of scarf-bonded carbon fibre/epoxy laminates by Nd:YAG laser surface activation*. Composites Part A: Applied Science and Manufacturing **67** (2014), 123–130.
- [75] SANTHANAKRISHNAN BALAKRISHNAN, V., SEIDLITZ, H.: *Potential repair techniques for automotive composites: A review*. Composites Part B: Engineering **145** (2018), 28–38.
- [76] SHENG, P., CHRYSOLOURIS, G.: *Theoretical Model of Laser Grooving for Composite Materials*. Journal of Composite Materials **29** (1995) no.1, 96–112.
- [77] WOLYNSKI, A., HERRMANN, T., MUCHA, P. ET AL.: *Laser ablation of CFRP using picosecond laser pulses at different wavelengths from UV to IR*. Physics Procedia **12** (2011), 292–301.
- [78] DITTMAR, H., JAESCHKE, P., SUTTMANN, O. ET AL.: *Online laser-based repair preparation of CFRP supported by short coherent interferometry*. 10th Conference on Photonic Technologies LANE 2018 (2018), 1–4.
- [79] KUNZE, R., MALLMANN, G., SCHMITT, R.: *Inline Plasma Analysis as Tool for Process Monitoring in Laser Micro Machining for Multi-layer Materials*. Physics Procedia **83** (2016), 1329–1338.
- [80] FROES, F. H., BOYER, R.: *Additive manufacturing for the aerospace industry*, Elsevier, Amsterdam Netherlands, Cambridge MA United States, 2019.
- [81] EMMELMANN, C., PETERSEN, M., KRANZ, J. ET AL.: *Bionic lightweight design by laser additive manufacturing (LAM) for aircraft industry*. In: AMBS

- P, CURTICAPEAN D, EMMELMANN C et al.: SPIE Eco-Photonics 2011: Sustainable Design, Manufacturing, and Engineering Workforce Education for a Green Future. SPIE, 2011, 1-12.
- [82] JIANG, J., XU, X., STRINGER, J.: *Support Structures for Additive Manufacturing: A Review*. Journal of Manufacturing and Materials Processing **2** (2018) no.4, 64.
- [83] ZHU, Z., KEIMASI, S., ANWER, N. ET AL.: *Review of Shape Deviation Modeling for Additive Manufacturing*. In: EYNARD B, NIGRELLI V, OLIVERI SM et al.: *Advances on Mechanics, Design Engineering and Manufacturing: Proceedings of the International Joint Conference on Mechanics, Design Engineering & Advanced Manufacturing (JCM 2016)*, 14–16 September, 2016, Catania, Italy. Springer Nature, Cham, Switzerland, 2016, 241–250.
- [84] HASSANIN, H., ELSHAER, A., REDHA, B.-D. ET AL.: *Surface Finish Improvement of Additive Manufactured Metal Parts*. In: GUPTA K: *Micro and Precision Manufacturing*. Springer International Publishing, Cham, 2018, 145–164.
- [85] KUMBHAR, N. N., MULAY, A. V.: *Post Processing Methods used to Improve Surface Finish of Products which are Manufactured by Additive Manufacturing Technologies: A Review*. Journal of The Institution of Engineers (India): Series C **99** (2018) no.4, 481–487.
- [86] CAMPANELLI, S. L., CASALINO, G., CONTUZZI, N. ET AL.: *Taguchi Optimization of the Surface Finish Obtained by Laser Ablation on Selective Laser Molten Steel Parts*. Procedia CIRP **12** (2013), 462–467.
- [87] HOFELE, M., SCHANZ, J. ET AL.: *Laser based post processing of additive manufactured metal parts*. Lasers in Manufacturing Conference 2017 (2017), 1–12.
- [88] MINGAREEV, I., BONHOFF, T., EL-SHERIF, A. F ET AL.: *Femtosecond laser post-processing of metal parts produced by laser additive manufacturing*. Journal of Laser Applications **25** (2013) no.5, 52009.

- 
- [89] SCHANZ, J., HOFELE, M., HITZLER, L. ET AL.: *Laser Polishing of Additive Manufactured AlSi10Mg Parts with an Oscillating Laser Beam*. In: ÖCHSNER A, ALTENBACH H: *Machining, Joining and Modifications of Advanced Materials*. Springer Singapore, Singapore, 2016, 159–169.
- [90] CAO, Q., BAI, Y., ZHENG, Z. ET AL.: *Support Removal on Thin-Walled Parts Produced by Laser Powder Bed Fusion*. *3D Printing and Additive Manufacturing* (2022).
- [91] MÖHRING, H.-C., BECKER, D., MAUCHER, C. ET AL.: *Influence of the support structure on the bandsawing process when separating LPBF components from the building platform*. *Journal of Machine Engineering* **22** (2022) no.3, 19–30.
- [92] KATNAM, K. B, DA SILVA, L., YOUNG, T. M: *Bonded repair of composite aircraft structures: A review of scientific challenges and opportunities*. *Progress in Aerospace Sciences* **61** (2013), 26–42.
- [93] FISCHER, F., ROMOLI, L., KLING, R.: *Laser-based repair of carbon fiber reinforced plastics*. *CIRP Annals* **59** (2010) no.1, 203–206.
- [94] VÖLKERMAYER, F., FISCHER, F., STUTE, U. ET AL.: *Laser-based approach for bonded repair of carbon fiber reinforced plastics*. *Physics Procedia* **12** (2011), 537–542.
- [95] DAVILA, Y., CROUZEIX, L., DOUCHIN, B. ET AL.: *Spatial Evolution of the Thickness Variations over a CFRP Laminated Structure*. *Applied Composite Materials* **24** (2017) no.5, 1201–1215.
- [96] NEUENSCHWANDER, B., BUCHER, G. F, NUSSBAUM, C. ET AL.: *Processing of metals and dielectric materials with ps-laserpulses: results, strategies, limitations and needs*. In: NIINO H, MEUNIER M, GU B et al.: *Laser Applications in Microelectronic and Optoelectronic Manufacturing XV*. Proc. SPIE, 2010, 1-14.

- [97] NEUENSCHWANDER, B., JAEGLI, B., SCHMID, M. ET AL.: *Surface Structuring with Ultra-short Laser Pulses: Basics, Limitations and Needs for High Throughput*. Physics Procedia **56** (2014), 1047–1058.
- [98] LIGHTPULSE: *Structuring and texturing*, <https://www.light-pulse.de/en-gb/laserstructuring>, accessed 12.07.2022.
- [99] RAPIDDIRECT: *Surface Roughness Chart: Understanding Surface Finish in Manufacturing*, <https://www.rapiddirect.com/blog/surface-roughness-chart/>, accessed 12.07.2022.
- [100] INDRISIUNAS, S., SVIRPLYS, E., RICHTER, H. ET AL.: *Laser-Ablated Silicon in the Frequency Range From 0.1 to 4.7 THz*. IEEE Transactions on Terahertz Science and Technology **9** (2019) no.6, 581–586.
- [101] MITCHELL, J., CROW, N., NIETO, A.: *Effect of Surface Roughness on Pitting Corrosion of AZ31 Mg Alloy*. Metals **10** (2020) no.5, 651.
- [102] BONSE, J., BAUDACH, S., KRÜGER, J. ET AL.: *Femtosecond laser ablation of silicon—modification thresholds and morphology*. Applied Physics A **74** (2002) no.1, 19–25.
- [103] LEE, S., YANG, D., NIKUMB, S.: *Femtosecond laser micromilling of Si wafers*. Applied Surface Science **254** (2008) no.10, 2996–3005.
- [104] KIRNER, S. V., HERMENS, U., MIMIDIS, A. ET AL.: *Mimicking bug-like surface structures and their fluid transport produced by ultrashort laser pulse irradiation of steel*. Applied Physics A **123** (2017) no.754, 1–13.
- [105] KELLER, W. J., SHEN, N., RUBENCHIK, A. M ET AL.: *Physics of picosecond pulse laser ablation*. Journal of Applied Physics **125** (2019) no.085103, 1–18.
- [106] FAAS, S., BIELKE, U., WEBER, R. ET AL.: *Prediction of the surface structures resulting from heat accumulation during processing with picosecond laser pulses at the average power of 420 W*. Applied Physics A **124** (2018) no.9.

- 
- [107] LAUER, B., JÄGGI, B., NEUENSCHWANDER, B.: *Influence of the Pulse Duration onto the Material Removal Rate and Machining Quality for Different Types of Steel*. *Physics Procedia* **56** (2014), 963–972.
- [108] NEUENSCHWANDER, B., JAEGGI, B., FOERSTER, D. J ET AL.: *Influence of the burst mode onto the specific removal rate for metals and semiconductors*. *Journal of Laser Applications* **31** (2019) no.022203, 1–10.
- [109] SCANLAB: *Data sheet ExcelliSCAN 14*, <https://www.scanlab.de/de/produkte/scan-systeme/excelliscan/excelliscan-14>, accessed 16.07.2022.
- [110] SCHILLE, J., SCHNEIDER, L., LOESCHNER, U.: *Process optimization in high-average-power ultrashort pulse laser microfabrication: how laser process parameters influence efficiency, throughput and quality*. *Applied Physics A* **120** (2015) no.3, 847–855.
- [111] METZNER, D., LICKSCHAT, P., WEIBMANTEL, S.: *Investigations of qualitative aspects with burst mode ablation of silicon and cemented tungsten carbide*. *Applied Physics A* **125** (2019) no.411, 1–6.
- [112] BONAMIS, G., AUDOUARD, E., HÖNNINGER, C. ET AL.: *Systematic study of laser ablation with GHz bursts of femtosecond pulses*. *Optics express* **28** (2020) no.19, 27702–27714.
- [113] MIKHAYLOV, D., KIEDROWSKI, T., LASAGNI, A. F.: *Beam shaping using two spatial light modulators for ultrashort pulse laser ablation of metals*. In: KLOTZBACH U, KLING R, WATANABE A: *Laser-based Micro- and Nanoprocessing XIII*. Proc. SPIE, 2019, 41.
- [114] BRUENING, S., DU, K., JARCZYNSKI, M. ET AL.: *High-throughput micromachining with ultrashort pulsed lasers and multiple spots*. *Journal of Laser Applications* **32** (2020) no.012003, 1–8.
- [115] HAUSCHWITZ, P., MARTAN, J., BIČIŠŤOVÁ, R. ET AL.: *LIPSS-based functional surfaces produced by multi-beam nanostructuring with 2601 beams*

- and real-time thermal processes measurement*. Scientific reports **11** (2021) no.22944, 1–10.
- [116] ŽEMAITIS, A., GAIDYS, M., BRIKAS, M. ET AL.: *Advanced laser scanning for highly-efficient ablation and ultrafast surface structuring: experiment and model*. Scientific reports **8** (2018) no.17376, 1–14.
- [117] SANNER, N., HUOT, N., AUDOUARD, E. ET AL.: *Direct ultrafast laser micro-structuring of materials using programmable beam shaping*. Optics and Lasers in Engineering **45** (2007) no.6, 737–741.
- [118] HÄFNER, T., HEBERLE, J., HOLDER, D. ET AL.: *Speckle reduction techniques in holographic beam shaping for accurate and efficient picosecond laser structuring*. Journal of Laser Applications **29** (2017) no.022205, 1–9.
- [119] GROSSMANN, D. G, FLAMM, D., HELLSTERN, J. ET AL.: *Scaling percussion drilling processes by ultrashort laser pulses using advanced beam shaping*. In: RAČIUKAITIS G, MOLPECERES C, NARAZAKI A et al.: Laser Applications in Microelectronic and Optoelectronic Manufacturing (LAMOM) XXV. Proc. SPIE, 2020, 25.
- [120] ARMBRUSTER, O., NAGHILOU, A., KITZLER, M. ET AL.: *Spot size and pulse number dependence of femtosecond laser ablation thresholds of silicon and stainless steel*. Applied Surface Science **396** (2017), 1736–1740.
- [121] RUSSBUELDT, P., MANS, T., WEITENBERG, J. ET AL.: *Compact diode-pumped 1.1 kW Yb:YAG Innoslab femtosecond amplifier*. Optics letters **35** (2010) no.24, 4169–4171.
- [122] NEGEL, J.-P., VOSS, A., ABDU AHMED, M. ET AL.: *1.1 kW average output power from a thin-disk multipass amplifier for ultrashort laser pulses*. Optics letters **38** (2013) no.24, 5442–5445.
- [123] NUBBEMEYER, T., KAUMANN, M., UEFFING, M. ET AL.: *1 kW, 200 mJ picosecond thin-disk laser system*. Optics letters **42** (2017) no.7, 1381–1384.

- 
- [124] MÜLLER, M., ALESHIRE, C., KLENKE, A. ET AL.: *10.4 kW coherently combined ultrafast fiber laser*. Optics letters **45** (2020) no.11, 3083–3086.
- [125] BORNSCHLEGEL, B., FINGER, J.: *In-Situ Analysis of Ultrashort Pulsed Laser Ablation with Pulse Bursts*. Journal of Laser Micro/Nanoengineering **14** (2019) no.1, 88–94.
- [126] DOMKE, M., PIREDDA, G., ZEHETNER, J. ET AL.: *Minimizing the surface roughness for silicon ablation with ultrashort laser pulses*. Journal of Laser Micro/Nanoengineering **11** (2016) no.1, 100–103.
- [127] ELAHI, P., AKÇAALAN, Ö., ERTEK, C. ET AL.: *High-power Yb-based all-fiber laser delivering 300 fs pulses for high-speed ablation-cooled material removal*. Optics letters **43** (2018) no.3, 535–538.
- [128] FINGER, J., KALUPKA, C., REININGHAUS, M.: *High power ultra-short pulse laser ablation of IN718 using high repetition rates*. Journal of Materials Processing Technology **226** (2015), 221–227.
- [129] GAFNER, M., REMUND, S. M., CHAJA, M. W ET AL.: *High-rate laser processing with ultrashort laser pulses by combination of diffractive elements with synchronized galvo scanning*. Advanced Optical Technologies **10** (2021) no.4-5, 333–352.
- [130] GILLNER, A., FINGER, J., GRETZKI, P. ET AL.: *High Power Laser Processing with Ultrafast and Multi-Parallel Beams*. Journal of Laser Micro/Nanoengineering **14** (2019) no.2, 129–137.
- [131] HIRSIGER, T., GAFNER, M., REMUND, S. M ET AL.: *Machining metals and silicon with GHz bursts: Surprising tremendous reduction of the specific removal rate for surface texturing applications*. In: RAČIUKAITIS G, MOLPECERES C, NARAZAKI A et al.: Laser Applications in Microelectronic and Optoelectronic Manufacturing (LAMOM) XXV., Proc. SPIE, 2020, 27.
- [132] KNAPPE, R., HALOUI, H., SEIFERT, A. ET AL.: *Scaling ablation rates for picosecond lasers using burst micromachining*. In: PFLEGING W, LU Y, WASHIO

- K et al.: Laser-based Micro- and Nanopackaging and Assembly IV. SPIE, 2010, 75850H.
- [133] SAILER, M., JANSEN, F., FEHRENBACHER, A. ET AL.: *Micromachining flexibility by tunable ultrashort pulse duration, pulse-on-demand, and hybrid processing from single pulse to GHz burst with TruMicro Series 2000*. In: RAČIUKAITIS G, MOLPECERES C, NARAZAKI A et al.: Laser Applications in Microelectronic and Optoelectronic Manufacturing (LAMOM) XXV., Proc. SPIE, 2020, 29.
- [134] ŽEMAITIS, A., GAIDYS, M., GEČYS, P. ET AL.: *Rapid high-quality 3D micro-machining by optimised efficient ultrashort laser ablation*. Optics and Lasers in Engineering **114** (2019), 83–89.
- [135] EUROPEAN COMMISSION: *High throughPut LasER processing of Diamond and Silicon (HIPERDIAS)*. Fact Sheet - Objective, <https://cordis.europa.eu/project/id/687880>.
- [136] MOTTAY, E.: *Ultrashort-pulse laser applications advance*. Industrial Laser Solutions (2020).
- [137] National Renewable Energy Laboratory: *High-Throughput Laser Processing*, <https://www.nrel.gov/manufacturing/laser-processing.html>, accessed 10.01.2023.
- [138] FRAUNHOFER ILT: *Flexibly Battery Design through High-Rate Laser Ablation*, [https://www.ilt.fraunhofer.de/content/dam/ilt/en/documents/annual\\_reports/ar20/tf2/jb20-s60-flexible-battery-design-through-high-rate-laser-ablation.pdf](https://www.ilt.fraunhofer.de/content/dam/ilt/en/documents/annual_reports/ar20/tf2/jb20-s60-flexible-battery-design-through-high-rate-laser-ablation.pdf).
- [139] NEWPORT: *Laser Micromachining*, <https://www.newport.com/n/laser-micromachining>, accessed 10.01.2023.
- [140] STUART, D.: *Chasing higher powers: The race for ultrafast kilowatt lasers*, <https://www.electrooptics.com/feature/chasing-higher-powers-race-ultrafast-kilowatt-lasers>, accessed 20.01.2023.

- 
- [141] HOLDER, D., WEBER, R., GRAF, T. ET AL.: *Analytical model for the depth progress of percussion drilling with ultrashort laser pulses*. Applied Physics A **127** (2021) no.302, 1–8.
- [142] VOLLERTSEN, F., SCHMIDT, F.: *Dry metal forming: Definition, chances and challenges*. International Journal of Precision Engineering and Manufacturing-Green Technology **1** (2014) no.1, 59–62.
- [143] ZAHEDI, E., WOERZ, C., REICHARD, G. ET AL.: *Lubricant-free deep drawing using CO<sub>2</sub> and N<sub>2</sub> as volatile media injected through laser-drilled micro-holes*. Manufacturing Review **6** (2019) no.11, 1–11.
- [144] KRAUS, M., AHMED, M. A., MICHALOWSKI, A. ET AL.: *Microdrilling in steel using ultrashort pulsed laser beams with radial and azimuthal polarization*. Optics express **18** (2010) no.21, 22305–22313.
- [145] ZHANG, H., DI, J., ZHOU, M. ET AL.: *An investigation on the hole quality during picosecond laser helical drilling of stainless steel 304*. Applied Physics A **119** (2015) no.2, 745–752.
- [146] KROSCHER, A., MICHALOWSKI, A., GRAF, T.: *Model of the final borehole geometry for helical laser drilling*. Advanced Optical Technologies **7** (2018) no.3, 183–188.
- [147] ANCONA, A., RÖSER, F., RADEMAKER, K. ET AL.: *High speed laser drilling of metals using a high repetition rate, high average power ultrafast fiber CPA system*. Optics express **16** (2008) no.12, 8958–8968.
- [148] FINGER, J., REININGHAUS, M.: *Effect of pulse to pulse interactions on ultra-short pulse laser drilling of steel with repetition rates up to 10 MHz*. Optics express **22** (2014) no.15, 18790–18799.
- [149] FÖRSTER, D. J., WEBER, R., GRAF, T.: *Residual heat during ultrashort laser drilling of metals*. Proceedings of LPM2017 - the 18th International Symposium on Laser Precision Microfabrication (2017), 1–4.

- [150] WEBER, R., GRAF, T., FREITAG, C. ET AL.: *Processing constraints resulting from heat accumulation during pulsed and repetitive laser materials processing*. Optics express **25** (2017) no.4, 3966–3979.
- [151] KLIMENTOV, S. M, KONONENKO, T. V, PIVOVAROV, P. A ET AL.: *The role of plasma in ablation of materials by ultrashort laser pulses*. Quantum Electronics **31** (2001) no.5, 378–382.
- [152] KLIMENTOV, S. M, GARNOV, S. V, KONOV, V. I ET AL.: *Effect of low-threshold air breakdown on material ablation by short laser pulses*. Physics of Wave Phenomena **15** (2007) no.1, 1–11.
- [153] HOLDER, D., LEIS, A., BUSER, M. ET AL.: *High-quality net shape geometries from additively manufactured parts using closed-loop controlled ablation with ultrashort laser pulses*. Advanced Optical Technologies **9** (2020) no.1-2, 101–110.
- [154] HOLDER, D., BUSER, M., BOLEY, S. ET AL.: *Image processing based detection of the fibre orientation during depth-controlled laser ablation of CFRP monitored by optical coherence tomography*. Materials & Design **203** (2021) no.109567, 1–10.
- [155] WEBSTER, P. JL, LEUNG, B. YC, YU, J. XZ ET AL.: *Coaxial real-time metrology and gas assisted laser micromachining: process development, stochastic behavior, and feedback control*. In: MAHER MA, CHIAO J-C, RESNICK PJ: Micromachining and Microfabrication Process Technology XV., Proc. SPIE, 2010, 1–10.
- [156] CHICHKOV, B. N, MOMMA, C., NOLTE, S. ET AL.: *Femtosecond, picosecond and nanosecond laser ablation of solids*. Applied Physics A Materials Science & Processing **63** (1996) no.2, 109–115.
- [157] MICHALOWSKI, A., QIN, Y., WEBER, R. ET AL.: *Theoretical and experimental studies of ultra-short pulsed laser drilling of steel*. In: MACKENZIE JI, JELÍNKOVÁ H, TAIRA T et al.: Laser Sources and Applications II., Proc. SPIE, 2014, 91350R.

- 
- [158] GOUFFÉ, A.: *Correction d'ouverture des corps-noirs artificiels compte tenu des diffusions multiples internes*. Revue d'Optique **24** (1945), 1–10.
- [159] GOUFFÉ, A.: *Aperture Corrections of Artificial Black Bodies with Consideration of Multiple Internal Diffusions*. General dynamics/Astronautics, San Diego, CA (1960).
- [160] HÜGEL, H., GRAF, T.: *Laser in der Fertigung*. Grundlagen der Strahlquellen, Systeme, Fertigungsverfahren. 3rd ed., Springer Vieweg + Teubner, Wiesbaden, 2014.
- [161] JOHNSON, P. B, CHRISTY, R. W: *Optical constants of transition metals: Ti, V, Cr, Mn, Fe, Co, Ni, and Pd*. Physical Review B **9** (1974) no.12, 5056–5070.
- [162] LIDE, D. R, HAYNES, W. M: *CRC Handbook of Chemistry and Physics*, CRC Press/Taylor and Francis, Boca Ranton, FL, 2010.
- [163] KAYE, G. WC, LABY, T. H: *Tables of Physical & Chemical Constants*. 16th ed., Longman, Harlow, 1995.
- [164] GEČYS, P., VINČIŪNAS, A., GEDVILAS, M. ET AL.: *Ripple Formation by Femtosecond Laser Pulses for Enhanced Absorptance of Stainless Steel*. Journal of Laser Micro/Nanoengineering **10** (2015) no.2, 129–133.
- [165] KAM, D. H, MAZUMDER, J., KIM, J.: *Conical microspike morphology formation and control on various metal surfaces using femtosecond laser pulse*. Journal of Laser Applications **28** (2016) no.4, 1–6.
- [166] BANKS, P. S, FEIT, M. D, RUBENCHIK, A. M ET AL.: *Material effects in ultrashort pulse laser drilling of metals*. Applied Physics A: Materials Science & Processing **69** (1999) no.7, 377-380.
- [167] GAMALY, E. G, MADSEN, N. R, DUERING, M. ET AL.: *Ablation of metals with picosecond laser pulses: Evidence of long-lived nonequilibrium conditions at the surface*. Physical Review B **71** (2005) no.17, 1–12.

- [168] WECK, A., CRAWFORD, T., WILKINSON, D. S ET AL.: *Laser drilling of high aspect ratio holes in copper with femtosecond, picosecond and nanosecond pulses*. Applied Physics A **90** (2008) no.3, 537–543.
- [169] DÜSING, J. F, HWANG, D. J, GRIGOROPOULOS, C. P ET AL.: *Optical emission imaging and spectroscopy during femtosecond laser ablation of thin metal films on flexible polymer substrates*. International Congress on Applications of Lasers & Electro Optics (ICALEO) **888** (2009), 1–5.
- [170] WINTER, J., RAPP, S., SPELLAUGE, M. ET AL.: *Ultrafast pump-probe ellipsometry and microscopy reveal the surface dynamics of femtosecond laser ablation of aluminium and stainless steel*. Applied Surface Science **511** (2020) no.145514, 1–11.
- [171] LUFT, A., FRANZ, U., EMSERMANN, L. ET AL.: *A study of thermal and mechanical effects on materials induced by pulsed laser drilling*. Applied Physics A Materials Science & Processing **63** (1996) no.2, 93–101.
- [172] PARK, K.-W., NA, S.-J.: *Theoretical investigations on multiple-reflection and Rayleigh absorption–emission–scattering effects in laser drilling*. Applied Surface Science **256** (2010) no.8, 2392–2399.
- [173] HOLDER, D., WEBER, R., GRAF, T.: *Analytical Model for the Depth Progress during Laser Micromachining of V-Shaped Grooves*. Micromachines **13** (2022) no.870, 1–12.
- [174] BRUNEEL, D., MATRAS, G., LE HARZIC, R. ET AL.: *Micromachining of metals with ultra-short Ti-Sapphire lasers: Prediction and optimization of the processing time*. Optics and Lasers in Engineering **48** (2010) no.3, 268–271.
- [175] WANG, C., HU, H., LI, Z. ET AL.: *Enhanced Osseointegration of Titanium Alloy Implants with Laser Microgrooved Surfaces and Graphene Oxide Coating*. ACS Applied Materials & Interfaces **11** (2019), 39470–39483.
- [176] BERTHIER, J., GOSSELIN, D., VILLARD, N. ET AL.: *The Dynamics of Spontaneous Capillary Flow in Confined and Open Microchannels*. Sensors & Transducers **183** (2014) no.12, 123–128.

- 
- [177] HOLDER, D., WEBER, R., GRAF, T.: *Laser micromachining of V-shaped grooves on Ti6Al4V with ultrashort laser pulses for passive directional transport of fluids*. International Congress on Applications of Lasers & Electro Optics (ICALEO) (2021), 1–9.
- [178] BUTKUS, S., ALESENKOV, A., PAIPULAS, D. ET AL.: *Analysis of the Micromachining Process of Dielectric and Metallic Substrates Immersed in Water with Femtosecond Pulses*. *Micromachines* **6** (2015) no.12, 2010–2022.
- [179] STEPÁK, B. D., ANTOŃCZAK, A. J., SZUSTAKIEWICZ, K.: *Optimization of femtosecond laser micromachining of polylactide and PLLA/HAp composite*. In: KLOTZBACH U, WASHIO K, KLING R: *Laser-based Micro- and Nanoprocessing XII.*, Proc. SPIE, 2018, 70.
- [180] HOLDER, D., WEBER, R., RÖCKER, C. ET AL.: *High-quality high-throughput silicon laser milling using a 1 kW sub-picosecond laser*. *Optics letters* **46** (2021) no.2, 384–387.
- [181] CANGUEIRO, L., AUDOUARD, E., MARTIN, P.-E. ET AL.: *Model for ultrafast laser micromachining*. Proc. SPIE **10520** (2018), 1–12.
- [182] KONONENKO, T. V., KONOV, V. I., GARNOV, S. V ET AL.: *Dynamics of Deep Short Pulse Laser Drilling: Ablative Stages and Light Propagation*. *Laser Physics* **11** (2001) no.3, 343–351.
- [183] HABASHI, F.: *Titanium, Physical and Chemical Properties*. In: KRETSINGER RH, UVERSKY VN, PERMYAKOV EA: *Encyclopedia of Metalloproteins*. Springer New York, New York, NY, 2013, 2251–2252.
- [184] PALM, K. J, MURRAY, J. B, NARAYAN, T. C ET AL.: *Dynamic Optical Properties of Metal Hydrides*. *ACS Photonics* **5** (2018), 4677–4686.
- [185] MAHARJAN, N., ZHOU, W., ZHOU, Y. ET AL.: *Ablation morphology and ablation threshold of Ti-6Al-4V alloy during femtosecond laser processing*. *Applied Physics A* **124** (2018) no.8.

- [186] HOLDER, D., BOLEY, S., BUSER, M. ET AL.: *OCT-controlled generation of complex geometries on stainless steel using ultra-short laser pulses*. Lasers in Manufacturing Conference 2019 (2019), 1–6.
- [187] BOLEY, S., HOLDER, D., ONUSEIT, V. ET AL.: *Distance controlled laser ablation of CFRP*. Lasers in Manufacturing Conference 2017 (2017), 1–9.
- [188] HOLDER, D., BOLEY, S., BUSER, M. ET AL.: *In-process determination of fiber orientation for layer accurate laser ablation of CFRP*. Procedia CIRP **74** (2018), 557–561.
- [189] SCHARES, R. L., SCHMITT, S., EMONTS, M. ET AL.: *Improving accuracy of robot-guided 3D laser surface processing by workpiece measurement in a blink*. In: KAIERLE S, HEINEMANN SW: High-Power Laser Materials Processing: Applications, Diagnostics, and Systems VII., Proc. SPIE, 2018, 1–12.
- [190] FISHBURN, J. M., WITHFORD, M. J., COUTTS, D. W ET AL.: *Study of the fluence dependent interplay between laser induced material removal mechanisms in metals: Vaporization, melt displacement and melt ejection*. Applied Surface Science **252** (2006) no.14, 5182–5188.
- [191] KURŠELIS, K., KIYAN, R., CHICHKOV, B. N: *Formation of corrugated and porous steel surfaces by femtosecond laser irradiation*. Applied Surface Science **258** (2012) no.22, 8845–8852.
- [192] HE, C., ZIBNER, F., FORNAROLI, C. ET AL.: *High-precision Helical Cutting Using Ultra-short Laser Pulses*. Physics Procedia **56** (2014), 1066–1072.
- [193] HOLDER, D., BUSER, M., LEIS, A. ET AL.: *Post-processing of additively manufactured metal parts by ultrashort laser pulses for high-quality net shape geometries and advanced functionality*. IOP Conference Series: Materials Science and Engineering **1135** (2021) no.012005, 1–10.
- [194] SOUTIS, C.: *Fibre reinforced composites in aircraft construction*. Progress in Aerospace Sciences **41** (2005) no.2, 143–151.

- 
- [195] BULL, D. J, HELFEN, L., SINCLAIR, I. ET AL.: *A comparison of multi-scale 3D X-ray tomographic inspection techniques for assessing carbon fibre composite impact damage*. Composites Science and Technology **75** (2013), 55–61.
- [196] PELIVANOV, I., AMBROZIŃSKI, Ł., KHOMENKO, A. ET AL.: *High resolution imaging of impacted CFRP composites with a fiber-optic laser-ultrasound scanner*. Photoacoustics **4** (2016) no.2, 55–64.
- [197] GARDINER, G.: *Primary structure repair: The quest for quality*. High Performance Composites (2011), 48–54.
- [198] FREESE, J. de, HOLTSMANNSPÖTTER, J., RASCHENDORFER, S. ET AL.: *End milling of Carbon Fiber Reinforced Plastics as surface pretreatment for adhesive bonding – effect of intralaminar damages and particle residues*. The Journal of Adhesion **96** (2020) no.12, 1122–1140.
- [199] OHMI, M., TANIZAWA, M., FUKUNAGA, A. ET AL.: *In-situ Observation of Tissue Laser Ablation Using Optical Coherence Tomography*. Optical and Quantum Electronics **37** (2005) no.13-15, 1175–1183.
- [200] BOLEY, M., FETZER, F., WEBER, R. ET AL.: *Statistical evaluation method to determine the laser welding depth by optical coherence tomography*. Optics and Lasers in Engineering **119** (2019), 56–64.
- [201] SCHMITT, R., MALLMANN, G., WINANDS, K. ET AL.: *Inline Process Metrology System for the Control of Laser Surface Structuring Processes*. Physics Procedia **39** (2012), 814–822.
- [202] GENNA, S., LEONE, C., UCCIARDELLO, N. ET AL.: *Increasing adhesive bonding of carbon fiber reinforced thermoplastic matrix by laser surface treatment*. Polymer Engineering & Science **57** (2017) no.7, 685–692.
- [203] ONUSEIT, V., WEBER, R., WIEDENMANN, M. ET AL.: *Efficient Laser Processing of CFRP*. 8th International Conference on Photonic Technologies LANE 2014 (2014), 1–4.

- [204] WEBER, R., HAFNER, M., MICHALOWSKI, A. ET AL.: *Minimum Damage in CFRP Laser Processing*. Physics Procedia **12** (2011), 302–307.
- [205] KONONENKO, T. V., FREITAG, C., KOMLENOK, M. S ET AL.: *Heat accumulation effects in short-pulse multi-pass cutting of carbon fiber reinforced plastics*. Journal of Applied Physics **118** (2015) no.103105, 1–6.
- [206] LI, Z. L., ZHENG, H. Y., LIM, G. C ET AL.: *Study on UV laser machining quality of carbon fibre reinforced composites*. Composites Part A: Applied Science and Manufacturing **41** (2010) no.10, 1403–1408.
- [207] LEONE, C., PAPA, I., TAGLIAFERRI, F. ET AL.: *Investigation of CFRP laser milling using a 30W Q-switched Yb:YAG fiber laser: Effect of process parameters on removal mechanisms and HAZ formation*. Composites Part A: Applied Science and Manufacturing **55** (2013), 129–142.
- [208] TAKAHASHI, K., TSUKAMOTO, M., MASUNO, S. ET AL.: *Influence of laser scanning conditions on CFRP processing with a pulsed fiber laser*. Journal of Materials Processing Technology **222** (2015), 110–121.
- [209] EHRENSTEIN, G. W.: *Faserverbund-Kunststoffe*. Werkstoffe-Verarbeitung-Eigenschaften. 1st ed., Carl Hanser Verlag, München, 2006.
- [210] CANNY, J.: *A Computational Approach to Edge Detection*. IEEE Transactions on Pattern Analysis and Machine Intelligence **8** (1986) no.6, 679–698.
- [211] SHI, L., WU, S.: *Automatic fiber orientation detection for sewed carbon fibers*. Tsinghua Science and Technology **12** (2007) no.4, 447–452.
- [212] RADON, J.: *Über die Bestimmung von Funktionen durch ihre Integralwerte längs gewisser Mannigfaltigen*. Berichte über die Verhandlungen der Königlich-Sächsischen Akademie der Wissenschaften zu Leipzig **69** (1917), 262–277.
- [213] TAO, X., EADES, A.: *Errors, artifacts, and improvements in EBSD processing and mapping*. Microscopy and microanalysis the official journal of

- 
- Microscopy Society of America, Microbeam Analysis Society, Microscopical Society of Canada **11** (2005) no.1, 79–87.
- [214] KRAUSE, M., HAUSHERR, J. M., BURGETH, B. ET AL.: *Determination of the fibre orientation in composites using the structure tensor and local X-ray transform*. Journal of Materials Science **45** (2010) no.4, 888–896.
- [215] PARKER, J. R.: *Algorithms for Image Processing and Computer Vision*. 2nd ed., Wiley Publishing, Indianapolis, 2011.
- [216] FEIH, S., MOURITZ, A. P.: *Tensile properties of carbon fibres and carbon fibre–polymer composites in fire*. Composites Part A: Applied Science and Manufacturing **43** (2012) no.5, 765–772.
- [217] GOWER, M. C.: *Laser micromachining for manufacturing MEMS devices*. Proc. SPIE **4559** (2001), 53–59.
- [218] MINKEVIČIUS, L., INDRIŠIŪNAS, S., ŠNIAUKAS, R. ET AL.: *Terahertz multi-level phase Fresnel lenses fabricated by laser patterning of silicon*. Optics letters **42** (2017) no.10, 1875–1878.
- [219] SARACENO, C. J., SUTTER, D., METZGER, T. ET AL.: *The amazing progress of high-power ultrafast thin-disk lasers*. Journal of the European Optical Society-Rapid Publications **15** (2019) no.1.
- [220] FREITAG, C., WIEDENMANN, M., NEGEL, J.-P. ET AL.: *High-quality processing of CFRP with a 1.1-kW picosecond laser*. Applied Physics A **119** (2015) no.4, 1237–1243.
- [221] FAAS, S., BIELKE, U., WEBER, R. ET AL.: *Scaling the productivity of laser structuring processes using picosecond laser pulses at average powers of up to 420 W to produce superhydrophobic surfaces on stainless steel AISI 316L*. Scientific reports **9** (2019) no.1, 1933.
- [222] DIETZ, T., JENNE, M., BAUER, D. ET AL.: *Ultrafast thin-disk multi-pass amplifier system providing 1.9 kW of average output power and pulse energies*

- 
- in the 10 mJ range at 1 ps of pulse duration for glass-cleaving applications.* Optics express **28** (2020) no.8, 11415–11423.
- [223] RÖCKER, C., LOESCHER, A., DELAIGUE, M. ET AL.: *Flexible Sub-1 ps Ultra-fast Laser Exceeding 1 kW of Output Power for High-Throughput Surface Structuring.* In: Optical Society of America: Laser Congress 2019 (ASSL, LAC, LS&C). OSA, Washington, D.C., 1-2.
- [224] ABDOU AHMED, M., ROECKER, C., LOESCHER, A. ET AL.: *High-power ultra-fast thin-disk multipass amplifiers for efficient laser-based manufacturing.* Advanced Optical Technologies **10** (2021) no.4-5, 285–295.

# Danksagung

Die vorliegende Dissertation entstand während meiner Tätigkeit als wissenschaftlicher Mitarbeiter am Institut für Strahlwerkzeuge (IFSW) an der Universität Stuttgart. Hiermit möchte ich mich bei all jenen bedanken, die mich beim Erstellen dieser Arbeit unterstützt haben und mir diese Arbeit ermöglicht haben.

An erster Stelle möchte ich meinem Doktorvater Prof. Dr. phil. nat. Thomas Graf für die Betreuung dieser Arbeit sowie für die stetige Unterstützung hierbei danken. Die zahlreichen Anregungen bei den Publikationen sowie das angenehme Arbeitsumfeld, welches er am IFSW geschaffen hat, haben maßgeblich zum Gelingen dieser Arbeit beigetragen.

Bei Prof. Dr.-Ing. André Zimmermann möchte ich mich für die Übernahme des Mitberichts sowie für die Unterstützung bedanken.

Herzlich bedanken möchte ich mich auch bei apl. Prof. Dr. phil. nat. Rudolf Weber für seine wertvolle Unterstützung und die zahlreichen anregenden Diskussionen. Hervorzuheben ist an dieser Stelle auch sein entgegengebrachtes Vertrauen, welches er mir bei der Ausübung meiner Tätigkeit als wissenschaftlicher Mitarbeiter gewährte.

Mein Dank gilt auch Dr. Marwan Abdou Ahmed und Volker Onuseit für ihre Unterstützung und Engagement bei abteilungsübergreifenden Projekten und Publikationen.

Bedanken möchte ich mich auch bei allen Kolleginnen und Kollegen am IFSW, die durch den fachlichen Austausch und die gute Atmosphäre stets einen tollen Arbeitsalltag ermöglichen. Hervorzuheben sind dabei Manuel Henn, Dr. Daniel Förster, Dr. Christian Freitag, Kathrin Placzek, Dr. Michael Jarwitz, Michael Sawannia, Dr. Christian Hagenlocher, Jannik Lind, Artur Leis, Jonas Wagner, Matthias Buser, Steffen Boley, Alexander Peter, David Brinkmeier, Dr. Christoph Röcker und André Loescher.

Darüber hinaus möchte ich auch den zahlreichen Studentinnen und Studenten danken, die im Rahmen einer studentischen Arbeit oder als HiWi wertvolle Beiträge zu meiner Arbeit geleistet haben.

Ein Dank gilt auch meinen Eltern Claudia und Roland, welche durch ihre stetige Unterstützung während meines Studiums und während der Promotion die Grundlage für das Gelingen dieser Arbeit gelegt haben. Abschließend gilt mein besonderer Dank meiner Frau Frauke für ihre fortwährende Unterstützung und ihre Entbehrungen bei meiner Arbeit im wissenschaftlichen Umfeld.

# Laser in der Materialbearbeitung

## Forschungsberichte des IFSW (Institut für Strahlwerkzeuge)

Herausgegeben von

Prof. Dr.-Ing. habil. Helmut Hügel, Universität Stuttgart

Forschungsberichte des IFSW von 1992 bis 1999 erschienen im Teubner Verlag, Stuttgart

### **Zoske, Uwe**

Modell zur rechnerischen Simulation von Laserresonatoren und Strahlführungssystemen  
1992, 186 Seiten, ISBN 3-519-06205-4

### **Gorriz, Michael**

Adaptive Optik und Sensorik im Strahlführungssystem von Laserbearbeitungsanlagen  
1992, vergriffen, ISBN 3-519-06206-2

### **Mohr, Ursula**

Geschwindigkeitsbestimmende Strahleigenschaften und Einkoppelmechanismen beim CO<sub>2</sub>-Laserschneiden von Metallen  
1993, 130 Seiten, ISBN 3-519-06207-0

### **Rudlaff, Thomas**

Arbeiten zur Optimierung des Umwandlungshärrens mit Laserstrahlen  
1993, 152 Seiten, ISBN 3-519-06208-9

### **Borik, Stefan**

Einfluß optischer Komponenten auf die Strahlqualität von Hochleistungslasern  
1993, 200 Seiten, ISBN 3-519-06209-7

### **Paul, Rüdiger**

Optimierung von HF-Gasentladungen für schnell längsgeströmte CO<sub>2</sub>-Laser  
1994, 149 Seiten, ISBN 3-519-06210-0

### **Wahl, Roland**

Robotergeführtes Laserstrahlschweißen mit Steuerung der Polarisationsrichtung  
1994, 150 Seiten, ISBN 3-519-06211-9

### **Frederking, Klaus-Dieter**

Lasertiöten kleiner Kupferbauteile mit geregelter Lotdrahtzufuhr  
1994, 139 Seiten, ISBN 3-519-06212-7

### **Grünewald, Karin M.**

Modellierung der Energietransferprozesse in längsgeströmten CO<sub>2</sub>-Lasern  
1994, 158 Seiten, ISBN 3-519-06213-5

### **Shen, Jialin**

Optimierung von Verfahren der Laseroberflächenbehandlung mit gleichzeitiger Pulverzufuhr  
1994, 160 Seiten, ISBN 3-519-06214-3

### **Arnold, Johannes M.**

Abtragen metallischer und keramischer Werkstoffe mit Excimerlasern  
1994, 192 Seiten, ISBN 3-519-06215-1

### **Holzwarth, Achim**

Ausbreitung und Dämpfung von Stoßwellen in Excimerlasern  
1994, 153 Seiten, ISBN 3-519-06216-X

### **Dausinger, Friedrich**

Strahlwerkzeug Laser: Energieeinkopplung und Prozeßeffektivität  
1995, 143 Seiten, ISBN 3-519-06217-8

### **Meiners, Eckhard**

Abtragende Bearbeitung von Keramiken und Metallen mit gepulstem Nd:YAG-Laser als zweistufiger Prozeß  
1995, 120 Seiten, ISBN 3-519-06222-4

### **Beck, Markus**

Modellierung des Lasertiefschweißens  
1996, 160 Seiten, ISBN 3-519-06218-6

### **Breining, Klaus**

Auslegung und Vermessung von Gasentladungsstrecken für CO<sub>2</sub>-Hochleistungslaser  
1996, 131 Seiten, ISBN 3-519-06219-4

### **Griebsch, Jürgen**

Grundlagenuntersuchungen zur Qualitätssicherung beim gepulsten Lasertiefschweißen  
1996, 133 Seiten, ISBN 3-519-06220-8

### **Kreputat, Walter**

Aerodynamische Fenster für industrielle Hochleistungslaser  
1996, 144 Seiten, ISBN 3-519-06221-6

### **Xiao, Min**

Vergleichende Untersuchungen zum Schneiden dünner Bleche mit CO<sub>2</sub>- und Nd:YAG-Lasern  
1996, 118 Seiten, ISBN 3-519-06223-2

### **Glumann, Christiane**

Verbesserte Prozeßsicherheit und Qualität durch Strahlkombination beim Laserschweißen  
1996, 143 Seiten, ISBN 3-519-06224-0

### **Gross, Herbert**

Propagation höhermodiger Laserstrahlung und deren Wechselwirkung mit optischen Systemen  
1996, 191 Seiten, ISBN 3-519-06225-9

### **Rapp, Jürgen**

Laserschweißsignung von Aluminiumwerkstoffen für Anwendungen im Leichtbau  
1996, 202 Seiten, ISBN 3-519-06226-7

**Wittig, Klaus**

Theoretische Methoden und experimentelle Verfahren zur Charakterisierung von Hochleistungslaserstrahlung  
1996, 198 Seiten, ISBN 3-519-06227-5

**Grünenwald, Bernd**

Verfahrensoptimierung und Schichtcharakterisierung beim einstufigen Cermet-Beschichten mittels CO<sub>2</sub>-Hochleistungslaser  
1996, 160 Seiten, ISBN 3-519-06229-1

**Lee, Jae-Hoon**

Laserverfahren zur strukturierten Metallisierung  
1996, 154 Seiten, ISBN 3-519-06232-1

**Albinus, Uwe N. W.**

Metallisches Beschichten mittels PLD-Verfahren  
1996, 144 Seiten, ISBN 3-519-06233-X

**Wiedmaier, Matthias**

Konstruktive und verfahrenstechnische Entwicklungen zur Komplettbearbeitung in Drehzentren mit integrierten Laserverfahren  
1997, 129 Seiten, ISBN 3-519-06228-3

**Bloehs, Wolfgang**

Laserstrahlhärten mit angepaßten Strahlführungssystemen  
1997, 143 Seiten, ISBN 3-519-06230-5

**Bea, Martin**

Adaptive Optik für die Materialbearbeitung mit CO<sub>2</sub>-Laserstrahlung  
1997, 143 Seiten, ISBN 3-519-06231-3

**Stöhr, Michael**

Beeinflussung der Lichtemission bei mikrokanalgekühlten Laserdioden  
1997, 147 Seiten, ISBN 3-519-06234-8

**Plaß, Wilfried**

Zerstörschwellen und Degradation von CO<sub>2</sub>-Laseroptiken  
1998, 158 Seiten, ISBN 3-519-06235-6

**Schaller, Markus K. R.**

Lasergestützte Abscheidung dünner Edelmetallschichten zum Heißgaskorrosionsschutz für Mo-lybdän  
1998, 163 Seiten, ISBN 3-519-06236-4

**Hack, Rüdiger**

System- und verfahrenstechnischer Vergleich von Nd:YAG- und CO<sub>2</sub>-Lasern im Leistungsbereich bis 5 kW  
1998, 165 Seiten, ISBN 3-519-06237-2

**Krupka, René**

Photothermische Charakterisierung optischer Komponenten für Hochleistungslaser  
1998, 139 Seiten, ISBN 3-519-06238-0

**Pfeiffer, Wolfgang**

Fluiddynamische und elektrophysikalisch optimierte Entladungsstrecken für CO<sub>2</sub>-Hochleistungslaser  
1998, 152 Seiten, ISBN 3-519-06239-9

**Volz, Robert**

Optimiertes Beschichten von Gußeisen-, Aluminium- und Kupfergrundwerkstoffen mit Lasern  
1998, 133 Seiten, ISBN 3-519-06240-2

**Bartelt-Berger, Lars**

Lasersystem aus kohärent gekoppelten Grundmode-Diodenlasern  
1999, 135 Seiten, ISBN 3-519-06241-0

**Müller-Hummel, Peter**

Entwicklung einer Inprozeßtemperaturmeßvorrichtung zur Optimierung der laserunterstützten Zerspanung  
1999, 139 Seiten, ISBN 3-519-06242-9

**Rohde, Hansjörg**

Qualitätsbestimmende Prozeßparameter beim Einzelpulsbohren mit einem Nd:YAG-Slablaser  
1999, 171 Seiten, ISBN 3-519-06243-7

**Huonker, Martin**

Strahlführung in CO<sub>2</sub>-Hochleistungslasersystemen zur Materialbearbeitung  
1999, 121 Seiten, ISBN 3-519-06244-5

**Callies, Gert**

Modellierung von qualitäts- und effektivitätsbestimmenden Mechanismen beim Laserabtragen  
1999, 119 Seiten, ISBN 3-519-06245-3

**Schubert, Michael E.**

Leistungskalierbares Lasersystem aus fasergekoppelten Singlemode-Diodenlasern  
1999, 105 Seiten, ISBN 3-519-06246-1

**Kern, Markus**

Gas- und magnetofluidynamische Maßnahmen zur Beeinflussung der Nahtqualität beim Laserstrahlschweißen  
1999, 132 Seiten, ISBN 3-519-06247-X

**Raiber, Armin**

Grundlagen und Prozeßtechnik für das Lasermikrobohren technischer Keramiken  
1999, 135 Seiten, ISBN 3-519-06248-8

# Lasert in der Materialbearbeitung

## Forschungsberichte des IFSW (Institut für Strahlwerkzeuge)

Herausgegeben von

Prof. Dr.-Ing. habil. Helmut Hügel, Universität Stuttgart

Forschungsberichte des IFSW ab 2000 erschienen im Herbert Utz Verlag, München

### Schittenhelm, Henrik

Diagnostik des laserinduzierten Plasmas beim Abtragen und Schweißen  
2000, 141 Seiten, ISBN 3-89675-712-1

### Stewen, Christian

Scheibenlaser mit Kilowatt-Dauerstrichleistung  
2000, 145 Seiten, ISBN 3-89675-763-6

### Schmitz, Christian

Gaselektronische Analysemethoden zur Optimierung von Lasergasentladungen  
2000, 107 Seiten, ISBN 3-89675-773-3

### Karszewski, Martin

Scheibenlaser höchster Strahlqualität  
2000, 132 Seiten, ISBN 3-89675-785-7

### Chang, Chin-Lung

Berechnung der Schmelzbadgeometrie beim Laserstrahlschweißen mit Mehrfokustechnik  
2000, 141 Seiten, ISBN 3-89675-825-X

### Haag, Matthias

Systemtechnische Optimierungen der Strahlqualität von Hochleistungsdiodenlasern  
2000, 166 Seiten, ISBN 3-89675-840-3

### Bahnmüller, Jochen

Charakterisierung gepulster Laserstrahlung zur Qualitätssteigerung beim Laserbohren  
2000, 138 Seiten, ISBN 3-89675-851-9

### Schellhorn, Martin Carl Johannes

CO-Hochleistungslaser: Charakteristika und Einsatzmöglichkeiten beim Schweißen  
2000, 142 Seiten, ISBN 3-89675-849-7

### Angstenberger, Birgit

Fliehkraftunterstütztes Laserbeschichten  
2000, 153 Seiten, ISBN 3-89675-861-6

### Bachhofer, Andreas

Schneiden und Schweißen von Aluminiumwerkstoffen mit Festkörperlasern für den Karoseriebau  
2001, 194 Seiten, ISBN 3-89675-881-0

### Breitschwerdt, Sven

Qualitätssicherung beim Laserstrahlschweißen  
2001, 150 Seiten, ISBN 3-8316-0032-5

### Mochmann, Gunter

Laserkristallisation von Siliziumschichten auf Glas- und Kunststoffsubstraten für die Herstellung verbesserter Dünnschichttransistoren  
2001, 170 Seiten, ISBN 3-89675-811-X

### Herrmann, Andreas

Fertigungsorientierte Verfahrensentwicklung des Weichlötlens mit Diodenlasern  
2002, 133 Seiten, ISBN 3-8316-0086-4

### Mästle, Rüdiger

Bestimmung der Propagationseigenschaften von Laserstrahlung  
2002, 147 Seiten, ISBN 3-8316-0113-5

### Voß, Andreas

Der Scheibenlaser: Theoretische Grundlagen des Dauertrichbetriebs und erste experimentelle Ergebnisse anhand von Yb:YAG  
2002, 195 Seiten, ISBN 3-8316-0121-6

### Müller, Matthias G.

Prozessüberwachung beim Laserstrahlschweißen durch Auswertung der reflektierten Leistung  
2002, 122 Seiten, ISBN 3-8316-0144-5

### Abeln, Tobias

Grundlagen und Verfahrenstechnik des reaktiven Laserpräzisionsabtragens von Stahl  
2002, 138 Seiten, ISBN 3-8316-0137-2

### Erhard, Steffen

Pumpoptiken und Resonatoren für den Scheibenlaser  
2002, 184 Seiten, ISBN 3-8316-0173-9

### Contag, Karsten

Modellierung und numerische Auslegung des Yb:YAG-Scheibenlasers  
2002, 155 Seiten, ISBN 3-8316-0172-0

### Krassel, Klaus

Konzepte und Konstruktionen zur laserintegrierten Komplettbearbeitung in Werkzeugmaschinen  
2002, 140 Seiten, ISBN 3-8316-0176-3

### Staud, Jürgen

Sensitive Werkzeuge für ein neues Montagekonzept in der Mikrosystemtechnik  
2002, 122 Seiten, ISBN 3-8316-0175-5

### Schinzler, Cornelius M.

Nd:YAG-Laserstrahlschweißen von Aluminiumwerkstoffen für Anwendungen im Automobilbau  
2002, 177 Seiten, ISBN 3-8316-0201-8

### Sebastian, Michael

Grundlagenuntersuchungen zur Laser-Plasma-CVD Synthese von Diamant und amorphen Kohlenstoffen  
2002, 153 Seiten, ISBN 3-8316-0200-X

**Lücke, Bernd**

Kohärente Kopplung von Vertikalemitter-Arrays  
2003, 120 Seiten, ISBN 3-8316-0224-7

**Hohenberger, Bernd**

Laserstrahlschweißen mit Nd:YAG-Doppelfokus-  
technik – Steigerung von Prozeßsicherheit, Fle-  
xibilität und verfügbarer Strahlleistung  
2003, 128 Seiten, ISBN 3-8316-0223-9

**Jasper, Knut**

Neue Konzepte der Laserstrahlformung und  
-führung für die Mikrotechnik  
2003, 152 Seiten, ISBN 3-8316-0205-0

**Heimerdinger, Christoph**

Laserstrahlschweißen von Aluminiumlegierungen  
für die Luftfahrt  
2003, 112 Seiten, ISBN 3-8316-0256-5

**Christoph Fleig**

Evaluierung eines Messverfahrens zur genauen  
Bestimmung des Reflexionsgrades optischer  
Komponenten  
2003, 150 Seiten, ISBN 3-8316-0274-3

**Joachim Radtke**

Herstellung von Präzisionsdurchbrüchen in ke-  
ramischen Werkstoffen mittels repetierender  
Laserbearbeitung  
2003, 150 Seiten, ISBN 3-8316-0285-9

**Michael Brandner**

Steigerung der Prozesseffizienz beim Löten und  
Kleben mit Hochleistungsdiodenlasern  
2003, 195 Seiten, ISBN 3-8316-0288-3

**Reinhard Winkler**

Porenbildung beim Laserstrahlschweißen von  
Aluminium-Druckguss  
2004, 153 Seiten, ISBN 3-8316-0313-8

**Helmut Kindler**

Optische und gerätetechnische Entwicklungen  
zum Laserstrahlspritzen  
2004, 117 Seiten, ISBN 3-8316-0315-4

**Andreas Ruf**

Modellierung des Perkussionsbohrens von Metal-  
len mit kurz- und ultrakurzgepulsten Lasern  
2004, 140 Seiten, ISBN 3-8316-0372-3

**Guido Hergenhan**

Kohärente Kopplung von Vertikalemittern – Sys-  
temkonzept und experimentelle Verifizierung  
2004, 115 Seiten, ISBN 3-8316-0376-6

**Klaus Goth**

Schweißen von Mischverbindungen aus Alumi-  
numguß- und Knetlegierungen mit CO<sub>2</sub>-Laser  
unter besonderer Berücksichtigung der Nahtart  
2004, 143 Seiten, ISBN 3-8316-0427-4

**Armin Strauch**

Effiziente Lösung des inversen Problems beim  
Laserstrahlschweißen durch Simulation und  
Experiment  
2004, 169 Seiten, ISBN 3-8316-0425-8

**Thomas Wawra**

Verfahrensstrategien für Bohrungen hoher Präzi-  
sion mittels Laserstrahlung  
2004, 162 Seiten, ISBN 3-8316-0453-3

**Michael Honer**

Prozesssicherungsmaßnahmen beim Bohren  
metallischer Werkstoffe mittels Laserstrahlung  
2004, 113 Seiten, ISBN 3-8316-0441-x

**Thomas Herzinger**

Prozessüberwachung beim Laserbohren von  
Turbinenschaufeln  
2004, 143 Seiten, ISBN 3-8316-0443-6

**Reiner Heigl**

Herstellung von Randschichten auf Aluminium-  
gusslegierungen mittels Laserstrahlung  
2004, 173 Seiten, ISBN 3-8316-0460-8

# Lasert in der Materialbearbeitung

## Forschungsberichte des IFSW (Institut für Strahlwerkzeuge)

Herausgegeben von

Prof. Dr. phil. nat. Thomas Graf, Universität Stuttgart

Forschungsberichte des IFSW ab 2005 erschienen im Herbert Utz Verlag, München

### Thomas Fuhrich

Marangoni-effekt beim Laserstrahliefschweißen von Stahl  
2005, 163 Seiten, ISBN 3-8316-0493-2

### Daniel Müller

Pulsenergiestabilität bei regenerativen Kurzpulsverstärkern im Scheibenlaserdesign  
2005, 172 Seiten, ISBN 3-8316-0508-4

### Jiancun Gao

Neodym-dotierte Quasi-Drei-Niveau-Scheibenlaser: Hohe Ausgangsleistung und Frequenzverdopplung  
2005, 148 Seiten, ISBN 3-8316-0521-1

### Wolfgang Gref

Laserstrahltschweißen von Aluminiumwerkstoffen mit der Fokustrixtechnik  
2005, 136 Seiten, ISBN 3-8316-0537-8

### Michael Weikert

Oberflächenstrukturieren mit ultrakurzen Laserpulsen  
2005, 116 Seiten, ISBN 3-8316-0573-4

### Julian Sigel

Lasergenerieren metallischer Bauteile mit variabelm Laserstrahldurchmesser in modularen Fertigungssystemen  
2006, 132 Seiten, ISBN 3-8316-0572-6

### Andreas Ruß

Schweißen mit dem Scheibenlaser-Potentiale der guten Fokussierbarkeit  
2006, 142 Seiten, ISBN 3-8316-0580-7

### Gabriele Seibold

Absorption technischer Oberflächen in der Lasermaterialbearbeitung  
2006, 156 Seiten, ISBN 3-8316-0618-8

### Dirk Lindenau

Magnetisch beeinflusstes Laserstrahltschweißen  
2007, 180 Seiten, ISBN 978-3-8316-0687-0

### Jens Walter

Gesetzmäßigkeiten beim Lasergenerieren als Basis für die Prozesssteuerung und -regelung  
2008, 140 Seiten, ISBN 978-3-8316-0770-9

### Heiko Ridderbusch

Longitudinal angeregte passiv gütegeschaltete Laserzündkerze  
2008, 175 Seiten, ISBN 978-3-8316-0840-9

### Markus Leimser

Strömungsinduzierte Einflüsse auf die Naht Eigenschaften beim Laserstrahltschweißen von Aluminiumwerkstoffen  
2009, 150 Seiten, ISBN 978-3-8316-0854-6

### Mikhail Larionov

Kontaktierung und Charakterisierung von Kristallen für Scheibenlaser  
2009, 186 Seiten, ISBN 978-3-8316-0855-3

### Jürgen Müller-Borhanian

Kamerabasierte In-Prozessüberwachung beim Laserstrahltschweißen  
2009, 162 Seiten, ISBN 978-3-8316-0890-4

### Andreas Letsch

Charakterisierung allgemein astigmatischer Laserstrahlung mit der Methode der zweiten Momente  
2009, 176 Seiten, ISBN 978-3-8316-0896-6

### Thomas Kübler

Modellierung und Simulation des Halbleiterscheibenlasers  
2009, 152 Seiten, ISBN 978-3-8316-0918-5

### Günter Ambrosy

Nutzung elektromagnetischer Volumenkräfte beim Laserstrahltschweißen  
2009, 170 Seiten, ISBN 978-3-8316-0925-3

### Agnes Ott

Oberflächenmodifikation von Aluminiumlegierungen mit Laserstrahlung: Prozessverständnis und Schichtcharakterisierung  
2010, 226 Seiten, ISBN 978-3-8316-0959-8

### Detlef Breittling

Gasphaseneinflüsse beim Abtragen und Bohren mit ultrakurz gepulster Laserstrahlung  
2010, 200 Seiten, ISBN 978-3-8316-0960-4

### Dmitrij Walter

Online-Qualitätssicherung beim Bohren mittels ultrakurz gepulster Laserstrahlung  
2010, 156 Seiten, ISBN 978-3-8316-0968-0

### Jan-Philipp Weberpals

Nutzen und Grenzen guter Fokussierbarkeit beim Laserstrahltschweißen  
2010, 154 Seiten, ISBN 978-3-8316-0995-6

### Angelika Beyertt

Yb:KYW regenerativer Verstärker für ultrakurze Pulse  
2010, 166 Seiten, ISBN 978-3-8316-4002-7

**Christian Stolzenburg**

Hochrepetierende Kurzpuls-Scheibenlaser im infraroten und grünen Spektralbereich  
2011, 184 Seiten, ISBN 978-3-8316-4041-6

**Svent-Simon Beyertt**

Quantenfilm-Pumpen zur Leistungsskalierung von Halbleiter-Scheibenlasern  
2011, 130 Seiten, ISBN 978-3-8316-4051-5

**Sonja Kittel**

Verzugsarmes Laserstrahlschweißen an axial-symmetrischen Bauteilen  
2011, 162 Seiten, ISBN 978-3-8316-4088-1

**Andrey Andreev**

Schweißen mit dem Scheibenlaser im Getriebebau – Prozessmerkmale und Anlagenkonzepte  
2011, 140 Seiten, ISBN 978-3-8316-4103-1

**Christian Föhl**

Einsatz ultrakurz gepulster Laserstrahlung zum Präzisionsbohren von Metallen  
2011, 156 Seiten, ISBN 978-3-8316-4120-8

**Andreas Josef Birnesser**

Prozessregelung beim Laserstrahlschweißen  
2011, 150 Seiten, ISBN 978-3-8316-4133-8

**Christoph Neugebauer**

Thermisch aktive optische Bauelemente für den resonatorinternen Einsatz beim Scheibenlaser  
2012, 220 Seiten, ISBN 978-3-8316-4178-9

**Andreas Dauner**

Fluidmechanische Maßnahmen zur Reduzierung von Schmelzablagerungen beim Hochgeschwindigkeitslaserbohren  
2012, 150 Seiten, ISBN 978-3-8316-4194-9

**Axel Heß**

Vorteile und Herausforderungen beim Laserstrahlschweißen mit Strahlquellen höchster Fokussierbarkeit  
2012, 164 Seiten, ISBN 978-3-8316-4198-7

**Christian Gehrke**

Überwachung der Struktureigenschaften beim Oberflächenstrukturieren mit ultrakurzen Laserpulsen  
2013, 164 Seiten, ISBN 978-3-8316-4271-7

**David Schindhelm**

In-Prozess Qualitätssicherung für das Laserstrahlschneiden von Metallen  
2013, 150 Seiten, ISBN 978-3-8316-4345-5

**Tilman Froschmeier-Hans**

Festigkeitsverhalten laserstrahlgeschweißter belastungsangepasster Stahlwerkstoffverbindungen  
2014, 200 Seiten, ISBN 978-3-8316-4347-9

**Moritz Vogel**

Speciality Fibers for High Brightness Laser Beam Delivery  
2014, 187 Seiten, ISBN 978-3-8316-4382-0

**Andreas Michalowski**

Untersuchungen zur Mikrobearbeitung von Stahl mit ultrakurzen Laserpulsen  
2014, 176 Seiten, ISBN 978-3-8316-4424-7

**Georg Stöppler**

Untersuchung eines OPOs im mittleren Infrarot im Hinblick auf Anwendungen für minimalinvasive Chirurgie  
2015, 144 Seiten, ISBN 978-3-8316-4437-7

**Patrick Mucha**

Qualitäts- und produktivitätsbeeinflussende Mechanismen beim Laserschneiden von CF und CFK  
2015, 120 Seiten, ISBN 978-3-8316-4516-9

**Claus-Dieter Reiniger**

Fluiddynamische Effekte beim Remote-Laserstrahlschweißen von Blechen mit Fügspalt  
2015, 188 Seiten, ISBN 978-3-8316-4528-2

**Andreas Leitz**

Laserstrahlschweißen von Kupfer- und Aluminiumwerkstoffen in Mischverbindung  
2016, 172 Seiten, ISBN 978-3-8316-4549-7

**Peter Stritt**

Prozessstrategien zur Vermeidung von Heißrissen beim Remote-Laserstrahlschweißen von AlMgSi 6016  
2016, 194 Seiten, ISBN 978-3-8316-4555-8

**Katrin Sarah Wentsch**

Analyse Ytterbium-dotierter Materialien für den Einsatz in ultrakurz-gepulsten Scheibenlasersystemen  
2016, 162 Seiten, ISBN 978-3-8316-4578-7

**Jan-Philipp Negel**

Scheibenlaser-Multipassverstärker für ultrakurze Laserpulse mit Ausgangsleistungen im kW-Bereich  
2017, 142 Seiten, ISBN 978-3-8316-4632-6

**Christian Freitag**

Energietransportmechanismen bei der gepulsten Laserbearbeitung Carbonfaser verstärkter Kunststoffe  
2017, 152 Seiten, ISBN 978-3-8316-4638-8

**Andreas Popp**

Faserlaser und Faserlaserverstärker als Brillanzkonverter für Scheibenlaserstrahlen  
2017, 242 Seiten, ISBN 978-3-8316-4643-2

**Karin Heller**

Analytische Temperaturfeldbeschreibung beim Laserstrahlschweißen für thermographische Prozessbeobachtung  
2017, 130 Seiten, ISBN 978-3-8316-4654-8

**Stefan Piehler**

Resonatorinterne Kompensation thermisch induzierter Wellenfrontstörungen in hochbrillanten Scheibenlasern  
2017, 148 Seiten, ISBN 978-3-8316-4690-6

**Felix Abt**

Bildbasierte Charakterisierung und Regelung von Laserschweißprozessen  
2017, 232 Seiten, ISBN 978-3-8316-4691-3

**Volker Rominger**

Untersuchungen der Prozessvorgänge bei Einschweißungen in Baustahl mit Lasern hoher Brillanz  
2017, 186 Seiten, ISBN 978-3-8316-4692-0

**Thomas Rataj**

Hochleistungstaugliche faserintegrierte Strahlweichen  
2018, 142 Seiten, ISBN 978-3-8316-4733-0

**Michael Diez**

Pulsformung zur schädigungsarmen Laserbearbeitung von Silizium  
2018, 194 Seiten, ISBN 978-3-8316-4737-8

**Andreas Heider**

Erweitern der Prozessgrenzen beim Laserstrahlschweißen von Kupfer mit Einschweißstiefen zwischen 1 mm und 10 mm  
2018, 156 Seiten, ISBN 978-3-8316-4738-5

**Marcel Schäfer**

Energetische Beeinflussung von Schmelzeffluss und Heißrissbildung beim Laserstrahlschweißen von Vergütungsstahl  
2018, 146 Seiten, ISBN 978-3-8316-4742-2

## Laser in der Materialbearbeitung

### Forschungsberichte des IFSW (Institut für Strahlwerkzeuge)

Herausgegeben von

Prof. Dr. phil. nat. Thomas Graf, Universität Stuttgart

Forschungsberichte des IFSW ab 2019 erschienen im utzverlag, München

**Tom Dietrich**

Gitterwellenleiterstrukturen zur Strahlformung in Hochleistungsscheibenlasern  
2019, 154 Seiten, ISBN 978-3-8316-4785-9

**Martin Rumpel**

Applications of Grating Waveguide Structures in Solid-State Lasers  
2019, 112 Seiten, ISBN 978-3-8316-4801-6

**Michael Eckerle**

Generation and amplification of ultrashort pulsed high-power cylindrical vector beams  
2019, 112 Seiten, ISBN 978-3-8316-4804-7

**Martin Stubenvoll**

Messung und Kompensation thermisch induzierter Wellenfrontdeformationen in optischen Elementen  
2019, 118 Seiten, ISBN 978-3-8316-4819-1

**Christian Hagenlocher**

Die Kornstruktur und der Heißrisswiderstand von Laserstrahlschweißnähten in Aluminiumlegierungen  
2020, 150 Seiten, ISBN 978-3-8316-4864-1

**Florian Fetzer**

Analyse der Geometrie und Stabilität der Kapillare beim Laserstrahltiefschweißen mittels reduzierter Modelle.  
2020, 180 Seiten, ISBN 978-3-8316-4874-0

**Michael Jarwitz**

Laserstrahlschweißen von Metallen mit unterschiedlichen thermophysikalischen Eigenschaften.  
2020, 154 Seiten, ISBN 978-3-8316-4882-5

**Christian Röhrer**

Flexible Führung hochbrillanter Laserstrahlen mit optischen Fasern  
2020, 130 Seiten, ISBN 978-3-8316-4888-7

**Martin Sommer**

Laserstrahlschweißen der Aluminiumlegierung AlMgSi mittels Strahloszillation  
2021, 110 Seiten, ISBN 978-3-8316-4898-6

**Birgit Weichert**

Experimental Investigations on Power Scaling of High-Brightness cw Ytterbium-Doped Thin-Disk Lasers.  
2021, 166 Seiten, ISBN 978-3-8316-4914-3

**Sebastian Faas**

Oberflächenfunktionalisierung von Stahl mit UKP-Lasern mit mehreren Hundert Watt mittlerer Laserleistung.  
2021, 95 Seiten, ISBN 978-3-8316-4935-8

**Daniel Weller**

Erhöhung der Prozesssicherheit beim Remote-Laserstrahlfügen von Aluminiumwerkstoffen.  
2021, 130 Seiten, ISBN 978-3-8316-4940-2

**Sebastian Hecker**

Verfahren zur Inline-Prozessüberwachung für das Schweißen von Glas mit Ultrakurzpulslasern  
2022, 132 Seiten, ISBN 978-3-8316-4955-6

**Frieder Beirow**

Leistungsskalierung ultrakurz gepulster radial polarisierter Laserstrahlung.  
2022, 150 Seiten, ISBN 978-3-8316-4970-9

**Meiko Boley**

Bestimmung und Regelung der Kapillar- und Nahttiefe beim Laserstrahlschweißen.  
2022, 154 Seiten, ISBN 978-3-8316-4986-0

**Christoph Röcker**

Flexible Verstärkung und Frequenzkonversion ultrakurzer Laserpulse mit Ausgangsleistungen im kW-Bereich  
2022, 182 Seiten, ISBN 978-3-8316-4987-7

**Oliver Bocksrocker**

Mechanismen der Entstehung von Schnittunregelmäßigkeiten beim Laserschneiden mit 1  $\mu\text{m}$  Wellenlänge  
2023, 128 Seiten, ISBN 978-3-8316-4999-0

**Daniel Förster**

Energieeinkopplung und Energieumwandlungsprozesse bei der Bearbeitung von Metallen mit ultrakurzen Laserpulsen  
2023, 150 Seiten, ISBN 978-3-8316-5009-5

**Daniel Holder**

Laser micromachining with target depth  
2023, 194 Seiten, ISBN 978-3-8316-5010-1



